Werkstofftechnik

Changli Li

Diamond Cloth-Supported Nickel-Manganese Oxide Electrodes for High-Performance Flexible Supercapacitors

Schriftenreihe der Arbeitsgruppe
des Lehrstuhls für Oberflächen- und Werkstofftechnologie
im Institut für Werkstofftechnik

Herausgeber: Prof. Dr. rer. nat. habil. Xin jiang

Band 24

Changli Li

Diamond Cloth-Supported Nickel-Manganese Oxide Electrodes for High-Performance Flexible Supercapacitors

Schriftenreihe der Arbeitsgruppe des Lehrstuhls für Oberflächen- und Werkstofftechnologie im Institut für Werkstofftechnik

Impressum

Prof. Dr. rer. nat. Habil. Xin Jiang

Lehrstuhl für Oberflächen- und Werkstofftechnologie

Institut für Werkstofftechnik

Universität Siegen

57076 Siegen

ISSN: 2194-0096

Zugl.: Siegen, Univ., Diss., 2026

Diamond Cloth-Supported Nickel-Manganese Oxide Electrodes for High-Performance Flexible Supercapacitors

Von der Naturwissenschaftlich-Technischen Fakultät

der Universität Siegen

zur Erlangung des Grades eines Doktors

der Ingenieurwissenschaften

genehmigte

Dissertation

von:	M. Sc. Changli Li
aus:	China
eingereicht am:	19. November 2025
Mündliche Prüfung am:	27. March 2026
Referent:	Prof. Dr. rer. nat. habil. Xin Jiang
Korreferent:	Prof. Dr.-Ing. habil. Nianjun Yang

Zusammenfassung

Superkondensatoren (SCs) haben sich in den letzten Jahren als eine der zentralen Technologien der elektrochemischen Energiespeicherung etabliert. Ihr hohes Leistungsvermögen, gekennzeichnet durch außergewöhnliche Leistungsdichte, schnelle Lade- und Entladeprozesse, ausgezeichnete Zyklusstabilität und hohe Betriebssicherheit, macht sie zu vielversprechenden Kandidaten für eine Vielzahl praktischer Anwendungen. Mit dem dynamischen Fortschritt tragbarer und insbesondere auch tragbarer, flexibler Elektronik steigt die Nachfrage nach leistungsfähigen flexiblen SCs kontinuierlich an. Dies hat umfangreiche Forschungsarbeiten zur Entwicklung innovativer Elektrodenmaterialien, Elektrolyte und Gerätearchitekturen angestoßen. Von diesen Komponenten nehmen die Elektrodenmaterialien eine Schlüsselrolle ein, da sie maßgeblich die elektrochemische Leistungsfähigkeit sowie die mechanische Flexibilität von SCs bestimmen.

In dieser Arbeit wurden drei Elektrodensysteme entworfen und hergestellt: flexibles Diamond Cloth (DC), $NiMnO_x$-beschichtetes Kohlenstoffgewebe ($NiMnO_x$@CC) sowie $NiMnO_x$-beschichtetes Diamond Cloth ($NiMnO_x$@DC). Deren elektrochemische Eigenschaften wurden umfassend untersucht.

Das flexible DC wurde durch das Überwachsen eines bor-dotierten Diamantfilms (BDD) auf Kohlenstoffgewebe (CC) mittels mikrowellenunterstützter plasmaverstärkter chemischer Gasphasenabscheidung (MWCVD) synthetisiert. Eine Ti-Zwischenschicht wurde eingesetzt, um das CC vor Plasmaätzung zu schützen und die Haftung des BDD zu verbessern. Die DC-Elektrode zeigte exzellente elektrochemische Eigenschaften, darunter erhöhte Kapazität, gute Rate-Performance sowie außergewöhnliche Zyklusstabilität. Ein symmetrischer Pseudokondensator (PC), bestehend aus zwei DC-Elektroden, erreichte eine Energiedichte von 45,96 $\mu Wh\ cm^{-2}$ bei 4,25 $mW\ cm^{-2}$ und behielt 17,64 $\mu Wh\ cm^{-2}$ bei 67,93 $mW\ cm^{-2}$. Darüber hinaus wies der symmetrische DC-EDLC (Electric Double-Layer Capacitor) eine hervorragende mechanische Flexibilität auf.

Zur Einführung von Pseudokapazität wurden MnO_x-Filme mittels Elektroabscheidung auf CC synthetisiert, was eine bessere Konformität, Schichtdickenkontrolle und

Reproduzierbarkeit als hydrothermale Verfahren ermöglichte. Die optimierte Ni-dotierte Elektrode ($NiMnO_x$@CC) zeigte größere Stromantworten, ein weites Potentialfenster (-0,1—1,4 V *vs.* Ag/AgCl) und ausgeprägte Redox-Peaks. Sie erreichte eine spezifische Kapazität von 47,1 mF cm^{-2} bei 10 mV s^{-1} und 42,8 mF cm^{-2} bei 1 mA cm^{-2} in 1,0 M Na_2SO_4 Electrolyte, bei einer Coulomb-Effizienz von > 98,5 % über 10.000 Zyklen. Allerdings war die Zyklusstabilität begrenzt (≈ 16 % nach 10.000 Zyklen), was die praktische Anwendbarkeit einschränkte.

Der Ersatz von CC durch DC als Substrat führte zu einer synergistischen $NiMnO_x$@DC-Elektrode. Ein Abscheidepotential von 1,0 V erwies sich dabei als optimal, da es Abscheiderate und Nebenreaktionen in Einklang brachte. Die optimierte $NiMnO_x$@DC-Elektrode zeigte ausgeprägte Redox-Eigenschaften und hohe spezifische Kapazitäten von 180,5 mF cm^{-2} bei einer Scanrate von 10 mV s^{-1} sowie 228,1 mF cm^{-2} bei einer Stromdichte von 2 mA cm^{-2}. Gleichzeitig wurde eine nahezu ideale Coulomb-Effizienz (ca. 100 %) über 10.000 Lade-Entlade-Zyklen erreicht. Darüber hinaus zeigte die $NiMnO_x$@DC-Elektrode im Vergleich zur $NiMnO_x$@CC-Elektrode eine signifikant verbesserte Kapazitätserhaltung. Die maximale Energiedichte betrug 72,8 µWh cm^{-2}, während die maximale Leistungsdichte 17,0 mW cm^{-2} erreichte. Zugleich wies das quasi-festkörperbasierte Gerät auf Basis der $NiMnO_x$@DC-Elektroden eine ausgezeichnete mechanische Flexibilität in Biegetests auf.

Zusammenfassend präsentiert diese Arbeit einen systematischen und schrittweisen Ansatz von DC zu $NiMnO_x$@DC, der die Vorteile von CC, BDD und Ni–Mn-Oxiden wirksam integriert. Diese Strategie ermöglicht die Herstellung leistungsstarker flexibler SCs, die nicht nur durch hohe Energiedichte und schnelle Leistungsabgabe, sondern auch durch exzellente Langzeitstabilität und mechanische Flexibilität überzeugen. Die erzielten Fortschritte bei den Elektrodenmaterialien leisten somit einen wesentlichen Beitrag zur praktischen Realisierung flexibler SCs für portable und tragbare elektronische Anwendungen.

Acknowledgements

It is with immense gratitude that I acknowledge the support and contributions of the many individuals and institutions who have made my doctoral journey not only possible but also profoundly meaningful.

Foremost, I would like to express my deepest and most sincere appreciation to Professor Xin Jiang for providing me with the invaluable opportunity to pursue my doctoral studies at the Chair of Surface and Materials Technology (LOT) at the University of Siegen. His continuous support, valuable advice, and profound insights have been essential to the completion of this dissertation. His guidance in both academic research and personal development has greatly shaped my PhD journey. I feel truly honored to have been a member of his group.

Equally, I wish to extend my heartfelt gratitude to Professor Nianjun Yang (from Hasselt University), whose role in my PhD study has been just as important. With his remarkable expertise and unwavering patience, he has guided me closely through the concrete progress of my research and offered invaluable suggestions at every critical stage. His mentorship has been a constant source of motivation, and his insights were crucial to the progress and completion of this work. Beyond academics, he has also given me generous help in daily life, for which I am deeply grateful. To me, Prof. Yang has been not only a supervisor but also a mentor and a friend, whose encouragement and trust constantly strengthened my determination to move forward.

I am truly indebted to all my colleagues at LOT, whose assistance and collaboration have greatly enriched my PhD life. I particularly thank Ximan Dong, Dr. Xinyue Chen, and Yao Li for their helpful suggestions in research and the time we shared during my stay in Siegen. My special thanks go to Dr. Chuyan Zhang and Dr. Zhaofeng Zhai for their enlightening discussions and insightful advice, in particular thanks to Dr. Zhai for his support with HRTEM analysis. I am also grateful to Andrea Brombach for her kind and efficient assistance with administrative and daily matters. I sincerely appreciate the help of Claudia Kretzer and Stefan Wagener for their constant support with laboratory conditions, and Petra auf dem Brinke for her help with SEM and EDX characterizations. I wish to thank Dr. Michael Vogel and Dr. Aleksandr Zubtsovskii for their valuable guidance with PVD techniques, Tianxiao Guo for his support

with MWCVD equipment, and Dr. Hameed Ullah for sharing his expertise on MnO_x synthesis. Further thanks go to Dr. Thorsten Staedler, Dr. Kevin Suta, Dr. Akif Zeb, Bharath Reddy Lakki Reddy Venkata, and Chen Wang for their various support.

Beyond LOT, I also gratefully acknowledge the collaboration from other research groups. I am indebted to Professor Holger Schönherr and his group for their assistance with XPS characterization, to Markus Hartmann from the group of Professor Robert Brandt for his help with XRD characterizations, to Andrea Born for her support with BET surface area measurements, and to Felix Thiel for his assistance with Raman spectroscopy.

During my research stay at Hasselt University in Belgium, I would like to sincerely thank the BOF project for its valuable support, as well as Professor Ken Haenen for his valuable assistance. I am also grateful to Shuang Liu, Yasamin Shajirati, and other colleagues who kindly helped me during my stay there. In addition, I would like to thank Professor Quanhong Yang from Tianjin University for his generous support in strengthening the collaboration with Hasselt University.

This work has been financially supported by the Deutsche Forschungsgemeinschaft, to which I am truly grateful. Without such support, this dissertation would not have been possible.

Last but certainly not least, I would like to thank my family for their continuous encouragement and understanding. I am deeply grateful to my wife, Fengjun Li, for her loving care, boundless patience, and unwavering support throughout this journey. My heartfelt thanks also go to my parents and my parents-in-law, whose love, understanding, and constant encouragement have always given me the strength to pursue my academic career. I also thank my beloved cats, Miaobao, Benben, and Kuikui, who have accompanied me with warmth and joy throughout doctoral studies.

To all of you, I express my most sincere and profound gratitude.

Publication list

1. Li C, Dong X, Zhai Z, Huang N, Jiang X, Yang N. High-Performance Flexible Supercapacitors Using Diamond Cloth. *The Journal of Physical Chemistry C*. **2025**,129(14):6618-27.

2. Li C, Jiang X, Yang N. Synthesis, Surface Chemistry, and Applications of Non-Zero-Dimensional Diamond Nanostructures. *Small*. **2024**, 20(50):2400798.

3. Xu J, Li C, Yu S, Wang Z, Pritzel C, Jiang X, Yang N. Flexible Carbon Cloth Supercapacitors with High Power and Energy Densities. *Energy Technology*. **2023**,11(8):2300214.

Contents

Symbol List ..... **IV**

Abstract ..... **XI**

1 Introduction **1**

1.1 Electrochemical energy storage 1

1.2 Energy storage mechanisms of supercapacitors 3

1.2.1 Electric double-layer capacitors 4

1.2.2 Pseudocapacitors 7

1.3 Performance evaluation of supercapacitors 11

1.4 Electrode materials 13

1.4.1 Carbon cloth as a flexible substrate 13

1.4.2 Boron-doped diamond films 15

1.4.3 $NiMnO_x$ Pseudocapacitive Electrodes 18

1.5 Electrolytes 20

1.6 Motivation of the thesis 23

1.7 Overview of the thesis 26

2 Experimental **29**

2.1 Material preparation techniques 29

2.1.1 Radio frequency physical vapor deposition 29

2.1.2 Microwave plasma enhanced chemical vapor deposition 29

2.1.3 Hydrothermal synthesis 31

2.1.4 Electrodeposition 32

2.2 Electrode materials synthesis 32

2.2.1 Flexible diamond cloth 32

2.2.2 $NiMnO_x$-coated carbon cloth 34

2.2.3 $NiMnO_x$-coated diamond cloth 37

2.3 Characterization 38

2.3.1 Morphology and structural characterization 38

2.3.2 Phase and component analysis 38

2.4 Electrochemical measurements 39
2.4.1 Cyclic voltammetry 40
2.4.2 Galvanostatic charging-discharging technique 42
2.4.3 Electrochemical impedance spectroscopy 44
2.4.4 Mechanical flexibility 45
3 Flexible Diamond Cloth electrode 46
3.1 Optimization of BDD film deposition 47
3.1.1 Influence of the titanium interlayer 47
3.1.2 Seeding process 49
3.1.3 Influence of deposition temperature 50
3.2 Characterization of diamond cloth 51
3.3 Electrochemical performance of diamond cloth 57
3.3.1 Three-electrode system 57
3.3.2 Two-electrode system 63
3.3.3 Energy and power density 67
3.3.4 Mechanical flexibility and stability 69
3.4 Conclusions 70
4 $NiMnO_x$-Coated Carbon Cloth 72
4.1 Comparison of hydrothermal synthesis and electrodeposition 72
4.2 Incorporation of nickel 75
4.3 Characterization of $NiMnO_x$-coated carbon cloth 79
4.4 Performance of $NiMnO_x$-coated carbon cloth electrode 84
4.5 Conclusions 87
5 $NiMnO_x$-Coated Diamond Cloth 89
5.1 Substrate-dependent performance of $NiMnO_x$ 90
5.2 Influence of deposition potential 92
5.3 Pseudocapacitive performance of $NiMnO_x$-coated diamond cloth 101
5.3.1 Pseudocapacitive performance using a three-electrode system 101
5.3.2 Electrochemical performance using a two-electrode system 105
5.3.3 Energy density and power density 108

5.4 Flexible supercapacitors from $NiMnO_x$-coated diamond cloth 110
5.5 Conclusions 112
6 Summary and Perspectives 114
7 References 118

Symbol List

Abbreviations

3D	three-dimensional
BDD	boron-doped diamond
BE	binding energy
BET	Brunauer-Emmett-Teller
CC	carbon cloth
CF	carbon fiber
CFC	carbon fiber cloth
CNF	carbon nanofiber
CNT	carbon nanotube
CV	cyclic voltammetry
CVD	chemical vapor deposition
DC	diamond cloth
DFT	density functional theory
EDLC	electric double-layer capacitor
EDX	energy-dispersive X-ray spectrometer
EES	electrochemical energy storage
EIS	impedance spectroscopy
EV	electric vehicle
fCC	functional carbon cloth
FESEM	field-enhanced scanning electron microscopy
FFT	fast Fourier Transform
GCD	galvanostatic charging-discharging
HFCVD	hot filament chemical vapor deposition
HRTEM	high-resolution transmission electron microscopy
IHP	inner Helmholtz plane
LIB	lithium-ion battery
LIG	laser-induced graphene

MWCVD	microwave plasma enhanced chemical vapor deposition
ND	nanodiamond
OHP	outer Helmholtz plane
PC	pseudocapacitor
PVD	physical vapor deposition
RF-PVD	radio frequncy physical vapor deposition
rGO	reduced graphene oxide
SC	supercapacitor
SiNW	silicon nanowire
sp^2	sharp-principle-two
sp^3	sharp-principle-three
XAS	X-ray absorption spectroscopy
XPS	X-ray photoelectron spectroscopy
XRD	X-ray diffraction

Chemicals

Ag	silver
AgCl	silver chloride
Al	aluminum
APS	ammonium persulfate
Ar	argon
Au	gold
B	boron
C	carbon
CH_4	methane
Co(OH)2	cobalt(II) hydroxide
Cu	copper
$Fe(CN)_6^{3-}$	ferricyanide ion
$Fe(CN)_6^{4-}$	ferrocyanide ion

H^+	hydrogen ion
H_2	hydrogen gas
H_2O	water
H_2SO_4	sulfuric acid
I^-	iodide(I) ion
I_3^-	triiodide ion
$K_3Fe(CN)_6$	potassium ferricyanide
$K_4Fe(CN)_6$	potassium ferrocyanide
KCl	potassium chloride
$KMnO_4$	potassium permanganate
KOH	potassium hydroxide
Mn	manganese
$Mn^{2+}/Mn^{3+}/Mn^{4+}$	manganese(II)/(III)/(IV) ion
Mn_2O_3	manganese(III) oxide
Mn_3O_4	manganese(II,III) oxide
MnO	manganese(II) oxide
MnO_2	manganese dioxide
MnOOH	manganese oxide-hydroxide
MnO_x	manganese oxides
$MnSO_4$	manganese sulfate
MoS_2	molybdenum disulfide
Na^+	sodium ion
Na_2SO_4	sodium sulfate
Ni	nickel
$Ni(CH_3COO)_2$	nickel(II) acetate
Ni^{2+}/ Ni^{3+}	nickel(II)/(III) ion
Ni-Mn oxides	nickel-doped manganese oxides
$NiMnO_x$	nickel-doped manganese oxides
NiO	nickel(II) oxide

O	oxygen
PANI	polyaniline
Pb	lead
PMA	polyacrylamide
Pt	platinum
PVA	polyvinyl alcohol
Si	silicon
$TEABF_4$	tetraethylammonium tetrafluoroborate
Ti	titanium
TiC	titanium carbide
TiO_2	titanium dioxide
TiS_2	titanium disulfide
TMB	trimethylborane
T-Nb_2O_5	orthorhombic niobium pentoxide

Symbols

Δt	charging and discharging time
A	geometric area of effective capacitor electrode
C	capacitance
C_D	capacitance from diffusion layer
C_{dl}	electric double-layer capacitance
C_g	gravimetric specific capacitance
C_H	Helmholtz layer capacitance
C_s	areal specific capacitance
$C_{s,CV}$	areal specific capacitance calculated through CV
$C_{s,GCD}$	areal specific capacitance calculated through GCD
C_{sc}	specific capacitance
C_v	volumetric specific capacitance
E	energy density

E_g	gravimetric energy density
E_l	lower potential limit
E_{pa}	anodic peak potential
E_{pc}	cathodic peak potential
E_u	upper potential limit
E_v	volumetric energy density
i	current
i_{pa}	anodic peak current
i_{pc}	cathodic peak current
P	power density
P_g	gravimetric power density
P_v	volumetric power density
R_{ct}	charge transfer resistance
R_s	electrolyte resistance
t	time
V	voltage or potential
v	scan rate
Z	impedance
Z'	real part of impedance
Z''	imaginary part of impedance
Z_w	Warburg impedance
ΔQ	charge acceptance
Δt_{dc}	discharging time
ΔU	potential change
ΔV	voltage or potential change
θ	centerline-to-face angle
λ	wavelength
Φ	diameter

Units

°	degree
μF cm^{-2}	microfarad per square centimeter
Å	angstrom
A g^{-1}	ampere per gram
atom-%	atomic percent
°C	degree Celsius
C g^{-1}	coulomb per gram
cm^{-1}	per centimeter
cm^{-3}	per cubic centimeter
eV	electron volt
F cm^{-3}	farad per cubic centimeter
F g^{-1}	farad per gram
g	gram
g L^{-1}	gram per liter
g mL^{-1}	gram per microliter
GHz	gigahertz
GWh	gigawatt hour
h	hour
Hz	hertz
kHz	kilohertz
kV	kilovolt
M	moles per liter
m^2 g^{-1}	square meters per gram
mA	microampere
mA cm^{-2}	microampere per square centimeter
mF cm^{-2}	microfarad per square centimeter
MHz	megahertz
min	minute

mL	microliter
mm	micrometer
mM	micromoles per liter
mV s^{-1}	microvolt per second
mW	microwatt
mW cm^{-2}	mictrowatt per square centimeter
nm	nanometer
ppm	parts per million
s	second
sccm	standard cubic centimeters per minute
V	volt
V s^{-1}	volt per second
W	watt
W cm^{-3}	watt per cubic centimeter
W kg^{-1}	watt per kilogram
µm	micrometer
µW cm^{-2}	microwatt per square centimeter
µWh cm^{-2}	microwatt hour per square centimeter

Abstract

Supercapacitor (SC), one of the most important classes of electrochemical energy storage devices, has attracted considerable attention due to their high power density, fast charging-discharging capabilities, superior cycling stability, and reliable performance. With the rapid advancement of portable and wearable electronics, the demand for high-performance flexible SCs has significantly intensified, thereby driving extensive research into advanced electrode materials, electrolytes, and device architecture. Among them, the development of electrode materials plays a decisive role in determining both electrochemical performance and mechanical flexibility of SCs.

Herein, three electrode systems were designed and fabricated in this thesis: flexible diamond cloth (DC), $NiMnO_x$-coated carbon cloth ($NiMnO_x$@CC), and $NiMnO_x$-coated diamond cloth ($NiMnO_x$@DC). Their electrochemical performance was further and comprehensively evaluated by means of various techniques and tools. More details ae demonstrated as follows.

The flexible DC was synthesized through the overgrowth of a boron-doped diamond (BDD) film on CC in a microwave plasma enhanced chemical vapor deposition (MWCVD) reactor. A Ti interlayer was first introduced to protect CC from plasma etching while simultaneously enhancing BDD adhesion. The DC electrode demonstrated excellent electrochemical performance, including enhanced capacitance, good rate performance, and exceptional cycling stability. A symmetric pseudocapacitor (PC) assembled from two DC electrodes delivered an energy density of 45.96 μWh cm^{-2} at a power density of 4.25 mW cm^{-2}, retaining 17.64 μWh cm^{-2} at 67.93 mW cm^{-2}. Moreover, the symmetric DC electric double-layer capacitor (EDLC) exhibited excellent mechanical flexibility.

Pseudocapacitance was then introduced by electrochemical synthesis of Mn-oxide films on CC. This $NiMnO_x$@CC electrode offered better conformality, thickness control, and reproducibility compared with electrodes prepared through hydrothermal methods. The optimized Ni-doped electrode exhibited larger current responses, a wide potential

window (1.5 V), and distinct redox peaks, yielding a specific capacitance of 47.1 mF cm^{-2} at a scan rate of 10 mV s^{-1} and 42.8 mF cm^{-2} at a current density of 1 mA cm^{-2} in 1.0 M Na_2SO_4, with > 98.5 % coulombic efficiency over 10,000 cycles. Its cycling retention was limited (≈ 16% after 10,000 cycles), constraining practical application.

CC was further replaced with DC as the substrate to produce a more stable $NiMnO_x$@DC electrode. The optimal deposition potential of 1.0 V balanced deposition rate and side reactions. The as-fabricated $NiMnO_x$@DC electrode exhibited pronounced redox features and high specific capacitances of 180.5 mF cm^{-2} at a scan rate of 10 mV s^{-1} and 228.1 mF cm^{-2} at a current density of 2 mA cm^{-2}, coupled with exceptional coulombic efficiency approaching 100 % over 10,000 charging-discharging cycles. Furthermore, the $NiMnO_x$@DC electrode exhibited significantly enhanced capacitance retention in comparison to the $NiMnO_x$@CC electrode. The maximum energy density of 72.8 μWh cm^{-2} and maximum power density of 17.0 mW cm^{-2} were obtained for a symmetric $NiMnO_x$@DC PC. Simultaneously, the quasi-solid-state device using the $NiMnO_x$@DC electrodes showed excellent mechanical flexibility during the bending tests.

In summary, this thesis presents a systematic and stepwise route to design different SC electrodes from DC to $NiMnO_x$@DC, effectively integrating the advantages of CC, BDD, and Ni–Mn oxides. This strategy enables the fabrication of high-performance flexible SCs, which exhibit not only high energy density and rapid power delivery but also excellent long-term stability and mechanical flexibility. These advancements in electrode materials significantly contribute to the realization of practical applications for flexible SCs in portable and wearable electronic devices.

1 Introduction

1.1 Electrochemical energy storage

The growing scarcity of energy resources and the escalating tension between energy consumption and environmental preservation have emerged as the most pressing challenges for sustainable development in the 21st century. In recent decades, the development of environmentally friendly clean energy sources, such as solar energy, wind power, hydropower, and nuclear power, is one of the most effective ways to alleviate such issues. Consequently, the global transition toward sustainable energy systems and electrified transportation has intensified the demand for efficient energy storage devices. Taking electrochemical energy storage (EES) as an example, it converts chemical energy into electrical energy and vice versa, playing a vital role in modern energy systems and has been widely employed in various applications, such as portable electronic devices, electric vehicles (EVs), and large-scale grid integration.[1]

Generally, EES systems can be categorized into two primary types: batteries and supercapacitors (SCs). The main performance characteristics of different EES devices presented in the form of their Ragone plot, are shown in **Figure 1.1.**[2] One can see clearly that lithium-ion batteries (LIBs), which are widely used for EVs and portable electronic devices today, possess many advantages, such as a high operating voltage, an extended cycle life, and a high energy density.[3] The global shipments of LIBs are estimated to reach 439.32 GWh by 2025.[4] However, LIBs still have several shortcomings including relatively slow charging rate, and low thermal stability and flame point.

Development of SCs is an alternative to partially address these challenges. SCs, also known as electrochemical capacitors, have garnered significant attention due to their unique ability to bridge the gap between conventional capacitors and rechargeable batteries. SCs are characterized by their ability to deliver high power density, rapid charging and discharging rates, exceptionally long operational lifespans, and reliable performance.[5,6] These attributes render them highly promising candidates for a wide

range of applications. Despite their advantages, a major limitation of SCs is their relatively lower energy density compared to that of lithium-ion batteries.[7,8] Therefore, enhancing the energy density of SCs is substantially crucial to fulfilling a broader range of applications.

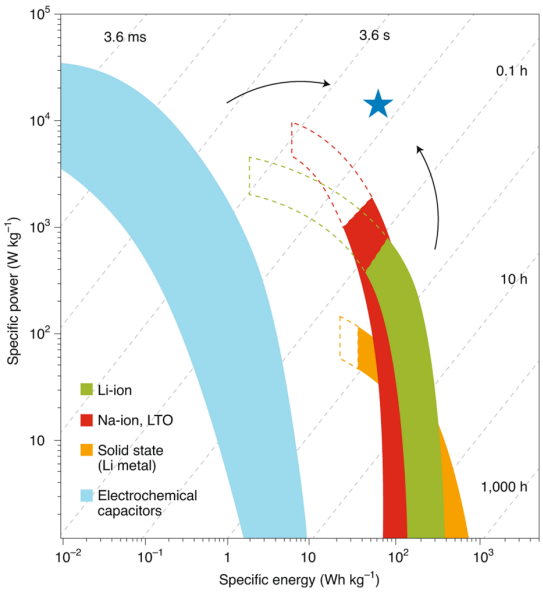


Figure 1.1. *Ragone plot of main EES devices in terms of the specific power density against specific energy density. The arrows show the development trends of the specific power density and specific energy density of EES devices approaching the star symbol. LTO refers to lithium titanium oxide ($Li_4Ti_5O_{12}$). Reproduced with permission.*[2] *Copyright © 2020, Springer Nature Limited.*

The first electrochemical capacitor was developed and patented by Becker in 1957.[9] Initial designs were based on porous carbon electrodes and aqueous electrolytes, which offered the modest energy densities but high reliability. Since then, SCs have undergone significant advancements and transformations that have solidified their importance in advanced energy storage technologies stemming from the breakthroughs in materials science and electrochemistry.[5,7,10,11]

A SC is mainly composed of current collectors, electrode materials, and an electrolyte.

Electrode materials are one of the most crucial components of SCs. Various materials, such as activated carbon, metal oxides, and conducting polymers, have been developed and utilized as capacitor electrodes to enhance their performance.[12–14] Among various materials explored, carbon-based electrodes have garnered particular attention due to their remarkable chemical stability, high specific surface area, excellent electrical conductivity, tunable pore structure, and long-term durability.[15,16] These outstanding properties make carbon materials extremely suitable for development of high-performance SCs.

In addition to conventional performance metrics of SCs, such as cycling stability, energy density, and power density, the rapid growth of flexible and wearable electronics has introduced a new critical requirement: mechanical robustness and flexibility.[17–20] As portable and wearable devices (e.g., smart textiles, health-monitoring electronics, and foldable displays) become increasingly prevalent, the demand for energy storage components that can withstand bending, twisting, and repeated mechanical deformation without significant performance degradation has surged.[21–23] The realization of high-performance flexible SCs critically depends on the design and fabrication of flexible electrode materials that possess not only excellent electrochemical performance but also exceptional mechanical durability. The following section discusses the fundamental energy storage mechanisms, providing the significant theoretical foundation for the electrode design strategies presented in this thesis.

1.2 Energy storage mechanisms of supercapacitors

To rationally design flexible SCs, it is essential to understand their underlying energy storage mechanisms. SCs store energy through mechanisms fundamentally different from those employed in conventional batteries. Generally, SCs can be classified into two categories based on their two energy storage mechanisms: electric double-layer capacitors (EDLCs) and pseudocapacitors (PCs). An ECLC involves the storage and release of energy through the rapid adsorption and desorption of ions at the interface between the

electrode material and the electrolyte.[24] Most carbon-based SCs are based on this mechanism. Whereas energy storage of a PC is achieved from fast faradaic electron/charge transfer (or redox reactions), intercalation, or electrosorption taking place on the surface of used capacitor electrodes und the applied potential.[16,25]

1.2.1 Electric double-layer capacitors

EDLCs store energy through the physical separation of charge at the interface between the electrode material (typically high-surface-area carbon) and the electrolyte. When a voltage is applied, the ions from the electrolyte migrate and accumulate on the electrode surface to form a nanoscale electrochemical double-layer. This process involves purely physical adsorption/desorption of ions without redox reactions (i.e., *via* no faradaic process). Therefore, EDLCs exhibit extremely fast charging and discharging rates and are capable of storing and releasing a significant amount of energy per unit time, resulting in high power density. Meanwhile, the cycling life of EDLCs is theoretically supposed to be unlimited.

The electric double-layer theory was first expressed and presented in the 19th century by Hermann Von Helmholtz during the investigation of colloidal suspensions, which was known as Helmholtz double-layer model (**Figure 1.2a**).[26] Two dense layers of opposite charge are formed at the interface of an electrode and an electrolyte. They are further separated by a nanoscale distance. The electric double-layer plays a role that is approximate to the dielectric layer in a conventional two-plate capacitor. In the early 20th century, the Helmholtz model was further refined by Louis G. Gouy and David L. Chapman, who considered that ions (both anions and cations) are continuously distributed in the electrolyte solution due to thermal motion (**Figure 1.2b**).[27,28] The layer was proposed as a diffuse layer in the Gouy-Chapman model. However, the capacitance calculated using the Gouy-Chapman model was overestimated because of the assumption of point charges and their extremely small distance from the electrode surface under high potential. Therefore, by taking the size of ions into account, Otto Stern integrated the Helmholtz model and the Gouy-Chapman model to propose the Stern model (**Figure 1.2c**) in 1924.[29] In this model, some ions adsorb onto the electrode surface, forming an inner

static Helmholtz layer, while others constitute a Gouy-Chapman diffuse layer. The capacitance C_{dl} of an EDLC calculated using the Stern model consists of two parts connected in series: capacitance C_H from the Helmholtz layer and C_D from the diffusion layer. Their relationship can be expressed by the following equation:

$$\frac{1}{C_{dl}} = \frac{1}{C_H} + \frac{1}{C_D} \tag{1.1}$$

Note that the surfaces of cations and anions in the electrolyte are actually surrounded by solvent molecules, forming solvated ions. These solvated ions serve as the actual charge carriers. Based on that, David C. Grahame improved the stern model in 1947.[30] It has been taken into account that the solvated ions might lose their solvation shell as they approach an electrode. The proposed Helmholt layer in the Stern model was separated into the inner Helmholtz plane (IHP) and the outer Helmholtz plane (OHP) (**Figure 1.2c**).

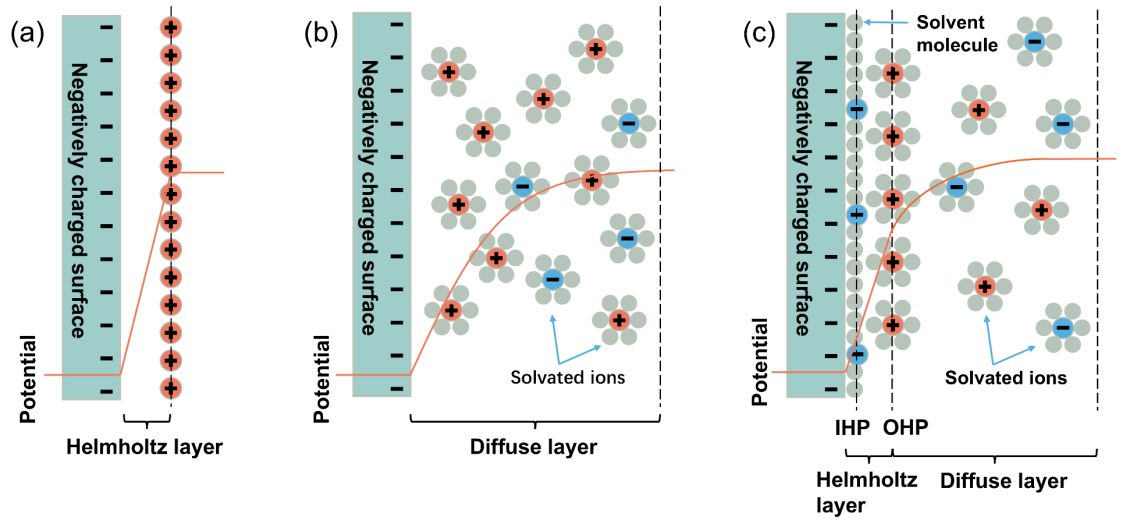


Figure 1.2. *Schematic representations of the electric double-layer near a negatively charged electrode in an aqueous electrolyte: (a) the Helmholtz model, (b) the Gouy-Chapman model, (c) the Stern model. IHP refers to the inner Helmholtz plane and OHP refers to the out Helmholtz plane.*

Based on the classical electric double-layer theoretical models described above, the specific capacitance of an (e.g., carbon-based) EDLC is expected to be proportional to

the specific surface area of the used electrode. However, for porous carbon materials, this assumption does not hold true. The insufficient wettability of porous electrode materials in the electrolyte solution results in a reduced accessible surface area to electrolyte ions for the formation of electric double-layer, thereby causing the specific capacitances to be lower than theoretically expected ones.[31] In addition, the pore size of porous carbon materials strongly influences the capacitance of EDLCs. In macropores, minimal curvature allows the Stern model to describe charge storage effectively. In micropores, however, ion behavior becomes more complex. Chmiola *et al.* found that the specific capacitance of carbide-derived carbons exhibited an anomalous increase when the pore size was below 1 nm (**Figure 1.3a**).[32] This contradicts the conventional view that capacitance decreases continuously with pore size. At sub-nanometer scales, solvated ions partially shed their solvation shell (**Figure 1.3b, 1.3c, and 1.3d**), thereby shortening the distance between ions and electrode surface and enhancing capacitance. Thus, the optimal pore size for maximizing capacitance tends to match the desolvated ion size rather than the solvated one.

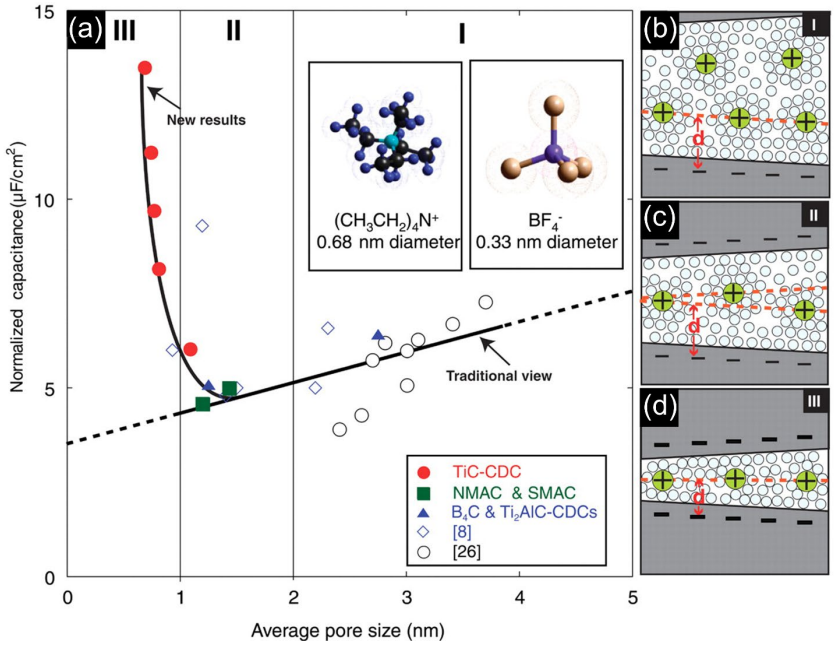


Figure 1.3. *(a) Graph depiction of the specific capacitance against average pore size of four carbon material electrodes using the same electrolytes. (b—d) Schematic illustrations of solvated ions located within pores with varying distances between*

adjacent pore walls: (b) greater than 2 nm, (c) between 1 and 2 nm, and (d) less than 1 nm, visually explaining this behavior.[32] *Copyright © 2006 American Association for the Advancement of Science.*

The development of various electric double-layer models has significantly advanced the understanding of the energy storage mechanisms in EDLCs and plays an important role in enhancing the electrochemical performance of carbon-based materials. Factors influencing the energy storage performance of EDLCs are intricate and multifaceted, such as the wettability and microstructure of the electrodes, the type of electrolyte ions, and the interaction between ions and electrode. Consequently, the exploration of efficient electrode materials and the careful selection of appropriate electrolytes are essential for achieving high-performance EDLCs. Overall, further research is necessary to elucidate the fundamental mechanisms underlying electric double-layer energy storage. Ultimately, a comprehensive understanding of all contributing factors will facilitate the design of next-generation EDLCs with their superior performance.

1.2.2 Pseudocapacitors

The concept of pseudocapacitance was initially introduced by B.E. Conway.[33] In contrast to EDLCs, which store energy through pure electrostatic adsorption of ions, pseudocapacitors (PCs) store energy involving a Faradaic process, namely fast and highly reversible redox reactions on the surface or near-surface of the electrodes. The charge transfer of PCs is argued to be similar to the process in batteries. However, for thermodynamic reasons, there exists a linear relationship between charge acceptance (ΔQ) and the change in potential (ΔV). This results in the derivative dQ/dV being equivalent to a capacitance. Generally, PCs can achieve a higher capacitance and a greater energy density due to the additional contribution of their pseudocapacitances compared to EDLCs. Their power density and energy density are usually between those of EDLCs and LIBs.[34]

Clearly, electrode materials are the core components of various PCs. Among numerous electrode materials, typical pseudocapacitive materials include transition metal oxides (e.g., ruthenium oxide, manganese oxide, and vanadium nitride), conducting polymers (e.g., polyaniline, polypyrrole), and surface-functionalized carbons containing redox-active heteroatoms (e.g., oxygen, nitrogen).[35]

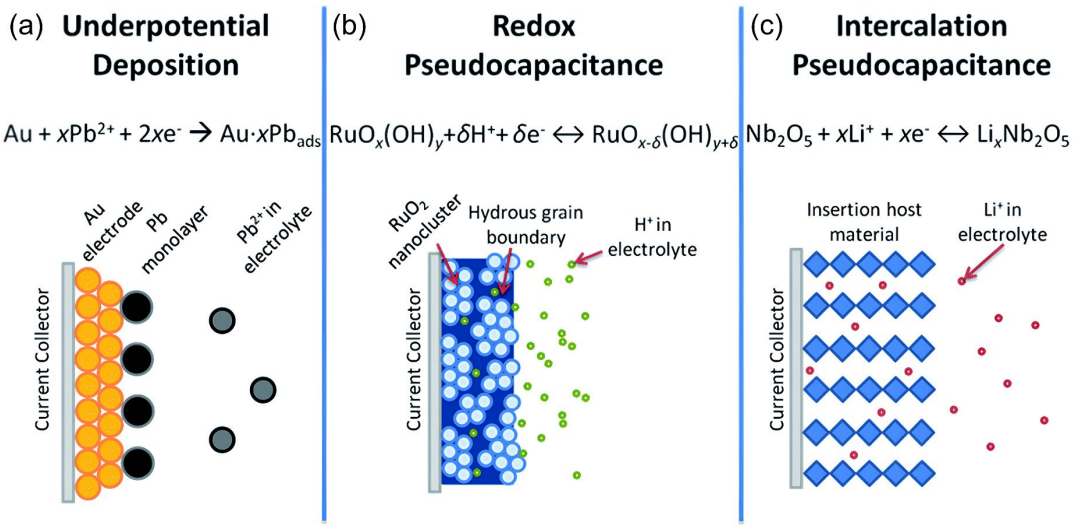


Figure 1.4. *Illustration of three types of pseudocapacitance mechanisms: (a) underpotential deposition, (b) redox pseudocapacitance, and (c) intercalation pseudocapacitance. Reproduced with permission.* [36] *Copyright © 2014 Royal Society of Chemistry.*

Based on charge storage mechanisms of the applied electrode materials, pseudocapacitance can be categorized into the following three types as illustrated in **Figure 1.4**: (1) underpotential deposition, (2) surface redox pseudocapacitance, and (3) intercalation pseudocapacitance.[33,36] Underpotential deposition refers to the deposition of atomic monolayers of a metal from its cationic solution onto a dissimilar metal substrate under a higher redox potential (**Figure 1.4a**). A characteristic example of underpotential deposition is the deposition of lead (Pb) on gold (Au).[37,38] This process is rarely utilized for the preparation of high-performance PCs owing to its limited potential window, which leads to relatively low capacitance, as well as the high cost associated with noble metals.

By contrast, the surface redox pseudocapacitance is more prevalent. It arises from the rapid and reversible redox reactions between the electrode and the electrolyte. Typically, ruthenium oxide demonstrates redox pseudocapacitance primarily because of the rapid charge transfer enabled by its high conductivity (**Figure 1.4b**).[39] In literature, metal oxides and conducting polymers have been more frequently shown to exhibit pseudocapacitive behavior because their multiple oxidation states facilitate rapid redox reactions. The intercalation pseudocapacitance originates from the fast intercalation of ions from the electrolyte into tunnels, layers, and crystal structure of redox-active materials, where a faradic reaction occurs without any phase transformation (**Figure 1.4c**).[40] In comparison with LIBs, intercalation process of PCs is much faster due to the rapid diffusion of ions, thereby avoiding any phase transformation.[41] Intercalation pseudocapacitance materials, including MoS_2, $Co(OH)_2$, TiS_2, T-Nb_2O_5, and transition metal carbides, exhibit superior rate capability and extended cycle life in comparison to battery materials.[42] In addition, pseudocapacitive behavior has been observed in several battery materials.[43] To clarify this point, pseudocapacitive materials are further classified as intrinsic or extrinsic, depending on whether their pseudocapacitance is inherent or arises from nanostructuring, respectively.[36]

In addition to pseudocapacitive electrode materials, pseudocapacitance has been suggested to arise from redox-active electrolytes. These electrolytes contain redox-active species that are capable of undergoing reversible redox reactions during the charging-discharging cycles, thereby significantly enhancing the capacitance and energy density of SCs.[44,45] Redox-active electrolytes thus play a critical role by directly participating in fast electron transfer processes at the electrode-electrolyte interface. For instance, specific ionic liquids or aqueous solutions containing redox couples such as $Fe(CN)_6^{3-}/Fe(CN)_6^{4-}$ or I_3^-/I^- provided additional pseudocapacitive contributions.[44,46] This is because these redox-active ions adsorb onto the electrode surface and engage in faradaic reactions, which effectively enhance the energy density without relying solely on the intrinsic properties (mainly capacitive performance) of the electrode materials (**Figure 1.5**). The primary advantage of utilizing redox-active electrolytes for the construction of PCs lies

in their flexibility in selection of electrode materials and redox species.[46] Thus, the electrochemical performance becomes tunable, enabling the adjustment to parameters such as operating voltage windows and the ionic conductivity. However, several challenges limit their practical applications. These disadvantages encompass the potential for internal and fast self-discharging rates caused by the shuttling of mobile redox species, losses of active species due to diffusion overvoltage, and reduced cycling stability resulting from the cross-mixing of redox couples.[47,48] To mitigate these limitations different strategies have been applied, including using redox-active species like heptyl viologen and bromide that adsorb onto electrodes to suppress diffusion and self-discharging, and applying a Nafion membrane as separator to prevent self-discharging *via* redox shuttling.[47,49]

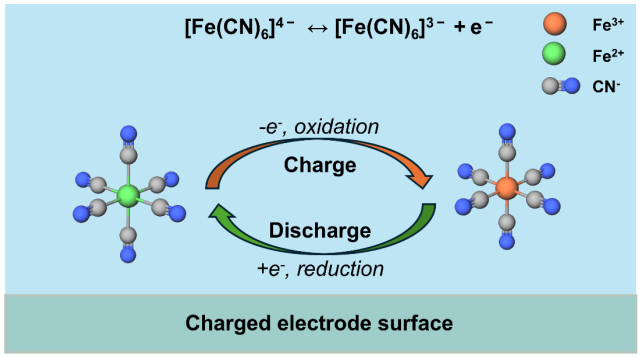


Figure 1.5 *Mechanism representation of a PC using a redox-active electrolyte of ferricyanide/ferrocyanide.*

In summary, pseudocapacitance represents a distinct electrochemical energy storage mechanism that combines characteristics of both electric double-layer capacitance and battery-like charge storage. It involves Faradaic reactions that facilitate the storage of electrical energy *via* charge transfer mechanisms, analogous to processes observed in batteries, while maintaining the high power density and long cycle life typical of capacitive systems. An in-depth understanding of the underlying charge storage mechanisms involved in pseudocapacitive processes is essential and still required to

develop effective PCs, such as for enhancing the energy density and cycling performance of various SCs.

1.3 Performance evaluation of supercapacitors

The systematic evaluation of SC performance is essential for understanding their charge storage behavior and for assessing its practical applications. Typically, the performance of SCs is assessed through several key parameters including capacitance (or specific capacitance), energy density, power density, coulombic efficiency, and cycling stability (also known as capacitance retention). For flexible SCs, an additional bending test for assessment of mechanical flexibility needs to be taken into consideration as well.

Capacitance is a critical parameter that reflects the complete charge storage capability of a capacitive electrode. It is defined as the ratio of the change in charge adsorbed or released during the charging and discharging processes to the corresponding change in applied potential.[25,50] It can be expressed using the following equation:

$$C = \frac{\Delta Q}{\Delta U} \tag{1.2}$$

where ΔQ is the charge stored by an electrode and ΔU is the given potential. To compare the capacitance of different electrodes efficiently, the specific capacitance (C_{sc}) is introduced. There are three kinds of specific capacitance: area specific capacitance normalized by the working geometric area (C_s, mF cm^{-2}), volume specific capacitance normalized by the working volume of electrode (C_v, F cm^{-3}), and mass specific capacitance normalized by the weight of active electrode material (C_g, F g^{-1}).

Energy density refers to the amount of energy that is stored in the given system per given unit (i.e., area, volume, or mass). If a capacitor electrode possesses a high energy density, it means they have the capability to store a large amount of energy by a very small amount of mass or in a small space. The energy density of an EDLC, E, can be calculated according to the following equation:

$$E = \frac{1}{2} C_{sc} V^2 \tag{1.3}$$

in which V is the operational voltage. It should be noticed that the energy density is estimated based on the measurement of a two-electrode system.

Similar to energy density, the power density is the amount of power delivered within a specific unit. It is also an important parameter to describe the properties of SC performance. The power density is usually calculated by the following equation:

$$P = \frac{E}{\Delta t_{dc}} \tag{1.4}$$

where P is the power density, and Δt_{dc} is the discharging time.

As the above equations indicate, the primary approach to obtain high energy and power density in a SC is to enhance both its specific capacitance and the cell voltage. The capacitance can be effectively improved through the selection of efficient electrodes (materials), the incorporation of redox-active species, and the introduction of nanostructured features onto electrode surface. The working cell voltage is strongly influenced by the electrochemical stability window of both the electrolyte and the electrode materials. Consequently, improving both the cell voltage and the electrolyte's electrochemical stability window can lead to a substantial increase in the energy density of the resulting SCs.

In addition to power density and energy density, long-term cycling stability and coulombic efficiency are critical for practical applications of SCs. High-performance SCs must maintain a substantial fraction of their initial capacitance after thousands or even hundreds of thousands of charging-discharging cycles, with minimal degradation of the electrode or electrolyte. The cycling stability is exhibited through the ratio of the capacitance retention after certain number of charging-discharging cycles to the initial capacitance. The cycling stability is determined by several factors such as the type of SCs, the active electrode materials, the charging-discharging rate, the electrolyte, the given potential, and the temperature during testing.[51] Coulombic efficiency, defined as the ratio of the charge transferred in the discharging step to that in the charging process, reflects

the reversibility of the charge storage process and ideally approaches 100 % for a high-performance SC.

In addition to the performance parameters mentioned above, mechanical flexibility of SCs in some cases is a specialized evaluation parameter.[18,52] This performance directly affects the practicality of flexible SCs in wearable and flexible electronic devices. The electrochemical performance of flexible SCs is evaluated through bending, stretching, and/or twisting tests, which involve handling related SCs at various angles and after extended cycling cycles. Therefore, flexible substrates should accommodate strain without structural failure. Similarly, active materials need to have good adhesion to the substrates while retaining electrical connectivity and ion accessibility during repeated deformation. In addition, the electrolyte should be mechanically compatible, which is often addressed by using gel electrolytes that combine ionic conductivity with structural integrity.

1.4 Electrode materials

The selection of electrode materials significantly influences the overall electrochemical performance of SCs, encompassing key parameters such as specific capacitance, energy and power densities, and long-term cycling stability.[24] Ideal electrode materials are expected to exhibit high electrical conductivity, large specific surface area, electrochemical stability, and compatibility with the electrolyte. Moreover, in the context of wearable electronics, electrodes must further reconcile electrochemical efficiency with flexibility, lightweight design, and mechanical robustness. This section highlights three electrode materials relevant to this thesis: carbon cloth (CC) as a flexible substrate, boron-doped diamond (BDD) films, and manganese oxides.

1.4.1 Carbon cloth as a flexible substrate

Commercial CC has emerged as a widely used current collector and electrode substrate for flexible electrodes in energy harvesting and storage devices due to its unique

combination of properties.[53,54] Structurally, it is composed of carbon fibers (CFs), which collectively provide a three-dimensional (3D) porous architecture that enhances both mechanical flexibility and structural integrity. In contrast to rigid current collectors such as metal foils, the macroporous structure (pore diameter: 10—50 μm) of CC, with pore diameters typically ranging from 10 to 50 μm, allows for efficient electrolyte penetration, ensuring uniform ion distribution across the CC surface. Moreover, this open-pore framework can effectively accommodate mechanical deformation caused by bending, twisting, or repeated flexing without compromising structural integrity or electrochemical performance. The fibrous network of CC contributes to excellent electrical conductivity, low density, and high chemical stability, making CC particularly attractive for the applications requiring lightweight and durable components.[55,56] Moreover, the large surface area of the 3D CC electrode effectively lowers local current densities, leading to a more uniform distribution of the electric field. In addition, CC can be easily processed into various shapes of electrodes. These advantageous characteristics make CC especially suitable for its integration into wearable electronics and portable energy storage systems, where mechanical durability under dynamic conditions is essential.

However, a key limitation that restricts the CC applicability is the relatively low intrinsic capacitance, which stems from the factors such as its limited specific surface area, poor electrolyte wettability, and insufficient electrochemical activity.[53] Consequently, CC is typically used more frequently as a chemically stable and inert platform to grow or deposit a wide range of electroactive materials, such as metal oxides, conductive polymers, and carbon nanostructures.[53,56–59] The employed CC can be classified into two types (**Figure 1.6**): woven CC and non-woven CC. The woven CC (**Figure 1.6a**) consists of interlaced CFs that form a mechanically robust and flexible textile structure (**Figure 1.6b**). In contrast, non-woven CC (**Figure 1.6c**) is composed of CFs randomly distributed and held together by a polymer binder, typically polyvinyl alcohol (PVA) (**Figure 1.6d**). Although non-woven CC is typically lighter with respect to its weight, PVA has an undeniable drawback: it can be easily etched in a plasma atmosphere or dissolved in aqueous solutions, causing carbon fibers to scatter. This makes

non-woven CC less suitable for the construction of SCs. In contrast, the interwoven architecture of woven CC offers better mechanical integrity, chemical stability, and durability during synthesis and electrochemical cycling. In this thesis, woven CC was employed as a flexible and robust substrate for integrating electroactive materials, aiming to combine the structural advantages of CC with the high electrochemical performance of the active components.

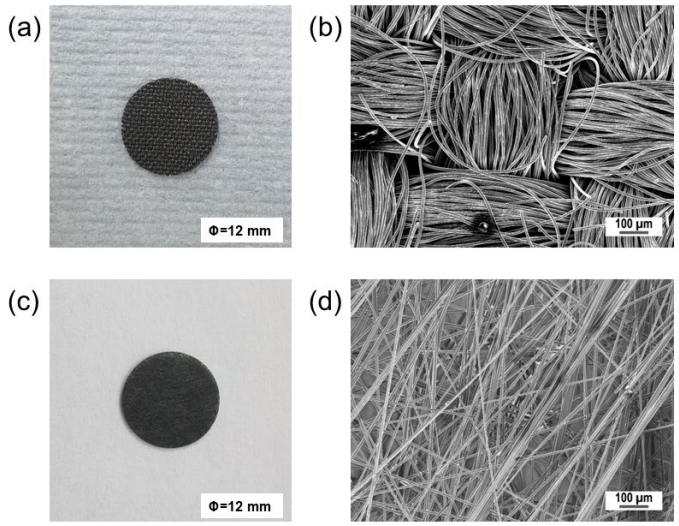


***Figure 1.6**. Two types of CC are presented: (a) Optical photograph and (b) microstructure of woven CC; (c) Optical photograph and (d) microstructure of non-woven CC.*

1.4.2 Boron-doped diamond films

Conductive diamond nanomaterials exhibit excellent electrochemical performance, making them promising candidates for use as capacitor electrodes.[11,60] Up to date, BDD appears to be the best choice among different doped diamond nanomaterials. As a capacitor electrode, BDD possesses a large potential window, good electrical conductivity, long-term stability, and superior chemical inertness.[61] A BDD electrode survives in 2 M H_2SO_4 within a voltage range of -35 to +6 V without structure damage.[62] Various BDD nanostructures (e.g., nanowires,[63] porous film,[64–66] network[67]) with enhanced specific surface areas have been meanwhile fabricated by use of different nanotechnologies (e.g.,

top-down, und bottom-up). These diamond nanomaterials have been applied as capacitor electrodes to form SCs in a wide variety of electrolytes. They exhibited outstanding chemical inertness, high capacitances, and extremely long cycling stability even in crucial conditions (e.g., high currents, voltages, or temperatures).[60] For example, a honeycomb-structured BDD EDLC delivered a specific capacitance of 3800 und 666 μF cm^{-2} in 1 M H_2SO_4 solution and organic 0.5 M tetraethylammonium tetrafluoroborate ($TEABF_4$) plus propylene carbonate solutions, respectively.[68] These capacitances were evaluated in three-electrode systems. A higher capacitance of a diamond electrode can be achieved once the effective surface area is enlarged, benefiting from the enhancement of surface defects or the higher number of active sites through boron doping. A highly porous diamond foam was applied as an EDLC electrode and showed a wide potential window of 2.5 V in aqueous solutions, a specific capacitance of 2.3 F cm^{-3} (or 0.598 mF cm^{-2}), and a power density of 807 W cm^{-3} at discharging rate of 1000 V s^{-1}.[69] The diamond-based EDLC demonstrator using the free-standing diamond paper as the electrode owned a capacitance of 0.688 mF cm^{-2} per layer of paper (or 0.645 F g^{-1}) in aqueous electrolytes. Thanks to the wide potential window of conductive diamond (e.g., up to 2.5 V) and the capacity of conductive diamond to be worked at high operation frequencies, the specific power density of this device attained to 10^5 W kg^{-1}.[70] A porous BDD network, formed *via* a template-free method, possessed hundreds of times larger (e.g., 490-fold enhancement for a 3 μm thick diamond network) surface area in comparison with a flat diamond film. The EDLC based on this diamond network displayed a capacitance of 13.7 F g^{-1} (or 17.3 F cm^{-3}) at a scan rate of 0.1 V s^{-1} in the H_2SO_4 aqueous solution.[67]

The radar plot (**Figure 1.7A**) exhibits the differences in the electrochemical performance of several SCs with diamond electrodes as measured by their maximum capacitive dimensions, including EDLCs, PCs and redox-electrolytes enhanced SCs (R-SCs) that were fabricated in our lab.[71] Several diamond electrode SCs could possess both high power and energy densities (**Figure 1.7B**). Their gravimetric energy density (E_g) and volumetric energy density (E_v) values are larger than those of most SCs with other material electrodes, and their gravimetric power density (P_g) and volumetric power

density (P_v) values are higher than those of batteries. Therefore, diamond nanomaterials are promising electrodes to improve the performance of SCs.

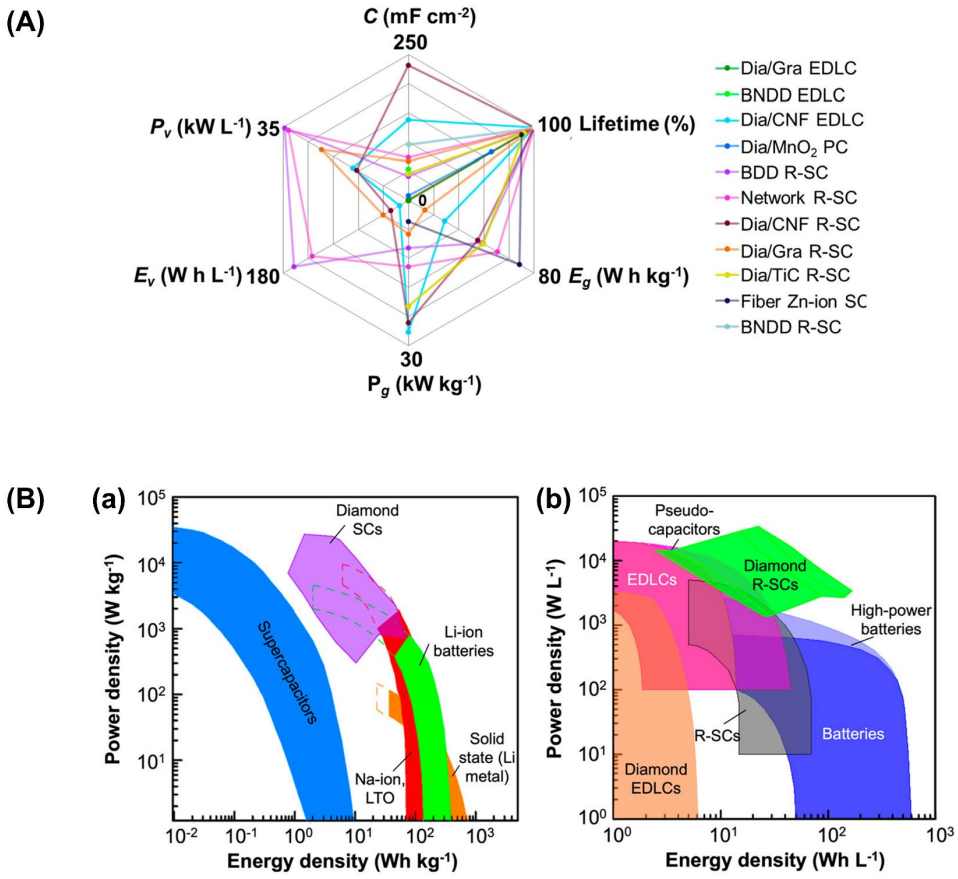


Figure 1.7. *(A) Radar plot of different diamond electrode SCs based on their maximum capacitances (C), lifetime, gravimetric power densities (P_g), volumetric power densities (P_v), gravimetric energy densities (E_g), and volumetric energy densities (E_v). (B) (a) Gravimetric Ragone plots and (b) volumetric ones of diamond electrode SCs in comparison with those of other energy storage devices. The abbreviations of LTO, R-SC, PDD, Dia/ Gra, BNDD, Dia/CNF, Dia/MnO_2, Network, Dia/TiC, and Fiber stand for lithium titanium oxide ($Li_4Ti_5O_{12}$), redox electrolyte-enhanced SC, phosphorus-doped diamond, diamond/graphite composites, boron-nitrogen co-doped diamond, diamond/carbon nanofibers, diamond/MnO_2 composite, diamond network, diamond/TiC composite, and diamond fibers, respectively. Reproduced with permission.*[71] *Copyright © 2023, American Chemical Society.*

Diamond SCs have been also constructed using hybrid diamond (carbon) materials, as these composites effectively combine the advantageous properties of both sp^2 and sp^3 carbon materials in capacitor electrode applications. Benefiting from the enlargement of surface areas of such hybrids and additional capacitance from sp^2 carbon, the enhancement of the capacitive performance of these hybrids is thus expected. Different hybrid diamond films with combinations of other sp^2 carbon materials have been investigated. For example, when BDD-coated carbon nanotubes (CNTs) was utilized as a hybrid EDLC electrode, it possessed a potential window of over 2.6 V together with a capacitance of up to 0.58 mF cm^{-2} in the phosphate buffer saline solution.[72] Another hybrid diamond film, which was synthesized by growing vertically aligned carbon nanofibers (CNFs) on a thin BDD films, has been utilized as an EDLC electrode and showed a capacitance of 137.9 mF cm^{-2} at a current density of 2 mA cm^{-2} in aqueous solutions.[73] Even after 10,000 charging-discharging cycles, its capacitance retention remained almost unchanged. Such outstanding capacitive performance mainly resulted from an enlarged surface area from the CNFs, the porous structure of a BDD film, high conductivity of this hybrid electrode, as well as its high stability.

In addition to being used as an electrode, BDD is also frequently utilized as an electrode support owing to its diverse surface chemistry and stable surface terminations, which facilitate the incorporation of pseudocapacitive materials (e.g., conjugated polymer, metal oxides, metal nitrides, metal carbides, and metal sulfides).[11,61,74] The integration of pseudocapacitive materials with diamond enables fast and reversible surface-controlled faradaic redox reactions at the electrode-electrolyte interface, facilitating additional electron and charge transfer, thereby significantly enhancing pseudocapacitance of SCs.[75] However, several critical challenges remain to be addressed in the development of diamond-based pseudocapacitive electrodes, such as the declined electrical conductivity, the limited operational lifespan, the detachment or depletion of pseudocapacitive materials, and the structural degradation of diamond pseudocapacitive composites.[11]

1.4.3 $NiMnO_x$ Pseudocapacitive Electrodes

As previously stated, transition metal oxides/hydroxides are proven to be one of the

primary categories of pseudocapacitive materials utilized in the fabrication of SCs. They have received significant attention as SC electrodes due to their multiple advantages, such as high specific capacitance, natural abundance, non-toxicity, environmental friendliness, cost-effectiveness, designable structure, and simple preparation.[76,77] Among them, manganese oxides (MnO_x) are particularly notable, thanks for their outstanding pseudocapacitive properties, excellent redox activity, diverse crystal structures, and collectively enhanced electrochemical performance. For example, MnO_2 is one of the most extensively studied manganese oxides due to its high theoretical capacitance of 1370 F g^{-1}.[78] Additionally, MnO_2 exhibits a wider operational potential window compared to other transition metal oxides, which contributes to a higher energy density.[79] Manganese oxides can be synthesized through either a hydrothermal method or electrodeposition.[80–84] Both methods are efficient processes and widely employed in the preparation of manganese oxides. Manganese, like other transition metals, exhibits the ability to form a range of stable oxide phases such as MnO, Mn_2O_3, MnO_2, and Mn_3O_4, which can adopt a variety of crystallographic structures.[85] Each of these manganese oxides exhibits unique structural arrangements, such as cubic, tetragonal, or orthorhombic crystal lattices, that significantly influence their physical and electrochemical properties. This structural versatility allows manganese oxides to exhibit a variety of characteristics of electrochemical performance when used as electrode materials. It has been demonstrated that the energy storage mechanism in manganese oxide-based SCs involves a combination of electric double-layer capacitance, arising from ion accumulation at the electrode-electrolyte interface, and pseudocapacitance resulting from charge transfer associated with the fast, reversible Mn^{3+}/Mn^{4+} redox reactions. Therefore, manganese oxides typically exhibit a high specific capacitance. For example, nanostructured MnO_2 that was electrodeposited onto graphene-functionalized textile substrates yielded a specific capacitance of 315 F g^{-1} at a scan rate of 2 mV s^{-1} in a 0.5 M Na_2SO_4 electrolyte solution.[86] Hydrothermally prepared manganese oxide (i.e., Mn_3O_4)/biomass porous carbon composite exhibited a high specific capacitance of 482 F g^{-1} at a current density of 0.5 A g^{-1} in the 6 M KOH aqueous solution.[87] However, the practical applications of MnO_x in SCs are often limited by its low electrical conductivity due to the wide band gap and

structural instability during prolonged cycling.[13] Fortunately, the disadvantage of their poor conductivity has been effectively mitigated to some extent by combining manganese oxides with conductive carbon nanomaterials that feature excellent electrical conductivity.

In addition to manganese oxides, nickel-based materials have garnered extensive research interest and have been systematically studied as promising pseudocapacitive electrode candidates. This is attributed to their notable theoretical specific capacitance, excellent thermal and chemical stability across different electrolytes, simple fabrication processes, and advantages such as low cost and environmental compatibility.[77,88] For example, nickel oxide (NiO) has been extensively studied as an electrode material for SCs due to its remarkable electrochemical activity, rich redox reactions, and a high theoretical capacitance of 2573 F g^{-1}.[89] To improve the electrical conductivity, the structural stability and the Na^+ storage capacity, nickel can be incorporated into manganese oxides to form Ni–Mn-based composite materials (i.e., $NiMnO_x$), which serve as promising electrode candidates for SC applications.[90,91] The integration of these components extended the potential window, improved the electrical conductivity, and enhanced the electrochemical activity for the electrode materials.[88,92] The enhanced performance is typically ascribed to the synergistic interaction among the transition metal constituents. For example, the carbon-coated Ni–Mn composite electrode exhibited a specific capacitance of 1863 F g^{-1} (671 C g^{-1}) at a current density of 1 A g^{-1}.[93] Another core-shell architecture using MnOOH as the core and NiO as the shell demonstrated a remarkable specific capacitance of 1890.5 F g^{-1} (1040 C g^{-1}) at a current density of 1.7 A g^{-1}.[94]

1.5 Electrolytes

Electrolytes play a pivotal role in determining the overall SC performance, as they govern the ionic conductivity, operating voltage window, energy density, power density, and cycling stability.[51,95] Fundamentally, electrolytes serve as the medium through which ions migrate between electrodes during charging and discharging processes, ensuring

charge neutrality, facilitating the formation of the electric double layer, and/or enabling Faradaic redox reactions in pseudocapacitive systems. An ideal electrolytes needs to feature a wide potential window, high ionic conductivity, high chemical and electrochemical stability, good compatibility with the employed electrodes, low sensitivity to working temperature variations, environmental sustainability, high operational safety, and cost-effectiveness. However, it is almost impossible to find such an electrolyte that meets all these requirements at the same time. Therefore, the selection of an electrolyte for SCs requires a balanced consideration of these factors (e.g., ionic mobility, chemical stability, compatibility with electrodes, and safety issues).

The main types of electrolytes used in SCs include aqueous, organic, solid-state or quasi-solid-state, and ionic liquid electrolytes.[96] Each type has its own distinct advantages and certain limitations. Organic electrolytes, as well as ionic liquid electrolytes, have a wider operating voltage window in comparison to aqueous electrolytes, thereby significantly enhancing energy density. For example, the operating voltage of a SC was increased from 0.9 V to 2.7 V by replacing aqueous electrolytes with organic alternatives.[97] The operating voltage window of an EDLC employing di-imidazolium ionic liquid-based electrolytes reached up to 3.2 V, thereby significantly improving the energy density.[98] Nonetheless, both organic electrolytes and ionic liquids are associated with several limitations. Organic electrolytes generally exhibit lower ionic conductivity and also raise safety concerns due to flammability and toxicity. In the case of ionic liquid electrolytes, their relatively high viscosity, which results in lower ionic conductivity, together with high cost and limited low-temperature performance, remain the main challenges for widespread practical applications. In recent years, solid-state and quasi-solid-state electrolytes have garnered considerable interest for next-generation SCs, particularly in flexible and wearable energy storage systems, due to their unique balance of enhanced safety, mechanical stability, wide electrochemical windows, flexibility and stretchability, and device integration potential.[99] However, their major limitations lie in their generally low ionic conductivity at room temperature compared to pure liquid electrolytes, potential drying out or dehydration over time (especially in aqueous gels),

and limited long-term mechanical integrity under extensive cycling or extreme environmental conditions. Compared to the other electrolytes, aqueous electrolytes are widely used in SCs owing to their advantageous properties, such as high ionic conductivity, low cost, simple preparation methods, environmental friendliness, and enhanced safety.[100] Because of higher ionic mobility and lower resistances, aqueous electrolytes are particular attractive for the preparation of SCs with rapid charging-discharging cycles and at high power densities.[101,102] Therefore, aqueous electrolytes are considered to be the ideal choice for the SC construction. However, their electrochemical stability window is limited by the thermodynamic decomposition potential of water (~ 1.23 V).[103] Extending the operational voltage window of aqueous electrolytes is a key factor in the development of high-performance SCs.

To significantly improve the capacitance and energy density of SCs, incorporation of redox-active species in the aqueous electrolytes that can induce reversible redox reactions within the electrolyte has been presented as an effective strategy.[47] These redox-active species participate in fast and reversible electron transfer processes, thereby contributing pseudocapacitance in addition to the double-layer capacitance. The coexistence of these two mechanisms leads to a substantial enhancement in the overall energy storage performance. Moreover, the integration of such redox-active species into the aqueous electrolytes has demonstrated long-term stability, with minimal degradation observed even after thousands of charging-discharging cycles.[48,57]

However, several prerequisites must be met to successfully implement redox-active electrolytes for the achievement of enhanced performance in PCs. An appropriate redox-active electrolyte employed in the design of PCs with high power density and energy density needs to exhibit excellent ionic conductivity, a broad electrochemical stability window, and good solubility in the selected solvent.[48] Importantly, the redox potential of the selected redox-active electrolyte must be compatible with or situated within the electrochemical stability windows of both the solvent and the capacitor electrode materials. In addition, both the electrolyte and the involved oxidation and reduction products during the charging-discharging processes should have good chemical and

electrochemical stability. This implies that the electrolyte must remain chemically and electrochemically inert toward other various SC components, such as electrode materials, solvents, and supporting electrolytes, to avoid undesirable side reactions during operation. The faradaic reactions of the introduced redox-active species are expected to be highly reversible. Minimizing voltage loss during charging and discharging cycles is achievable when the chosen redox-active electrolytes demonstrate fast ion diffusion kinetics and highly efficient electron-transfer kinetics. Furthermore, the selected redox electrolyte should ideally exhibit high availability, environmental compatibility, cost-effectiveness, enhanced safety, and natural abundance.

1.6 Motivation of the thesis

Triggered by the progress and achievements in the fields of SCs (as discussed) and especially with the rapid advancement of wearable and portable electronic devices (e.g., smartwatches, health monitoring sensors, and foldable displays), the development of flexible electrode materials with high energy and power densities, excellent cycling stability, and robust mechanical properties has emerged as a key research objective in the field of energy storage. The primary objective of this thesis thus focuses on the development of high-performance flexible SCs by utilizing appropriate capacitive electrode materials including CC, BDD, and manganese oxides, aiming to address the fundamental limitations of flexible SCs (e.g., their low energy density and performance degradation under mechanical deformation).

CC has been selected as an exemplary flexible substrate owing to its high electrical conductivity, excellent mechanical flexibility, exceptional chemical inertness, and good compatibility with various active electrode materials.[54,104–106] However, CC alone typically exhibits relatively low intrinsic capacitance and energy density, which limits its effectiveness as a standalone electrode material in energy storage. To transcend this limitation and enhance electrochemical performance, this thesis employs a hierarchically engineered electrode architecture that sequentially integrates advanced capacitive

materials onto the surface of CC through optimized deposition techniques (**Figure 1.8**). In short, the **core motivation** of this thesis is to establish a stable electrode architecture that unifies mechanical flexibility with enhanced electrochemical performance. The above challenges are addressed through three interlinked experimental systems:

(1) Diamond cloth: The first electrode system utilizes BDD films deposited on CC. It is named diamond cloth (DC), specifically designed to leverage the advantageous properties of BDD, such as a wide potential window and the exceptional long-term electrochemical stability. To protect the CC substrate from hydrogen plasma etching during the BDD growth process and meanwhile strengthen the adhesion between the substrate and BDD thin films, a titanium (Ti) interlayer is introduced prior to a diamond deposition process. The CFs of the CC substrate have been uniformly coated with high-quality BDD films by optimizing the deposition parameters during MWCVD processes. The electrochemical performance of DC electrodes is evaluated in two types of aqueous electrolytes: 1.0 M Na_2SO_4 solution, and 1.0 M Na_2SO_4 solution + 0.05 M $K_4Fe(CN)_6/K_3Fe(CN)_6$.

(2) $NiMnO_x$-coated CC: The second electrode system integrates redox-active Ni-doped manganese oxides ($NiMnO_x$) film onto CC, aiming to exploit high pseudocapacitances, cost-effectiveness, and environmental friendliness of manganese oxide derivatives. The manganese oxide films have been synthesized using both hydrothermal synthesis and electrodeposition, focusing on film uniformity, synthesis controllability, and electrochemical activity. Their performance has been investigated in 1.0 M Na_2SO_4 aqueous solution.

(3) $NiMnO_x$-coated DC: The third electrode design combines BDD films and $NiMnO_x$ films into a composite structure on CC, intending to integrate the advantages of both electrode materials. The DC electrode constitutes a stable and conductive framework, while $NiMnO_x$ contributes to pseudocapacitive active sites. Such a composite electrode has exhibited enhanced electrochemical performance, including excellent cycling stability, large specific capacitance, high energy density and power density, and good mechanical flexibility.

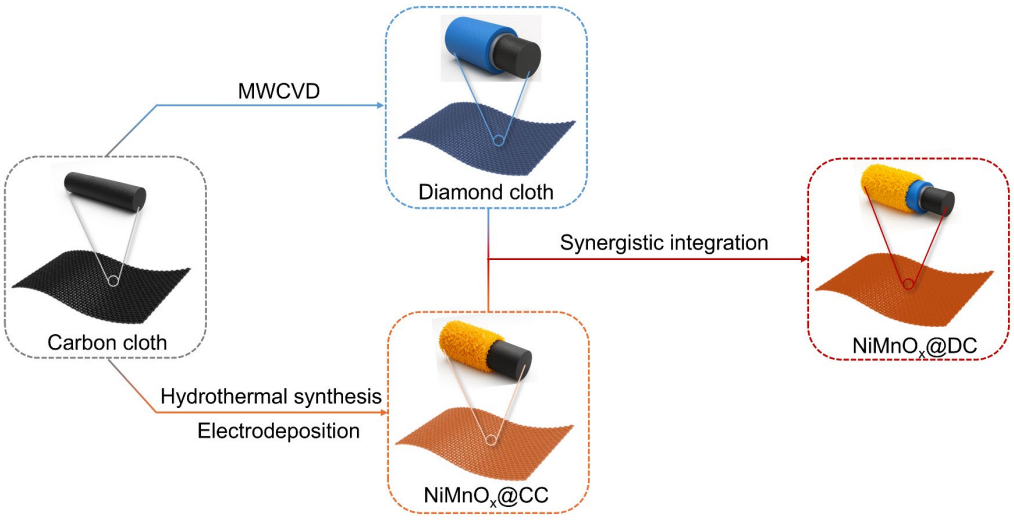


***Figure 1.8**. Schematic illustration of the fabrication pathways for flexible capacitor electrodes: from CC to DC and $NiMnO_x$@CC, and the integration of $NiMnO_x$ with diamond cloth to yield $NiMnO_x$@DC.*

To realize high-performance flexible supercapacitors, the thickness of active films (e.g., BDD and metal oxides) must be carefully regulated to balance ion/electron transport with mechanical flexibility. Two types of configurations are employed to evaluate electrochemical performance. These typically include a three-electrode system, which allows for the detailed analysis of individual electrode materials, and a two-electrode system, which simulates real device operating conditions by assessing the full cell performance. The selection of an appropriate configuration depends on the specific electrochemical characteristics being investigated, such as capacitance, cycling stability, or energy and power density. Furthermore, for evaluation of mechanical flexibility under realistic operating conditions, a gel electrolyte was also designed to enable bending tests of the assembled SCs.

Overall, high-performance flexible SCs are expected to be developed for further applications through a tiered approach: from a highly stable BDD film, to a highly pseudocapacitive manganese oxide layer, and finally to their combination. Through a comparative analysis across DC, $NiMnO_x$@CC, and $NiMnO_x$@DC, meaningful insights

into material design and optimization strategies for flexible SCs can be gained, thereby contributing to the advancement of energy storage technology in the field of wearable and portable electronics.

1.7 Overview of the thesis

This thesis is organized into six chapters that present a systematic electrode engineering approach for high-performance flexible SCs.

The first chapter provides an introduction to the background knowledge of SCs, including the development and their energy storage mechanisms of EDLCs and PCs, their performance metrics, and the electrode materials and electrolytes relevant to this thesis. The chapter concludes by articulating the research motivation and objectives.

Chapter 2 details the experimental methodology, including material synthesis using various methods such as physical vapor deposition (PVD), MWCVD, hydrothermal synthesis, electrodeposition, electrode fabrication, and the characterization techniques employed for morphological, structural, and compositional analysis of investigated materials. Electrochemical techniques (e.g., cyclic voltammetry (CV), galvanostatic charging-discharging (GCD), electrochemical impedance spectroscopy (EIS)) and mechanical flexibility tests are also described. The overall framework spans: (i) synthesis routes, (ii) preparation of flexible DC and $NiMnO_x$-coated electrodes, (iii) comprehensive materials characterization, and (iv) electrochemical measurements.

Chapters 3—5 present results and discussion of a systematic progression in electrode development for high-performance flexible SCs, from flexible DC to the $NiMnO_x$@DC electrode.

Chapter 3 establishes the foundation by developing flexible DC electrodes through comprehensive optimization of BDD film deposition parameters, including Ti interlayer effects, seeding processes, and temperature influences, followed by thorough characterization and comprehensive electrochemical evaluation. The DC electrode

exhibits exceptional cycling stability (e.g., almost 100 % coulombic efficiency and minor capacitance degradation after 10,000 cycles), excellent mechanical flexibility (e.g., 97 % capacitance retention after 500 bending cycles), and a maximum energy density of 45.96 μWh cm^{-2} at a power density of 4.25 mW cm^{-2} for pseudocapacitive configuration with redox electrolytes.

Chapter 4 summarizes the preparation, characterization, and electrochemical evaluation of the $NiMnO_x$@CC electrode material, highlighting the role of Ni–Mn oxides in enhancing energy storage performance and identifying limitations associated with sp^2 carbon substrates. In detail, it demonstrates the advantages of electrodeposition over hydrothermal synthesis. By incorporating a trace amount of nickel component into MnO_x film, the optimized $NiMnO_x$@CC electrode has exhibited high specific capacitances of 47.1 mF cm^{-2} at a scan rate of 10 mV s^{-1}, and 42.8 mF cm^{-2} at a current density of 1 mA cm^{-2} in 1.0 M Na_2SO_4 electrolyte. In addition, this electrode exhibits excellent coulombic efficiency (e.g., over 98.5 % over 10,000 cycles) but suffers from limited cycling stability (in capacitance retention).

Chapter 5 introduces the integrated $NiMnO_x$@DC electrode, which combines the mechanically and electrochemically robust DC electrode support with pseudocapacitive Ni–Mn oxides. The optimized $NiMnO_x$@DC electrode demonstrates pronounced redox features and high specific capacitances of 180.5 mF cm^{-2} at a scan rate of 10 mV s^{-1} and 228.1 mF cm^{-2} at a current density of 2 mA cm^{-2} with exceptional coulombic efficiency approaching 100 % over 10,000 charging-discharging cycles. Regarding capacitance retention, $NiMnO_x$@DC retained 73 % of its initial capacitance after 10,000 cycles, which is markedly higher than the 16 % retention measured for $NiMnO_x$@CC under the same cycling conditions. The symmetric $NiMnO_x$@DC PC deliveres a maximum energy density of 72.8 μWh cm^{-2} at the power density of 5.90 mW cm^{-2} and retained 18.3 μWh cm^{-2} at the power density of 17.0 mW cm^{-2}, indicating a superior balance between energy density and high power delivery. Additionally, the quasi-solid-state flexible $NiMnO_x$@DC PC has exhibited excellent mechanical flexibility (e.g., about 80 % capacitance retention after 500 bending cycles). The electrochemical performance of the

device is well preserved under mechanical stress and dynamic deformation.

Chapter 6 summarizes the main findings from the progressive development of the DC, $NiMnO_x$@CC, and $NiMnO_x$@DC electrodes, providing the key insights into the role of substrate materials in determining the performance and stability of flexible SCs. Furthermore, the chapter concludes with perspectives on potential future research directions to further advance the field of flexible SCs.

2 Experimental

2.1 Material preparation techniques

2.1.1 Radio frequency physical vapor deposition

Radio frequency physical vapor deposition (RF-PVD) is an advanced thin film synthesis technique that has been widely adopted for the fabrication of high-quality, uniform, and adherent thin films. In contrast to conventional sputtering techniques using direct current power, RF-PVD utilizes radio frequency alternating current power to enhance both the efficiency and precision of the thin film deposition onto a substrate.

In this thesis, a home-made RF-PVD reactor was applied to deposit of thin Ti films on the CC substrate. During deposition, the CC substrates were placed into a vacuum chamber maintained at a controlled low-pressure environment (~ 10^{-5} Torr). Pure argon (Ar) gas (purity: 99.999 %) was introduced into the chamber as the sputtering gas. The RF power, operating at the standard frequency of 13.56 MHz, was applied to generate an energetic Ar plasma that bombarded the surface of a Ti target (with a purity of 99.999 %, ZhongNuo Advanced Material Technology Co., Ltd, Beijing, 99.995 % purity, Φ101.6×6 mm), causing Ti atoms to be ejected and transported towards the substrate. These Ti atoms subsequently condensed onto the CC substrate, forming a uniform conformal film. During the deposition process, the temperature of the CC substrates was independently controlled by an additional direct current resistive heating module. This module allowed for precise thermal regulation, ensuring uniform heat distribution across the substrate surface without interfering with the deposition parameters. Deposition parameters, including RF power, Ar gas flow rate, working pressure, substrate-target distance, and deposition duration, were carefully optimized to ensure a continuous and adherent Ti film.

2.1.2 Microwave plasma enhanced chemical vapor deposition

Chemical vapor deposition (CVD) processes can be distinguished by the source of excitation. Among different CVD techniques, the microwave plasma enhanced chemical

vapor deposition (MWCVD) technique stands out as one of the most promising and widely utilized methods that have been widely used to fabricate nanocrystalline diamond thin films. The MWCVD technique utilizes electromagnetic wave energy to activate precursor gases, which typically consist of hydrogen (H_2) carry gas and the precursor of methane (CH_4). The excitation frequency for MWCVD is typically 2.45 GHz. Foremost among its advantages is the capability to generate stable, highly reactive, and uniform plasma environments, enabling precise control over diamond crystallinity, morphology, and doping uniformity. Additionally, diamond films synthesized *via* MWCVD typically exhibit superior chemical purity, excellent adhesion, low residual stress, and high film density. For instance, MWCVD-synthesized diamond films are not subject to contamination resulting from metal filament evaporation, a problem frequently encountered in hot filament chemical vapor deposition (HFCVD).[107] **Figure 2.1** shows a schematic illustration of a typical MWCVD reactor.

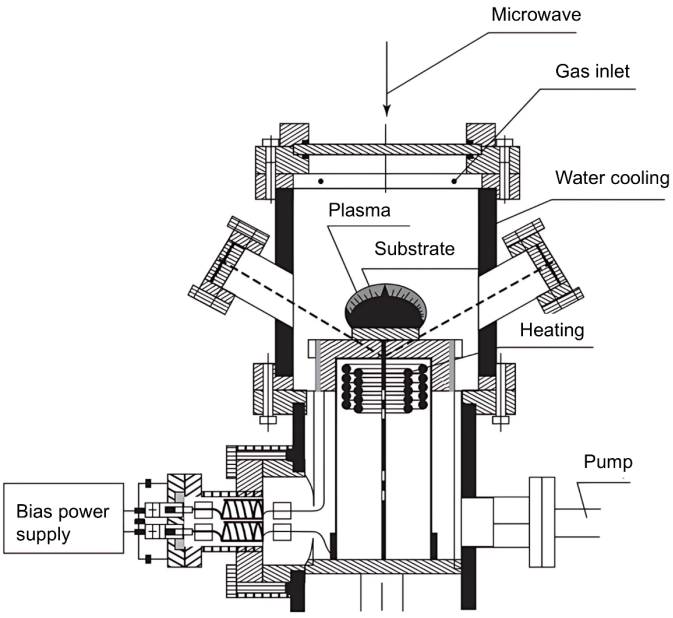


Figure 2.1. *Schematic diagram of an 'ASTeX'-type MWCVD reactor.*[108] *Copyright © 1999 Elsevier Science B.V.*

In this thesis, MWCVD technique was employed to deposit BDD thin films onto CC substrates previously coated with a Ti interlayer deposited through RF-PVD. The precursor gases for deposition of the BDD thin films includes CH_4 (Messer Industriegas,

Germany) as a carbon source and trimethylborane (TMB) gas (diluted in H_2, 1 % in H_2) (Messer Industriegas, Germany) as a boron source. This gas mixture was introduced into the chamber and activated into a luminous plasma ball. Consequently, the substrate was heated by the plasma itself. The temperature of the substrate was influenced by a combination of multiple parameters, such as the microwave power and working pressure.

2.1.3 Hydrothermal synthesis

Hydrothermal synthesis is a widely utilized solution-based chemical process employed to prepare nanostructured materials under controlled temperature and pressure conditions.[109,110] This technique involves chemical reactions occurring in a sealed Teflon-lined autoclave filled with an aqueous solution containing appropriate precursors. Typically, the process is conducted at elevated temperatures ranging from approximately 100 °C to 250 °C, under pressures higher than atmospheric pressure (1 atm), creating thermodynamically favorable environment for crystal nucleation and growth. The hydrothermal method is particularly suitable for the growth of large good-quality crystals while controlling over their composition. In conclusion, hydrothermal synthesis has gained popularity in materials science due to its ability to yield well-crystallized, high-purity, and uniform nanostructured materials with controllable morphologies (e.g., wires/needles, sheets, and hierarchical porous structures). Hydrothermal synthesis of manganese oxides offers several advantages, including simple reaction setup, cost-effectiveness, and environmental friendliness. Moreover, hydrothermal methods allow precise control over reaction parameters such as precursor concentration, solution pH, reaction temperature, duration, and the introduction of dopants.

In this thesis, hydrothermal synthesis was specifically employed to deposit manganese oxides onto flexible CC substrates. A typical hydrothermal synthesis procedure employed in this work involved immersing the CC substrates in a precursor solution containing manganese compounds (e.g., manganese sulfate and potassium permanganate), followed by sealing the mixture within an autoclave. The parameters were precisely controlled, resulting in the formation of uniformly distributed MnO_x nanostructures on CC.

2.1.4 Electrodeposition

Electrodeposition, or electrochemical deposition, refers to a versatile electrochemical process for the preparation of nanostructured thin films or coatings on the surface of conductive materials. Under an applied potential or current, the electrochemical oxidation or reduction of dissolved precursor species occurs. Electrodeposition therefore provides significant advantages, including precise control over film thickness, composition, morphology and uniformity. They can be simply achieved by tuning deposition parameters such as applied voltage, electrolyte composition, and deposition time. Furthermore, electrodeposition is inherently cost-effective, environmentally friendly, and easily adaptable to various substrate geometries. All these advantages make electrodeposition particularly suitable for flexible substrates and substrates with complex structures.

Consequently, electrodeposition was employed specifically to fabricate manganese oxide films and their Ni-doped derivatives onto the substrates in this thesis. Under appropriate electrochemical conditions, dissolved manganese ions undergo oxidation reactions at the electrode-electrolyte interface, resulting in the formation of adherent oxide coatings on the electrode surface. The deposition potential was precisely controlled to optimize the properties of the desired films, thereby enhancing their specific capacitance and cycling stability.

2.2 Electrode materials synthesis

2.2.1 Flexible diamond cloth

The CC (W0S1011, CeTech Co.) was cut into a circular shape with a diameter of 12 mm. Subsequently, it was subjected to ultrasonic cleaning in ethanol for 30 minutes, followed by sequential rinsing with deionized water to remove surface impurities. After drying, the sample was subjected to the PVD chamber for Ti sputtering. Using a Ti metal target with a purity of 99.995 % (Φ101.6×6 mm, ZhongNuo Advanced Material (Beijing)

Technology Co., Ltd), a thin Ti film was sputtered in Ar atmosphere for 1 min. Prior to this sputtering process, the target was subjected to a 10-minute pre-sputtering with a closed shutter to ensure its cleanliness. Detailed sputtering parameters, including background pressure, working pressure, RF power, Ar flow rate, heater power, sputtering time and substrate temperature are listed in **Table 2.1**.

Table 2.1. *Sputtering parameters for RF-PVD fabrication of Ti film*

Sputtering parameter	Value
Background pressure [Torr]	$1.2\sim2.3\times10^{-5}$
Working pressure [Torr]	8.0×10^{-3}
RF power [W]	200
Ar flow rate [sccm]	20
Heater power [V]	50
Sputtering time [min]	1/2/3/10
Substrate temperature [°C]	400

Subsequently, BDD films were grown in a MWCVD reactor (ASTeX 5000W A5000i model). The spontaneous nucleation of diamond on a foreign substrate during a CVD process has a low probability.[111] Prior to this deposition, the sputtered CC was soaked into the ethanol for 45 min and seeded with 1 g L^{-1} nanodiamond water suspension for 90 min in an ultrasonication bath. For control experiments, three distinct substrate temperatures (760 °C, 830 °C, 900 °C) were applied for the growth of BDD thin films. The synthesized DC materials were named DC760, DC830, DC900, respectively. The parameters of these MWCVD processes, including background pressure, working pressure, H_2/CH_4/TMB flow rate, microwave power, deposition time, and substrate temperature, are presented in **Table 2.2**. In the final step, the as-synthesized DC was subjected to heating at 450 °C in air for 2 h with an aim to reduce the sp^2 carbon content on the DC surface and meanwhile to facilitate the introduction of oxygen-containing

functional groups, thereby enhancing hydrophilicity.[112]

***Table 2.2**. Growth parameters of three diamond samples: DC760, DC830, DC900*

Deposition parameter	DC760	DC830	DC900
Background pressure [Torr]	$1.0\sim4.0\times10^{-2}$	$1.0\sim4.0\times10^{-2}$	$1.0\sim4.0\times10^{-2}$
Platform height [mm]	54.7	58	58
H_2 flow rate [sccm]	400	400	400
CH_4 flow rate [sccm]	4.0	4.0	4.0
TMB flow rate [sccm]	5.0	5.0	5.0
Working pressure [Torr]	30	30	35
Microwave power [W]	1000	1000	1100
Deposition time [h]	6	6	6
Substrate temperature [°C]	**760**	**830**	**900**

2.2.2 $NiMnO_x$-coated carbon cloth

Prior to synthesis, the CC substrates were cut and cleaned using the aforementioned preparation method. Following drying, the CC substrate was coated with MnO_x or $NiMnO_x$ through the subsequent procedures.

Hydrothermal method: Potassium permanganate ($KMnO_4$, ≥ 99.0 %, Fluka Chemie GmbH) and manganese (II) sulfate monohydrate ($MnSO_4 \cdot H_2O$, ≥ 97 %, Alfa-Aesar GmbH & Co KG) were used as precursors. In the first step, 45 mL of the aqueous precursor solutions (**Table 2.3**) along with the CC substrates were transferred into a Teflon-lined stainless steel autoclave, which was then placed in a temperature-controlled hydrothermal oven (VWR International, DRY-Line 112 Prime, USA) to conduct related reactions. Upon completion of each reaction, the autoclaves were naturally cooled to room temperature. The synthesized samples were thoroughly rinsed with deionized water

to remove residual ions or loosely bound particles and then dried under ambient conditions.

Five sets of experimental conditions used for hydrothermal synthesis are summarized (**Table 2.3**).

(1) The first synthesis process involved immersing CC in a solution containing 20 mM $KMnO_4$. The reaction was conducted hydrothermally at 150 °C for 5 hours.

(2) Based on the results of the first synthesis, the second synthesis was carried out in 10 mM $KMnO_4$ aqueous solution.

(3) For the third synthesis, a milder condition was applied. The applied $KMnO_4$ concentration was 5 mM, and the reaction temperature was declined to 80 °C. The hydrothermal reaction time was 1 h.

(4) The fourth synthesis was similar to the second one, utilizing the same precursor solution (5 mM $KMnO_4$), except the hydrothermal reaction duration at 80 °C was extended to 2h.

(5) In the fifth experiment, a mixed precursor solution consisting of 42 mM $KMnO_4$ and 16.7 mM $MnSO_4$ was utilized. The reaction was conducted at 150 °C for 5 h.

The as-prepared samples were designated as SH-1, SH-2, SH-3, SH-4, and SH-5, respectively (where S refers to sample, and H to hydrothermal).

The formation of MnO_x *via* a hydrothermal synthesis process can typically involve the following redox reaction:

$$4MnO_4^- + 3C + H_2O \rightarrow 4MnO_2 + CO_3^{2-} + 2HCO_3^-$$

For the condition with $MnSO_4$, a redox reaction between permanganate and manganese ions can be primarily involved as well:

$$2MnO_4^- + 3Mn^{2+} + 2H_2O \rightarrow 5MnO_2 + 4H^+$$

Note that the reactions involved in the formation of manganese oxides are indeed highly complex. Consequently, the synthesized manganese oxide products may contain various

oxidation states of manganese. For instance, both Mn_2O_3 and MnO_2 could be formed during hydrothermal synthesis. For simplicity, the products are collectively referred to as MnO_x in this thesis.

***Table 2.3**. Summary of experimental parameters for different synthesis*

Method	Sample number	Precursors	Conditions
Hydrothermal synthesis	SH-1	20 mM $KMnO_4$	150 ℃ / 5 h
	SH-2	10 mM $KMnO_4$	150 ℃ / 5 h
	SH-3	5 mM $KMnO_4$	80 ℃ / 1 h
	SH-4	5 mM $KMnO_4$	80 ℃ / 2 h
	SH-5	42 mM $KMnO_4$ + 16.7 mM $MnSO_4$	150 ℃ / 5 h
Electrodeposition	SE-Mn	50 mM $MnSO_4$	0.9 V (*vs.* Ag/AgCl) 1500 s
	SE-Ni	3 mM $Ni(CH_3COO)_2$	
	SE-NiMn	50 mM $MnSO_4$ + 3 mM $Ni(CH_3COO)_2$	

Electrodeposition: Electrochemical deposition of manganese oxides films onto CC substrates was conducted using an amperometric *i-t* (i.e., current-time) technique. Electrodeposition was performed using a CHI660E Potentiostat/Galvanostat (Shanghai Chenhua Inc., China). A standard three-electrode configuration was employed, with the CC substrate serving as the working electrode, a platinum (Pt) sheet acting as the counter electrode, and an Ag/AgCl (3 M KCl) (CHI111Shanghai Chenhua Inc., China) electrode used as the reference electrode. For such electrodeposition, three different aqueous electrolytes were prepared (**Table 2.3**): (i) 50 mM $MnSO_4$, (ii) 3 mM nickel (II) acetate

tetrahydrate ($Ni(CH_3COO)_2 \cdot 4H_2O$, ≥ 99 %, ChemPur Feinchemikalien und Forschungsbedarf GmbH), and (iii) a mixed electrolyte containing 50 mM $MnSO_4$ and 3 mM $Ni(CH_3COO)_2$. All the volumes of the used electrolytes were about 40 mL. The deposition was carried out at a constant applied potential of 0.9 V *vs.* Ag/AgCl for a total duration of 1500 s at room temperature. After the deposition, the synthesized electrodes were thoroughly rinsed with deionized water in order to remove any loosely adhered particles and residual electrolyte and finally dried under ambient conditions.

During the electrodeposition process, the following reactions occur:

$$Mn^{2+} + (1+n)H_2O \rightarrow MnO_{(1+n)} + (2+2n)H^+ + 2ne^-$$

The value of *n* can be either 1 or 1/2. Therefore, similar to the hydrothermally synthesized products, the manganese oxides might contain both Mn(III) and Mn(IV).

$$Ni^{2+} + 2H_2O \rightarrow NiOOH + 3H^+ + e^-$$

The as-prepared samples were designated as SE-Mn, SE-Ni, and SE-NiMn, respectively (where S refers to sample, and E to electrodeposition).

2.2.3 $NiMnO_x$-coated diamond cloth

In the mixture of 50 mM $MnSO_4$ and 3 mM $Ni(CH_3COO)_2$ with a volume ratio of 1:1, electrochemical deposition of $NiMnO_x$ films onto the BDD films-coated CC (i.e., DC) was conducted, according to the procedures described in Section 2.2.1. The electrodeposition procedure followed a similar protocol to that employed for the CC substrates (Section 2.2.2). A CHI Chenhua electrochemical workstation was employed using a three-electrode configuration with the DC as the working electrode. The DC working electrode, reference electrode of Ag/AgCl, and Pt counter electrode were immersed in 40 mL of the electrolyte mixture. To investigate the effect of applied potential on deposition behavior and resulting film properties, three deposition voltages were applied: 0.9 V, 1.0 V, and 1.1 V (*vs.* Ag/AgCl). The deposition time was kept constant at 1500 s at room temperature. After the deposition, the $NiMnO_x$-coated DC electrodes were thoroughly rinsed and dried following the procedure described in the previous

sections. The resulting samples were denoted $NiMnO_x$@DC-0.9, $NiMnO_x$@DC-1.0, and $NiMnO_x$@DC-1.1.

2.3 Characterization

2.3.1 Morphology and structural characterization

The surface and cross-sectional morphologies of the electrode materials in this thesis were investigated using field-enhanced scanning electron microscopy (FESEM, Zeiss Ultra55, Germany). In-lens secondary electron images were recorded under a high vacuum condition. The electron source was generated using a field emission gun and subsequently accelerated, with the acceleration voltage adjusted within the range of 3 to 10 kV.

The microstructural analysis of DC electrode was carried out using a high-resolution transmission electron microscopy (HRTEM, ThermoFisher, Talos F200X, USA). The instrument was operated at an accelerating voltage of 200 kV, which is a standard setting for achieving atomic-level resolution and obtaining detailed information about crystal lattice structures.

The specific surface areas of these electrodes were determined using the nitrogen adsorption technique, which is a widely employed method for characterizing porous materials. Brunauer-Emmett-Teller (BET) method, which is based on the physical adsorption of gas molecules onto a solid surface, has been applied for surface area analysis.

2.3.2 Phase and component analysis

An energy-dispersive X-ray spectrometer (EDX, Thermo Fisher Scientific, USA) integrated with a FESEM was employed to analyze the elemental composition of the synthesized films. A high-energy electron beam is necessary to induce the emission of characteristic X-rays from the sample material. Different operational modes of EDX analysis were utilized, including point-shoot mode, line-scan mode, and element mapping

mode.

The X-ray photoelectron spectroscopy (XPS) measurements (Surface Science Instruments, S-probe photoelectron spectrometer SSX-100, USA) were carried out to analyze the chemical states of the synthesized films, with Al Kα radiation at a power setting of 200 W. By irradiating the surface with a beam of X-rays and simultaneously measuring the kinetic energy of the electrons emitted from within 1-10 nm of the surface of the synthesized materials being analyzed, an XPS spectrum was obtained. The XPS spectra analysis was carried out using CasaXPS processing software (Version 2.3.19PR 1.0). The XPS spectra were calibrated with the C–C peak at 284.8 eV serving as the binding energy (BE) reference.

Raman spectra of the synthesized samples were collected using a micro-Raman spectrometer (Thermo Fisher Scientific, Nicolet Almega XR, USA) operating at a fixed laser excitation wavelength of 532 nm (frequency-doubled neodymium-doped yttrium orthvanate diode-pumped solid-state laser, power of 25 mW). The molecular structure, composition and crystallinity of the material were analyzed by Raman spectroscopy.

The crystalline structure and phase composition of the materials were systematically investigated through X-ray diffraction (XRD) analysis using an advanced diffractometer (PANalytical, Netherlands). The XRD measurements were performed employing monochromatic Cu Kα radiation (λ = 1.54 Å) as the incident X-ray source. The X-ray tube was operated under conditions of 40 kV voltage and 40 mA current. The resulting diffraction patterns were subsequently analyzed to determine the phase composition, crystallinity, and structural characteristics.

2.4 Electrochemical measurements

Electrochemical performance of the synthesized electrodes was evaluated through cyclic voltammetry (CV), galvanostatic charging-discharging (GCD) technique, and electrochemical impedance spectroscopy (EIS) that are available on electrochemical

workstations (CHI660e, Shanghai Chenhua Inc., China, and PMC-1000, Ametek Scientific Instruments, USA). Both three-electrode and two-electrode systems were employed. In a three-electrode configuration, the synthesized electrode served as the working electrode, an Ag/AgCl (3.0 M KCl) electrode functioned as the reference electrode, and a Pt sheet was used as the counter electrode. In a two-electrode configuration, two electrode materials acted as the capacitor electrodes. To investigate the electrochemical performance of the synthesized electrode materials, different electrolytes were employed, including a 1.0 M Na_2SO_4 (≥ 99 %, Carl Roth GmbH + Co. KG) aqueous solution, a 1.0 M Na_2SO_4 solution supplemented with 0.05 M $K_3Fe(CN)_6/K_4Fe(CN)_6$ (≥ 99.0 %/≥ 98 %, Alfa Aesar GmbH & Co KG) redox species.

2.4.1 Cyclic voltammetry

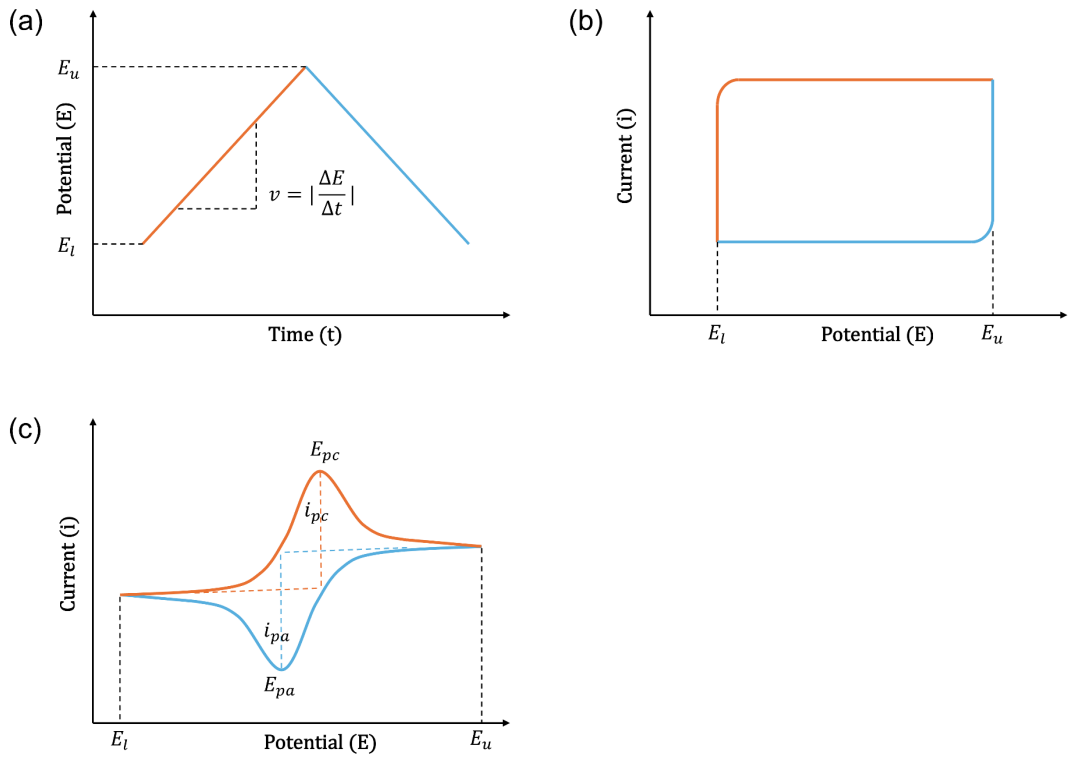


***Figure 2.2**. (a) Triangular wave potential as a function of time applied for CV measurements. (b) An idealized cyclic voltammogram illustrating the electrochemical behavior of an EDLC. (c) A representative cyclic voltammogram exhibiting distinct redox peaks with anodic and cathodic currents.*

CV is a well-established electrochemical characterization technique, extensively employed to investigate the redox behavior and electrochemical properties of materials. The technique involves applying a linearly varying potential (or voltage for two-electrode configuration) to a working electrode immersed in an electrolyte solution, while simultaneously monitoring the resulting current response. The potential is cycled between predefined lower (E_l, V) and upper (E_u, V) limits at a constant scan rate (v, mV s^{-1}), as shown in **Figure 2.2a**. The characteristics current-potential plots recorded are referred to as cyclic voltammograms. From these curves, essential electrochemical parameters such as current densities, oxidation and reduction potentials, redox reaction reversibility, and capacitance can be derived.

Corresponding to the two distinct energy storage mechanisms of SCs, two typical cyclic voltammograms can be observed. An EDLC stores charges *via* electrostatic accumulation of ions at the electrode-electrolyte interface, without faradaic reactions. Consequently, its CVs are characterized by a nearly rectangular-shaped profile (**Figure 2.2b**), demonstrating ideal capacitive behavior. The symmetry and rectangularity indicate efficient and reverse ion adsorption/desorption and rapid charge transfer, which are characteristic features of an EDLC. In contrast, as illustrated in **Figure 2.2c**, the representative cyclic voltammogram of a PC exhibits clear oxidation and reduction peaks. These peaks correspond to specific redox reactions occurring at the electrode-electrolyte interface, indicating that the charge storage mechanism involves electron transfer accompanied by (quasi) reversible redox reactions. Anodic peak current (i_{pa}) and cathodic peak current (i_{pc}) correspond to the oxidation reaction and reduction reaction, respectively. The comparison of their absolute values, together with the separation between anodic peak potential (E_{pa}) and cathodic peak potential (E_{pc}), are often used to determine the electrochemical reversibility of the redox reaction. For an ideal CV of a PC, the peak current ratio should be near unity, and the value of peak potential separation should be approximately $59/n$ mV, where n refers to the stoichiometric number of transferred electrons.[113,114]

The areal specific capacitance ($C_{s,CV}$, mF cm^{-2}) can be calculated through the following

equation:

$$C_{s,CV} = \frac{\int I(V)dV}{2 \times v \times \Delta V \times A} \quad (2.1)$$

Where I refers to the response current, V is the applied potential, v is the scan rate, ΔV is the potential change, and A is the geometric area of the effective capacitor electrode.

2.4.2 Galvanostatic charging-discharging technique

The GCD technique is a characterization method typically used to evaluate the performance of SCs. This method applies a constant current to an electrode or a device and simultaneously monitors the potential (or voltage in a two-electrode configuration) response as a function of time during both the charging and discharging processes. In a typical GCD measurement, the working electrode or device is initially charged by applying a constant current until reaching a pre-set upper potential limit (E_u), followed immediately by discharging at the same current down to a predetermined lower potential limit (E_l). The resultant potential-time profiles (i.e., GCD curves) provide critical insights into the electrochemical performance of the electrode material, such as capacitance, coulombic efficiency, and reversibility.

Depending on the energy storage mechanism, the GCD curves can exhibit distinct shapes. For an EDLC, the GCD curve (as shown in **Figure 2.3a**) is ideally triangular, indicating linear charging-discharging behavior resulting from the pure electrostatic adsorption and desorption of ions. In contrast, pseudocapacitive electrodes often show plateaus in their GCD curves (as shown in **Figure 2.3b**), reflecting redox reactions with phase transformations or intercalation processes. These plateaus correspond to constant potential regions where faradaic processes dominate. The symmetry of these two curves reflects the reversibility of the charging and discharging processes.

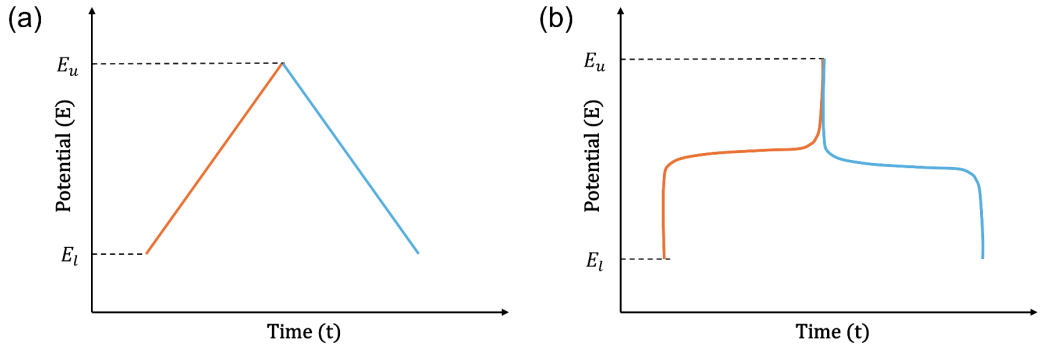


***Figure 2.3**. Two typical GCD curves of SCs: (a) the representative GCD curve of an ideal EDLC, and (b) the typical GCD curve for a PC.*

The area-normalized capacitance ($C_{s,GCD}$, mF cm^{-2}) can be quantitatively calculated from the GCD curves using the following equation:

$$C_{s,GCD} = \frac{I \times \Delta t}{2 \times \Delta V \times A} \tag{2.2}$$

where I refers to the value of the applied constant current, Δt is the charging and discharging time, ΔV is the potential change, and A is the geometric area of the effective capacitor electrode.

In addition, the cycling stability of the capacitor electrodes or devices in this thesis was examined through the GCD technique. During the cycling test, the electrode or device was subjected to repeated charging and discharging cycles under constant current conditions, typically over thousands of cycles. Afterwards, the capacitance retention was calculated. These results provide valuable insights into the reliability and potential for practical implementation of the electrode materials.

2.4.3 Electrochemical impedance spectroscopy

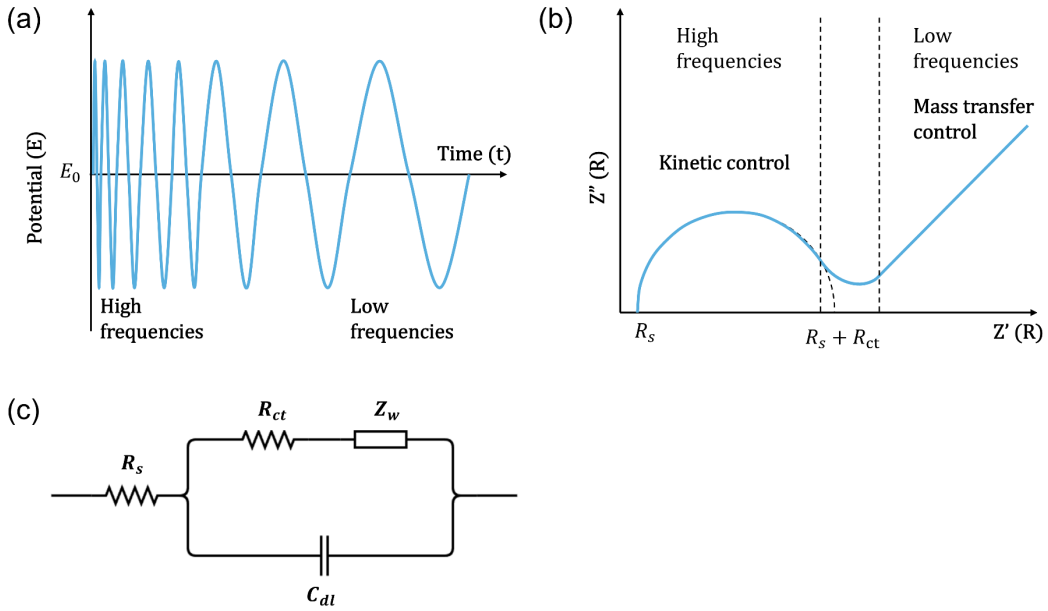


***Figure 2.4**. (a) A periodic sinusoidal potential perturbation with constant amplitude across a range of frequencies from high to low in EIS. (b) Schematic of a typical Nyquist plot. (c) The Randles equivalent electrical circuit.*

EIS is a powerful analytical technique widely employed to characterize the interface features between electrode and electrolyte, providing valuable insights into the internal resistances of energy storage devices and electrode materials. By applying small-amplitude sinusoidal potential perturbation (**Figure 2.4a**) across a wide frequency range (typically from 100 kHz to 0.01 Hz) and subsequently measuring the corresponding current response, EIS quantifies the complex impedance (Z) as a function of frequency. The results in this thesis were presented as Nyquist plots (**Figure 2.4b**), which display the real part (Z') versus the imaginary part (Z'') of the complex impedance.[115] The semicircular region at high frequencies reflects the charge transfer process, controlled by the charge transfer resistance (R_{ct}) and double-layer capacitance (C_{dl}). The intercept at high frequencies on the real axis represents the electrolyte resistance (R_s). At low frequencies, the straight line inclined at approximately 45° indicates the Warburg

impedance (Z_w), which is related to ion diffusion and mass transport limitations.[115–118] The plot is commonly divided into regions dominated by kinetic control (high frequencies) and mass transfer control (low frequencies). The equivalent circuit (**Figure 2.4c**) represents a typical model used to fit EIS data. In the thesis, the data were processed and fitted through ZView software (Version 2.1c).

2.4.4 Mechanical flexibility

A gel electrolyte was prepared and subsequently subjected to bending tests for the evaluation of the mechanical flexibility of SCs. In a beaker, 2 g of acrylamide (≥ 98.5 %, Thermo scientific) was added to 20 mL of deionized water and stirred until complete dissolution was achieved. The resultant solution was then mixed with 20 mL of 0.5 M Na_2SO_4 aqueous solution. Consequently, 0.5 g of ammonium persulfate (APS, ≥ 98.0 %, Merck) as an initiator was added to the mixture and mixed until it dissolved completely to obtain a transparent and homogeneous solution. The beaker was sealed and transferred into a drying oven set at 50 °C. The mixture was heated at 50 °C for 12 h to form a gel electrolyte. In the assembly step, a thin gel electrolyte was cut and placed between two capacitor electrodes, which were connected to thin copper (Cu) sheets. Subsequently, the assembly was covered with two plastic sheets, thereby sealing the SC. **Figure 2.5** illustrates the assembly configuration. The assembled SC was investigated by electrochemical measurements under different bending conditions.

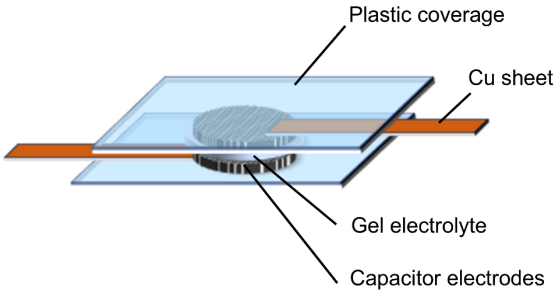


***Figure 2.5**. Schematic configuration of a SC using a gel electrolyte for bending tests.*

3 Flexible Diamond Cloth electrode

The growing demand for wearable and portable electronics motivates electrode architectures that combine rapid charge transfer, high electrochemical stability, and reliable performance under mechanical deformation. The development of flexible SC electrodes requires materials that can simultaneously deliver high electrochemical performance and withstand mechanical deformation without significant degradation. CC has been widely used as an ideal current collector or electrode substrate in flexible SCs owing to its lightweight nature, good electrical conductivity, high flexibility, and 3D architecture.[53,54] Nevertheless, its intrinsic capacitance is too low to enable direct use as an active electrode material. To address this limitation, the integration of capacitive materials onto CC has proven to be an effective strategy for enhancing the specific capacitance and energy density of CC-based flexible SCs.[53]

Conductive diamond nanomaterials exhibit excellent electrochemical performance, making them promising candidates for capacitor electrodes.[11,60] In particular, BDD has attracted attention owing to its significant advantages, including good conductivity, a wide potential window, low background current, excellent chemical stability, and reliable electrochemical response to redox systems.[61,119] In this chapter, a flexible DC was synthesized by overgrowing a thin BDD film on CC substrate *via* MWCVD. DC represents a strategic integration of two complementary materials: the mechanical flexibility and 3D architecture of CC with the exceptional electrochemical properties of BDD films. Prior to deposition of BDD film, a thin Ti interlayer was sputtered onto CC substrate using RF-PVD to protect it from plasma-induced etching and enhance interfacial adhesion. This chapter systematically investigates the optimization of DC fabrication parameters, including the critical role of protective interlayers, seeding processes, and deposition conditions in achieving uniform diamond films. Comprehensive characterization (morphology, structure, and composition) is followed by electrochemical evaluation using both three-electrode and two-electrode configurations, encompassing rate capability, impedance, energy and power densities, and cycling stability. Both EDLCs and PCs using DC electrodes are evaluated. Finally, mechanical

flexibility is assessed under different bending conditions. The insights gained from DC electrode development provide the foundation for subsequent integration with pseudocapacitive materials in later chapters.

3.1 Optimization of BDD film deposition

The preparation process of flexible DC is schematically illustrated in **Figure 3.1**. Generally, the fabrication process consists of two primary stages. In the first step, a Ti interlayer is deposited onto the surface of the CC substrate using an RF-PVD technique. Subsequently, BDD thin films are grown over the Ti interlayer-covered CC inside a MWCVD reactor.

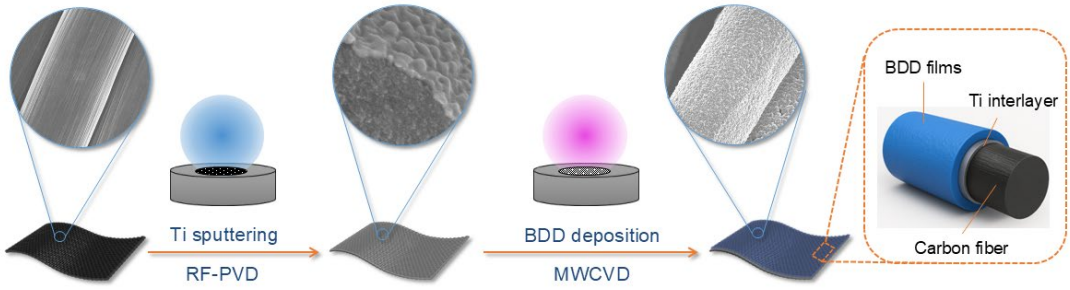


***Figure 3.1**. Diagram illustrating the preparation processes of DC electrode materials. The insets display FESEM images of the samples captured at various stages of the preparation process.*

3.1.1 Influence of the titanium interlayer

Before the overgrowth of BDD films using MWCVD, a Ti thin film was sputtered onto the CC surface as a protective and adhesion-enhancing interlayer using an RF-PVD technique. The FESEM images in **Figure 3.2** demonstrate the critical influence of a Ti interlayer in the synthesis of DC electrodes. Without the Ti interlayer, significant damages to the CF surface are observed due to direct plasma exposure (**Figure 3.2a**). The CC fibers

are intensively etched by the hydrogen plasma generated during the MWCVD process. In contrast, the quality of the as-synthesized BDD films is significantly improved with the protection of a moderate Ti interlayer (**Figure 3.2b**). The CFs maintain their smooth morphology while being uniformly coated with a dense and continuous diamond film. However, an excessively thick Ti interlayer (e.g., over 100 nm after a 10-minute sputtering time) adversely affects the integrity of BDD films. **Figure 3.2c** reveals delamination and cracking of the diamond film, indicating internal stress accumulation and poor adhesion between the BDD films and the CC fibers. This suggests that over-deposition of the Ti interlayer introduces additional residual stress, thereby compromising its effectiveness as a transition layer. Actually, all Ti interlayers deposited with sputtering times ranging from 1 to 3 minutes contribute to the protection of CFs and enhance the adhesion between BDD films and the CC substrate. To ensure the preservation of superior flexibility in the electrode material, CC coated with a Ti thin film deposited *via* 1-minute sputtering was employed as the substrate for the subsequent growth of the BDD films.

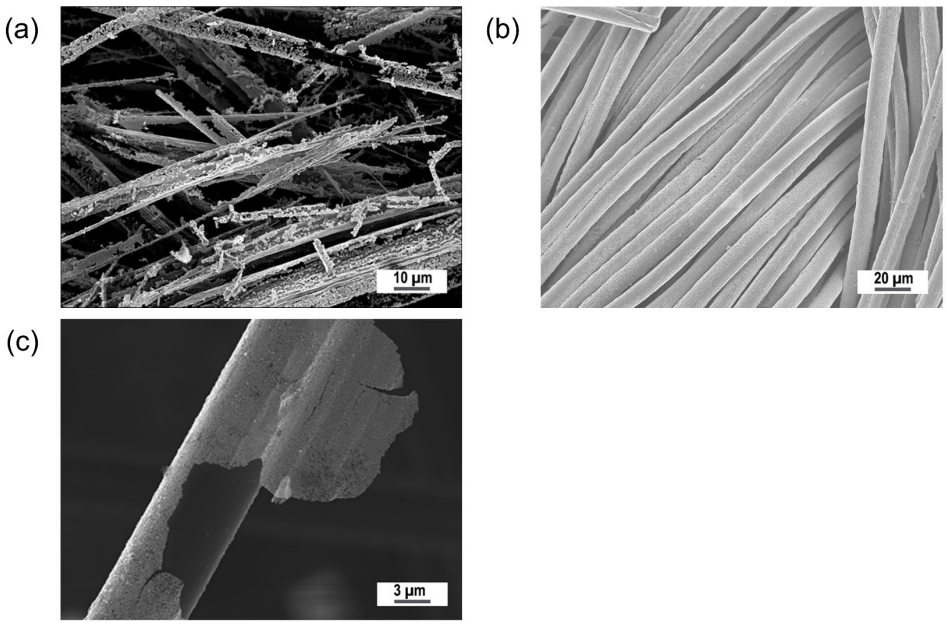


***Figure 3.2**. FESEM images of (a) a BDD film directly overgrown on CC, (b) BDD films-covered CC with a Ti interlayer via 1 min sputtering, (c) BDD films-covered CC with a Ti interlayer via 10 min sputtering.*

3.1.2 Seeding process

The seeding process plays a crucial role, as it determines the nucleation density and growth uniformity of the BDD film through the MWCVD technique. However, the presence of a Ti interlayer has a noticeable influence on seeding efficiency by altering the surface energy and surface chemistry. To investigate the effect of different seeding conditions, three treatments were applied to CC sputtered with a 1-minute Ti interlayer: (a) ultrasonication in a 1.0 g L^{-1} nanodiamond (ND) water suspension for 90 minutes; (b) ultrasonication in a 1.0 g L^{-1} ND methanol suspension for 90 minutes; (c) soaking in ethanol for 45 minutes followed by ultrasonication in a 1.0 g L^{-1} ND water suspension for 90 minutes.

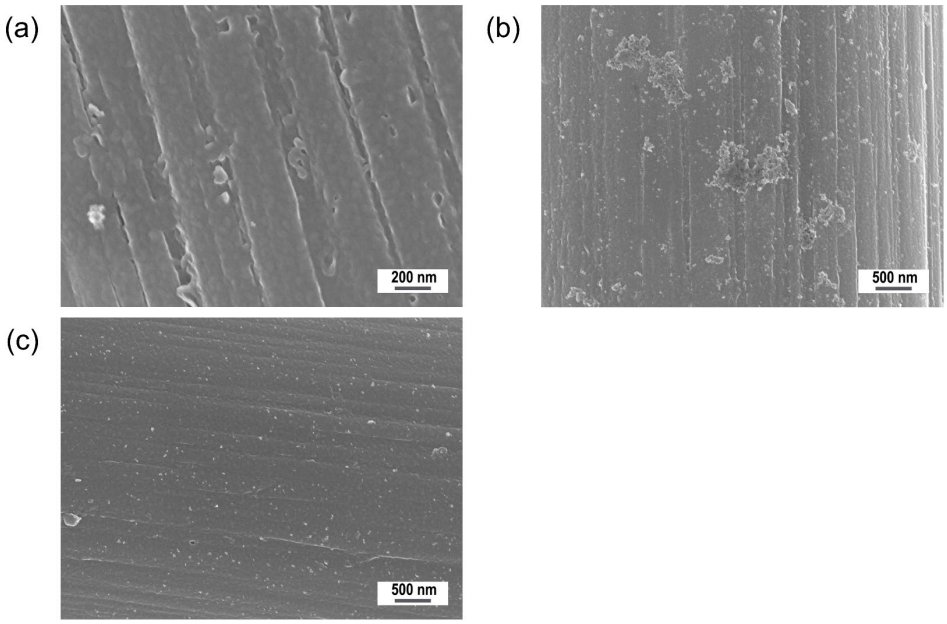


***Figure 3.3**. FESEM images of Ti interlayer-covered CC after seeding treatment with (a) 1.0 g L^{-1} ND water suspension, (b) 1.0 g L^{-1} ND methanol suspension, and (c) ethanol plus followed 1.0 g L^{-1} ND water suspension.*

The corresponding FESEM images (**Figure 3.3**) exhibit the distinct seeding distribution resulting from three treatments. **Figure 3.3a** reveals that almost no ND particles are attached to the substrate surface. This can be attributed to the high surface

tension and poor wettability of the Ti layer, thereby hindering the adsorption of ND particles in aqueous suspension. In contrast, the seeding treatment with methanol suspension results in a substantial amount of ND particles adhering to the surface (**Figure 3.3b**). The lower surface tension and better wetting properties towards methanol facilitate more uniform dispersion and stronger interaction between the ND seeds and the Ti surface. However, significant particle agglomeration is observed, indicating that the particles tended to cluster in this procedure, which can result in non-uniform nucleation sites during subsequent film growth. For third seeding condition, the combined ethanol soaking and subsequent ND seeding in water suspension yields a more uniform and well-dispersed distribution of ND particles on the surface (**Figure 3.3c**). The initial soaking in ethanol increased surface wettability, thereby promoting better attachment and dispersion of the ND particles in the subsequent aqueous suspension step. This dual-step approach effectively mitigates seed agglomeration and enhances the homogeneity of the seed distribution.

3.1.3 Influence of deposition temperature

The substrate temperature plays a critical role in the MWCVD synthesis of BDD films.[120] By adjusting the working distance and working pressure, the substrate temperature was controlled at 760 °C (DC760), 830 °C (DC830), or 900 °C (DC900). From their FESEM images (**Figure 3.4**), one can see that carbon fibers cannot be completely covered by diamond grains at both excessively high and low substrate temperatures. As observed in **Figure 3.4a**, at the relatively lower substrate temperature of 760 °C, the deposited BDD film exhibited incomplete surface coverage with evident gaps and discontinuous grain boundaries. The insufficient deposition rate due to the relatively larger working distance limits to achieving high-quality BDD films. When the substrate temperature was increased to 830 °C (**Figure 3.4b**), the diamond grains became more uniform and densely packed, forming a continuous and well-faceted film. This indicates that an optimal substrate temperature enhances the surface migration of carbon species, facilitating more efficient growth and improving the film quality. At an even higher substrate temperature of 900 °C (**Figure 3.4c**), the film surface shows overgrowth

with larger, coarsened grains and increased surface roughness. The higher temperature enables to improve the growth rate of crystal grains, resulting in uneven grain development, where larger grains dominate at the expense of smaller ones. This competitive growth behavior leads to non-uniform surface coverage and negatively impact the film integrity.

In summary, the substrate temperature of approximately 830 ℃ was determined to be optimal for fabrication of DC electrode materials. Unless otherwise specified in the following sections, DC material specifically refers to the DC prepared at approximately this optimal temperature.

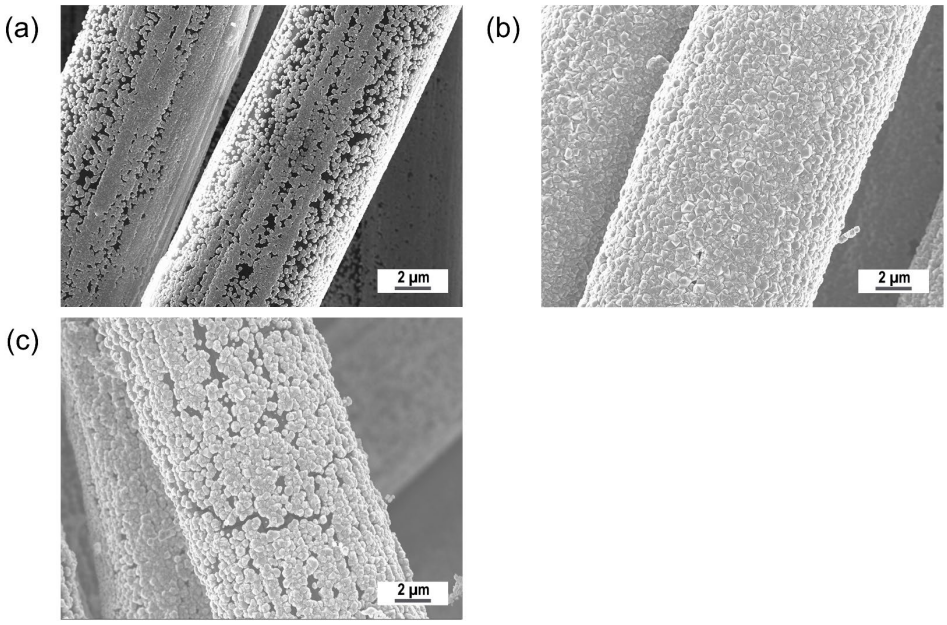
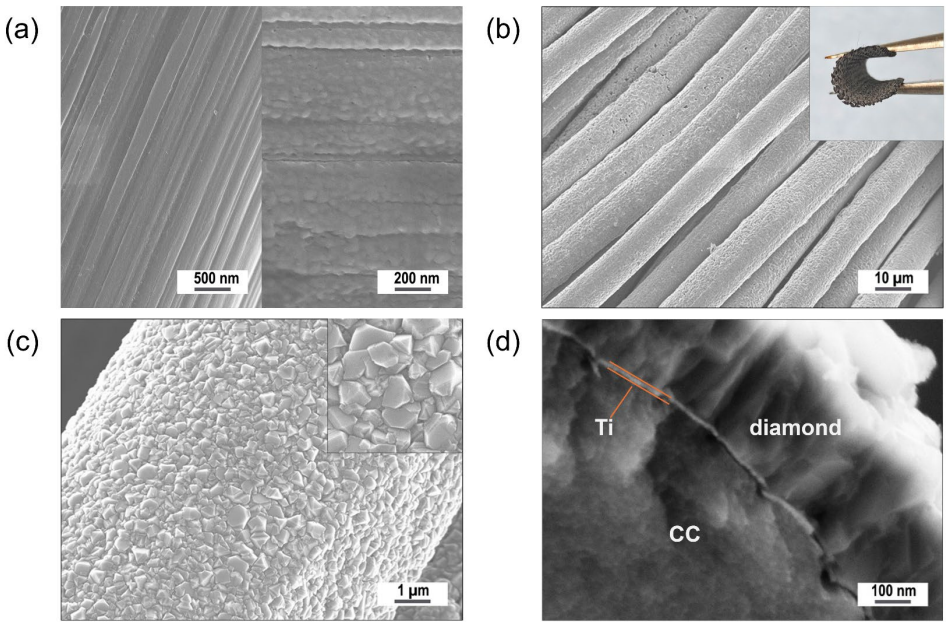


***Figure 3.4**. FESEM images of three samples: (a) DC760, (b) DC830, and (c) DC900.*

3.2 Characterization of diamond cloth

The surface morphology of the fabricated DC was first characterized through FESEM. The CC fibers maintain a high degree of uniformity in diameter (**Figure 3.5b**) and are fully covered by tightly packed BDD films (**Figure 3.5c**). The dense and crystalline surface offers superior mechanical strength and chemical stability. In electrochemical applications, this structure can significantly enhance electron transfer rates, improve

corrosion resistance, and increase the effective surface area for redox reactions. From the cross-sectional image of the CC fibers covered with BDD films (**Figure 3.5c**), the thickness of this interlayer is around 20—30 nm. In comparison with the pristine CC surface, it was evident that a uniform thin layer of Ti had been coated on the surface (**Figure 3.5a**). Nevertheless, it does impede the etching process of CFs and enhance the adherence of the BDD films to the substrate. With a deposition time of 6 h at the substrate temperature of 830 °C, the thickness of a BDD film reaches about 200—300 nm (**Figure 3.5d**). For such DC material, the CC is the core working as the skeleton and the BDD film is the shell covering the carbon fibers. The film per se consists of uniform diamond grains. According to statistics (through Nano Measurer, Version 1.2.5), the grain size is distributed mostly within the range of 200 to 400 nm, with an average size of 316 nm (**Figure 3.5e**). The carbon fibers of commercial CC have a very smooth surface and a limited specific surface area (1 m^2 g^{-1}) (**Figure 3.5a**).[56] In contrast, DC material has an increased specific surface area (18.6 m^2 g^{-1}), as determined from the gas adsorption-desorption isotherms (**Figure 3.5f**). The structure of this DC material provides a robust structural foundation for its use as an electrode to exert the excellent characteristics of diamond and CC.



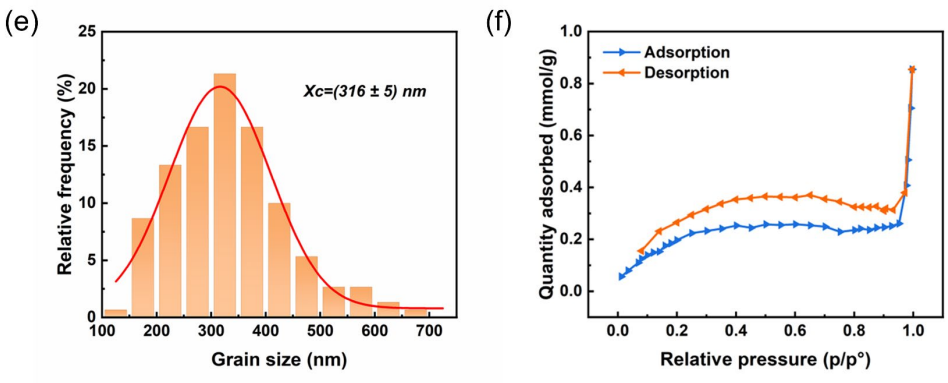


***Figure 3.5**. FESEM images of (a) CC surface before (left) and after (right) Ti sputtering. (b)-(d) FESEM images of DC material at different resolutions; The inset in (b) is the picture of a bending DC sheet; The inset in (c) shows the details of the diamond crystal grains; (d) the cross-sectional FESEM image. (e) The size distribution of diamond grains. (f) Nitrogen adsorption-desorption isotherms.*

HRTEM investigation and EDX elemental mapping were employed to get a deep insight into the microstructures of DC materials. The cross-sections of DC were firstly characterized. As shown in **Figure 3.6a**, a well-transited layered structure is observed, comprising a top BDD film and an underlying Ti interlayer. HRTEM image of the BDD region (**Figure 3.6b**) reveals a lattice spacing of 0.21 nm, corresponding to the (111) plane of crystalline diamond, confirming the high crystallinity of the deposited film.[121,122] The fast Fourier Transform (FFT) pattern (**Figure 3.6c**) further provides valuable insights into the crystalline orientations of this diamond phase. The clear and distinct spots in the FFT pattern suggest that the diamond sample has high crystallinity with minimal disorder. The (111) plane, which is prominently visible in the FFT pattern, corresponds to one of the most stable and common crystallographic planes in the diamond structure. Additionally, other prominent spots such as the (220) plane are observed in the FFT pattern. These spots confirm the high-quality crystal structure and provide evidence of the presence of multiple crystallographic orientations. The TEM image of Ti region (**Figure 3.6a**) reveals that the Ti interlayer is predominantly transformed into titanium dioxide (TiO_2) during the preparation process. In **Figure 3.6d**, two crystalline regions are observed. The one

with a lattice spacing of 0.25 nm is attributed to the (111) plane of titanium carbide (TiC), while the dominant one with a lattice spacing of 0.35 nm is assigned to the (101) plane of TiO_2.[123,124] This indicates a two-step transformation process during and after BDD deposition. Specifically, during the MWCVD growth, carbon atoms diffused into the Ti interlayer and reacted to form TiC at the interface.[125] However, most of the TiC phase has been oxidized into stable TiO_2 in an oxygen-rich atmosphere during the subsequent thermal oxidation treatment of the as-synthesized DC at 450 °C.

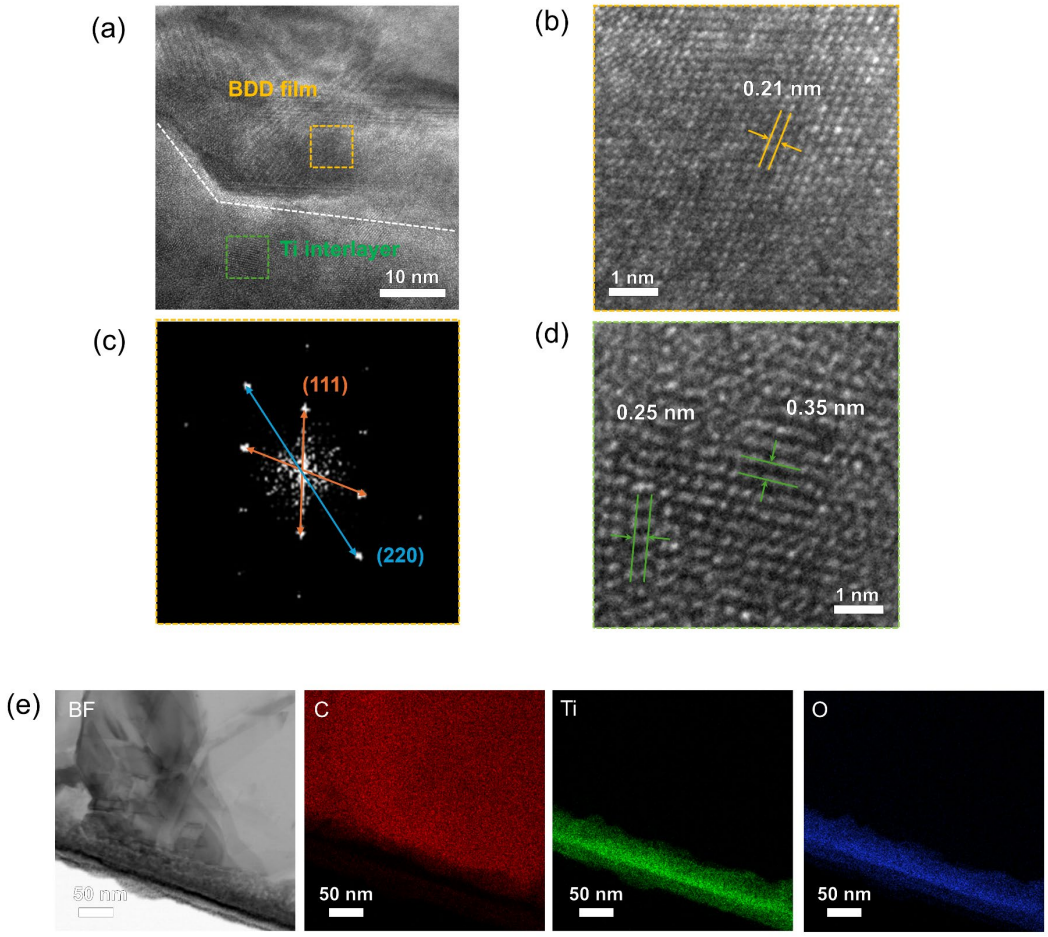


***Figure 3.6**. (a) Cross-sectional TEM image of the transition region. HRTEM images of (b) BDD region, and (d) Ti interlayer. (c) FFT pattern recorded from BDD film region. (e) EDX elemental mapping analysis of C, Ti, O from the transition region.*

The elemental distribution (**Figure 3.6e**) that was obtained through EDX elemental mapping provides further insight into the composition of the transition region. The C

signal is mainly localized in the BDD region, while Ti is strongly concentrated at the interlayer. A significant O signal is detected overlapping with the Ti-rich region, supporting the formation of TiO_2. Interestingly, a partial overlap between the C and O signals is also observed, which suggests a compositional gradient and incomplete oxidation of TiC. Consequently, the transition region is characterized by the coexistence and transformation of TiC and TiO_2.

The crystalline structure of the DC material was further investigated using XRD. For comparison, the XRD patterns of the bare CC substrate were analyzed. Related spectra are shown in **Figure 3.7a**. Both patterns exhibit a prominent diffraction peak at 2 Theta (2θ) around 25.7 °, corresponding to a characteristic plane (002) of graphite, which reflects the layered structure of sp^2-hybridized carbon in the CC substrate. Furthermore, a smaller peak is observed at approximately 42.1 °, associated with the (100), an additional indication of the graphite presence.[57] In contrast to the CC substrate, the DC sample exhibits additional diffraction peaks at 43.8 ° and 75.1 °, which are attributed to the (111) and (220) planes of crystalline diamond, respectively.[126] The intensity of the diamond (111) peak is particularly strong, suggesting preferential growth along the (111) orientation during the MWCVD process. The presence of both graphite- and diamond-related peaks in the DC pattern reflects the composite nature of the electrode.

It is worth noting that no distinct diffraction peaks corresponding to TiC or TiO_2 are observed in the XRD pattern of DC. This absence can be attributed to the extremely thin Ti interlayer, which is only approximately 20—30 nm thick. Such a small thickness results in a very low volume fraction of Ti relative to the entire sample and therefore leads to signal intensity below the detection limit. Additionally, the interlayer is partially amorphous, and the crystal grains are only several nanometers in diameter (**Figure 3.6a, Figure 3.6d**), further contributing to the lack of detectable diffraction features.

To further validate the diamond crystal structure of this DC material, Raman spectroscopy was performed, and some typical results are shown in **Figure 3.7b**. The Raman spectrum of the CC displays two prominent and broad peaks at approximately 1356 cm^{-1} and 1594 cm^{-1}, corresponding to the D band and G band, respectively. These

features are characteristic of disordered sp^2 carbon and graphitic structures. In contrast, the Raman spectrum of the DC sample reveals a sharp and intense peak centered at 1337 cm^{-1}, which is a signature of sp^3-hybridized carbon in crystalline diamond.[127] The relatively narrow full width at half maximum (FWHM) of the diamond peak indicates high crystallinity. The boron to carbon (B/C) ratio in the gas phase used for synthesis was 12,500 ppm. In combination with the thickness of obtained BDD film, the boron concentration is estimated to be approximately 2×10^{21} cm^{-3}.[128,129] Such a high boron-doping level is expected to induce metal-like conductivity in the diamond film, which is favorable for SC applications requiring fast electron transport and stable electrochemical performance.

To further examine the surface chemical composition and bonding configurations of DC electrode, a high-resolution XPS analysis was conducted. The C 1s spectrum (**Figure 3.7c)** reveals multiple chemically distinct carbon states. The dominant peak centered at 284.8 eV is assigned to C–C bonds, which are characteristic of sp^3-hybridized carbon and indicative of the diamond lattice.[130] Additionally, a secondary peak at approximately 286.3 eV is attributed to C–O bonds, suggesting the presence of oxygen-containing functional groups such as hydroxyl or ether groups. A weaker but discernible peak observed at approximately 287.6 eV corresponds to C=O bonds, typically arising from carbonyl or carboxyl functionalities. A small peak around 289.2 eV can be linked to O–C=O bonds, reflecting the presence of ester or carboxylate moieties. Complementary information is provided by the O 1s spectrum (**Figure 3.7d**), which exhibits three main peaks located at approximately 531.5 eV, 532.1 eV, and 533.5 eV, corresponding to C=O, C–O, and O–C=O species, respectively.[131] These oxygen-containing groups are assumed to result from thermal oxidation treatment and are concentrated on the BDD film surface. The presence of these oxygen functional groups not only improves the hydrophilicity and electrolyte accessibility of the electrode but also provides additional active sites for electrochemical reactions, thereby potentially enhancing the capacitive performance of the flexible DC electrode.[61]

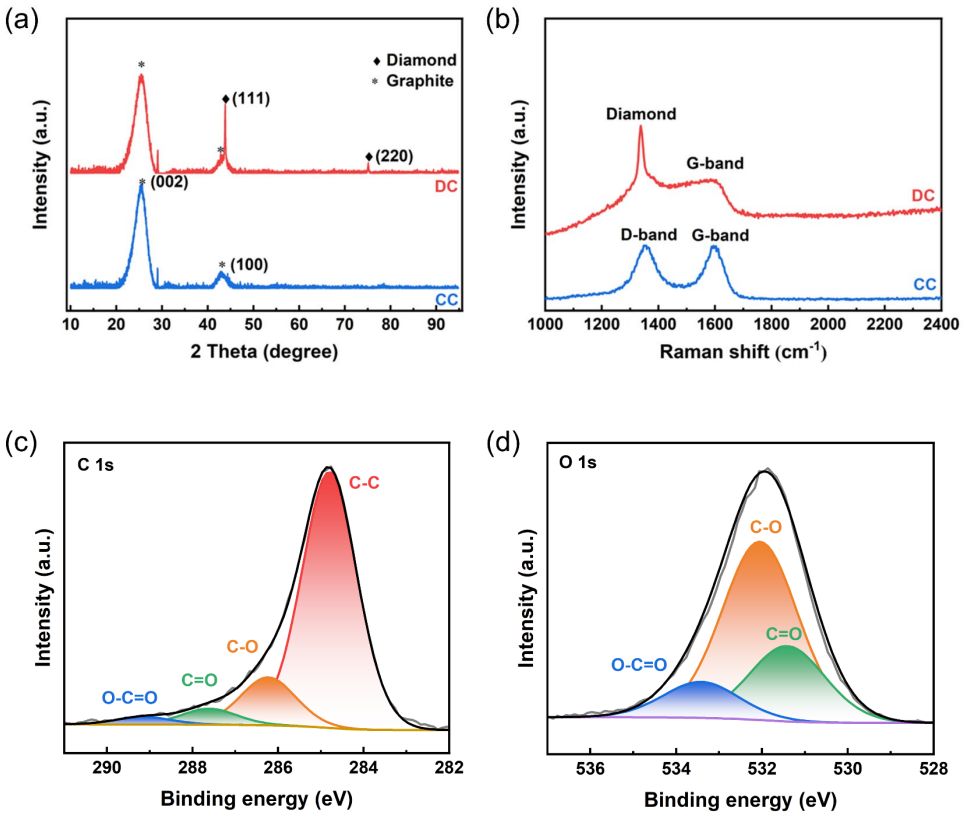


***Figure 3.7**. (a) XRD patterns, (b) Raman spectra of DC and CC. High-resolution XPS spectra of (c) C 1s and (d) O 1s for the DC sample.*

3.3 Electrochemical performance of diamond cloth

3.3.1 Three-electrode system

The electrochemical properties of the DC electrode were systematically investigated by directly employing the DC material as the working electrode in a three-electrode system. Its electrochemical performance was first investigated in comparison to several related materials as control experiments, including planar BDD on silicon (BDD@Si), titanium-coated carbon cloth (Ti@CC) (i.e., sample only after RF-PVD deposition), and bare CC electrode (**Figure 3.8**). In 1.0 M Na_2SO_4 aqueous solution, the CVs were recorded within a potential range from -0.1 V to 0.9 V at a scan rate of 50 mV s^{-1} (**Figure 3.8a**). The DC electrode exhibits a substantially higher current density across the entire

potential range compared to the other samples, indicating superior capacitive performance and a significantly enhanced specific capacitance. Moreover, the CV of the DC electrode displays a more pronounced rectangular profile, characteristic of ideal EDLC behavior. This profile implies efficient adsorption/desorption of ions on the DC electrode and its low charge transfer resistance. The enhanced capacitive performance of the DC electrode can be attributed to several synergistic factors. First, the BDD film on the DC consists predominantly of sp^3 carbon, which not only provides superior surface chemistry, but also higher density of effective active sites for electrochemical reactions. This enhanced surface reactivity contributes to higher capacitance. In addition, BDD films with high boron doping levels (exceeding 10^{20} cm^{-3}) exhibit metal-like conductivity.[60] This significant enhancement in electrical conductivity facilitates the rapid transfer and storage of charges, thereby increasing the capacitance. From a morphological perspective, as previously mentioned, the commercial CC substrate possesses a smooth surface and limited specific surface area (1 m^2 g^{-1}) (**Figure 3.5a**), which restricts its capacitance.[56] In contrast, the DC electrode has an enlarged specific surface area (18.6 m^2 g^{-1}). The porous woven structure of DC significantly increases the effective electrochemical active area of the entire electrode, allowing the electrolyte to fully penetrate the interior surface of BDD film. The gaps between the fibers provide channels for rapid ion transport, which helps to reduce ion diffusion resistance and further enhance performance. Additionally, thermal oxidation treatment led to the incorporation of oxygen-containing functional groups on the DC surface (**Figure 3.7d**). Consequently, the surface was transformed from hydrophobic to hydrophilic. This modification significantly enhances wettability, thereby increasing the effective contact area between the electrode and electrolyte and improving ion transport, which further boosts the capacitive performance of DC.

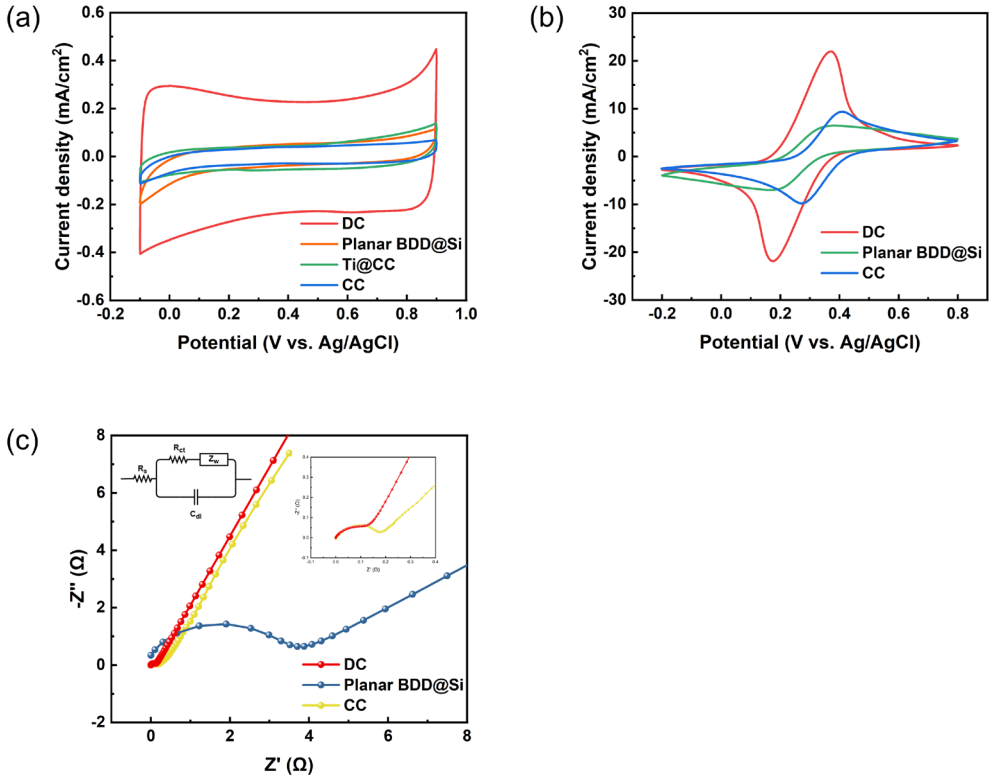


***Figure 3.8**. Comparison of electrochemical performance of different electrodes using a three-electrode system: (a) CVs at a scan rate of 50 mV s^{-1} in 1.0 M Na_2SO_4 solution, (b) CVs at a scan rate of 20 mV s^{-1} and (c) Nyquist plots achieved in 0.05 M $Fe(CN)_6^{3-/4-}$ + 1.0 M Na_2SO_4, the inset shows an enlarged view of the beginning.*

The measurements were also conducted in the redox-active electrolyte solution of 0.05 M $Fe(CN)_6^{3-/4-}$ + 1.0 M Na_2SO_4. In this case, the DC electrode again demonstrates superior performance. As shown in **Figure 3.8b**, the DC electrode exhibits significantly larger peak currents and well-defined redox peaks in comparison to the planar BDD@Si and the bare CC electrode, suggesting superior electron transfer kinetics an enhanced redox activity. The superior performance of the DC electrode can be attributed to its high conductivity and well-optimized design, which facilitates faster charge transfer processes and provides accessible active sites for redox reactions. EIS further corroborates the superior electrochemical performance of the DC electrode. As shown in the Nyquist plot (**Figure 3.8c**), the DC electrode exhibits the smallest semicircle in the high-frequency

region among all characterized electrodes, indicating the lowest charge transfer resistance (R_{ct}) and hence reflecting its superior interfacial electron transfer capability.[132] The inset provides a magnified view of the high-frequency region, clearly illustrating the comparison of semicircle between DC and CC electrodes. In the low-frequency Warburg region, characterized by the linear diffusion-controlled portion, the DC electrode demonstrates ion diffusion efficiency nearly comparable to that of the CC electrode, characteristic of nearly ideal capacitive behavior with fast ion transport and minimal diffusion limitation. In summary, DC material exhibits remarkable capacitive properties and holds great potential for the construction of both EDLCs and PCs.

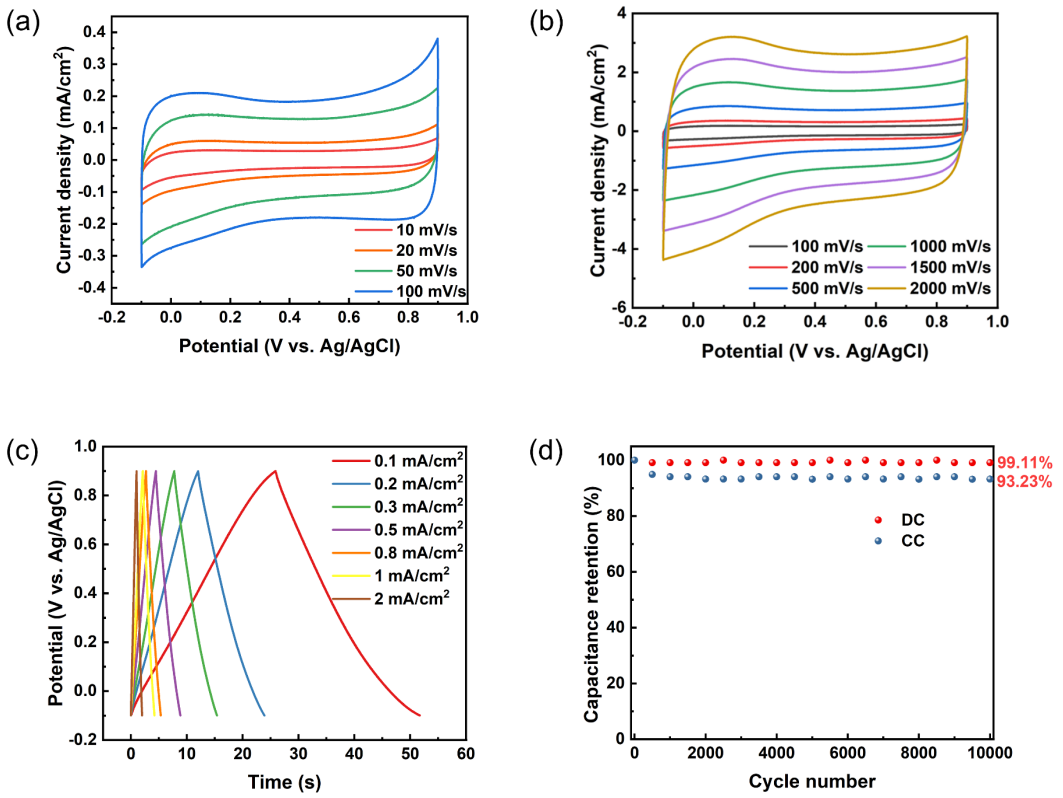


***Figure 3.9**. Electrochemical performance of DC electrode in a three-electrode system in a 1.0 M Na_2SO_4 electrolyte: (a), (b) CVs at different scan rates; (c) GCD curves at different current densities; (d) Capacitance retention during 10,000 charging-discharging cycles in comparison with that of the bare CC electrode.*

The capacitive characteristics of the DC electrode were further explored to assess its

potential for application in both EDLCs and PCs. The electrochemical characterization was performed in a three-electrode system. The electrochemical behavior of DC as EDLC electrode was evaluated in 1.0 M Na_2SO_4 aqueous solution within the potential range of -0.1—0.9 V at different scan rates and charging-discharging current densities. As shown in **Figure 3.9a**, CVs exhibit nearly rectangular shapes, indicating typical EDLC behavior with efficient charge storage, and fast and reversible charging-discharging processes. The estimated specific capacitances are 3.05, 2.87, 2.69, and 2.07 mF cm^{-2} at the scan rates of 10, 20, 50, and 100 mV s^{-1}, respectively. The CV profiles still remain almost rectangular-like shape even when the scan rate increases to as high as 2000 mV s^{-1} (**Figure 3.9b**), reflecting excellent rate capability. The deviation from the ideal rectangular shape at higher scan rates reflects the reduced efficiency in charging-discharging processes due to limited ion diffusion and a generated overpotential.[133] Meanwhile, the GCD curves were collected at different current densities, ranging from 0.1 to 2 mA cm^{-2} (**Figure 3.9c**). The nearly symmetric triangular shapes of the GCD curves and the absence of significant *IR*-drop highlight the high electronic conductivity, excellent coulombic efficiency, and high reversibility of the DC electrode in an EDLC. The calculated specific capacitances are 2.74, 2.54, 2.45, 2.35, 2.26, 2.23 and 2.10 mF cm^{-2} at the current densities of 0.1, 0.2, 0.3, 0.5, 0.8, 1 and 2 mA cm^{-2}, respectively, further confirming the excellent rate capability of the electrode. Furthermore, long-term cycling performance was evaluated at a current density of 0.8 mA cm^{-2} over 10,000 charging-discharging cycles (**Figure 3.9d**). The DC electrode exhibits excellent cycling stability with a capacitance retention of 99.11 % of its initial capacitance, indicating outstanding durability and minimal performance degradation over prolonged operation. In comparison, the bare CC electrode shows a lower capacitance retention of 93.23 %, suggesting comparatively higher degradation during long-time charging-discharging processes.

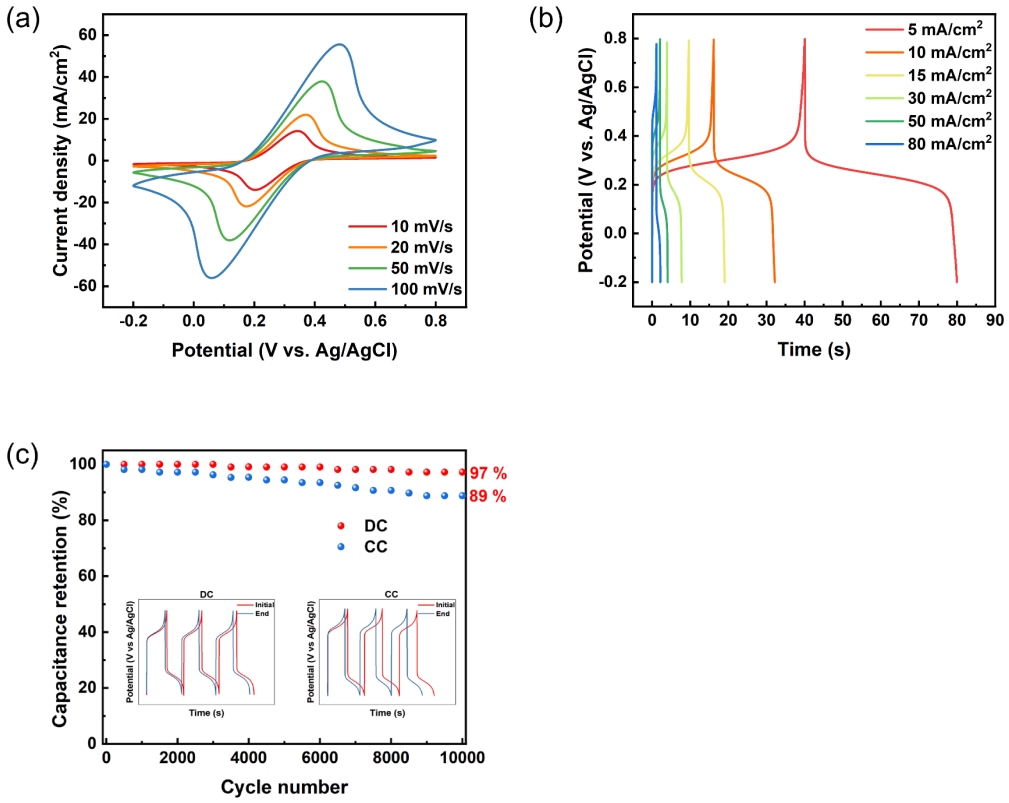


***Figure 3.10**. Electrochemical performance of DC electrode in a three-electrode configuration in a 1.0 M Na_2SO_4 solution containing 0.05 M $Fe(CN)_6^{3-/4-}$ redox species: (a) CVs at different scan rates; (b) GCD curves at different current densities; (c) Capacitance retention during 10,000 charging-discharging cycles in comparison with that of the bare CC electrode, the insets show the comparison of GCD curves before and after cycling.*

To further explore the electrochemical properties of the DC electrode beyond EDLCs, its performance was evaluated in an aqueous redox-active electrolyte composed of 0.05 M $Fe(CN)_6^{3-/4-}$ and 1.0 M Na_2SO_4 within a potential range of -0.2 to 0.8 V. The CVs recorded at various scan rates are presented in **Figure 3.10a**. The well-defined and symmetric oxidation and reduction peaks are observed at all scan rates, confirming the efficient electron transfer kinetics of the DC electrode. The proportional increase of peak current with the scan rate indicates a surface-controlled redox process, which is characteristic of the fast and reversible redox reaction of $Fe(CN)_6^{3-/4-}$. The slight peak shifts and

broadening at higher scan rates (50 and 100 mV s^{-1}) suggest minor limitations in ion diffusion and charge transfer kinetics, indicating good electrochemical stability. Besides, the shape and the absolute value of the oxidation peaks are almost identical to that of reduction peaks, demonstrating the outstanding reversibility of pseudocapacitive behavior.[134] The specific capacitances were calculated from CVs, which are 246.0, 208.5, 167.2, and 138.7 mF cm^{-2} at the scan rates of 10, 20, 50, and 100 mV s^{-1}, respectively. The GCD curves recorded at current densities ranging from 5 to 80 mA cm^{-2} are shown in **Figure 3.10b**. These curves exhibit clear nonlinear profiles with distinct potential plateaus, suggesting the typical pseudocapacitive behavior associated with faradaic reactions. The estimated capacitances are 212.0, 170.8, 151.6, 140.9, 108.0, and 92.1 mF cm^{-2} at the current densities of 5, 10, 15, 30, 50 and 80 mA cm^{-2}, respectively. The gradual decrease in capacitance with increasing current density arises from kinetic limitations in ion diffusion and charge transfer at high rates. Notably, the specific capacitance of the DC electrode in PC is nearly two orders of magnitude higher than in EDLC at equivalent scan rates or current densities, highlighting the enhanced charge storage facilitated by redox-active species. Cycling durability was also assessed in the redox-active electrolyte through long-time charging-discharging over 10,000 cycles (**Figure 3.10c**). The DC electrode retains 97 % of its initial capacitance after 10,000 cycles, whereas the CC electrode exhibits more pronounced degradation, with only 89 % retention. The excellent capacitance retention of the DC electrode in both EDLC and PC can be attributed to the BDD film shell, which provides exceptional chemical inertness, structural rigidity, and resistance against surface degradation.[135] This contrasts with the CC electrode, where the exposed sp^2 carbon surface is more prone to electrochemical oxidation, structural degradation, and loss of active sites under repeated cycling conditions.

3.3.2 Two-electrode system

To evaluate the practical applicability of the DC electrode, two-electrode symmetric SCs were fabricated and assessed. Their electrochemical behavior, including parameters such as energy density and power density, was assessed in both non-faradaic media and redox-active electrolyte.

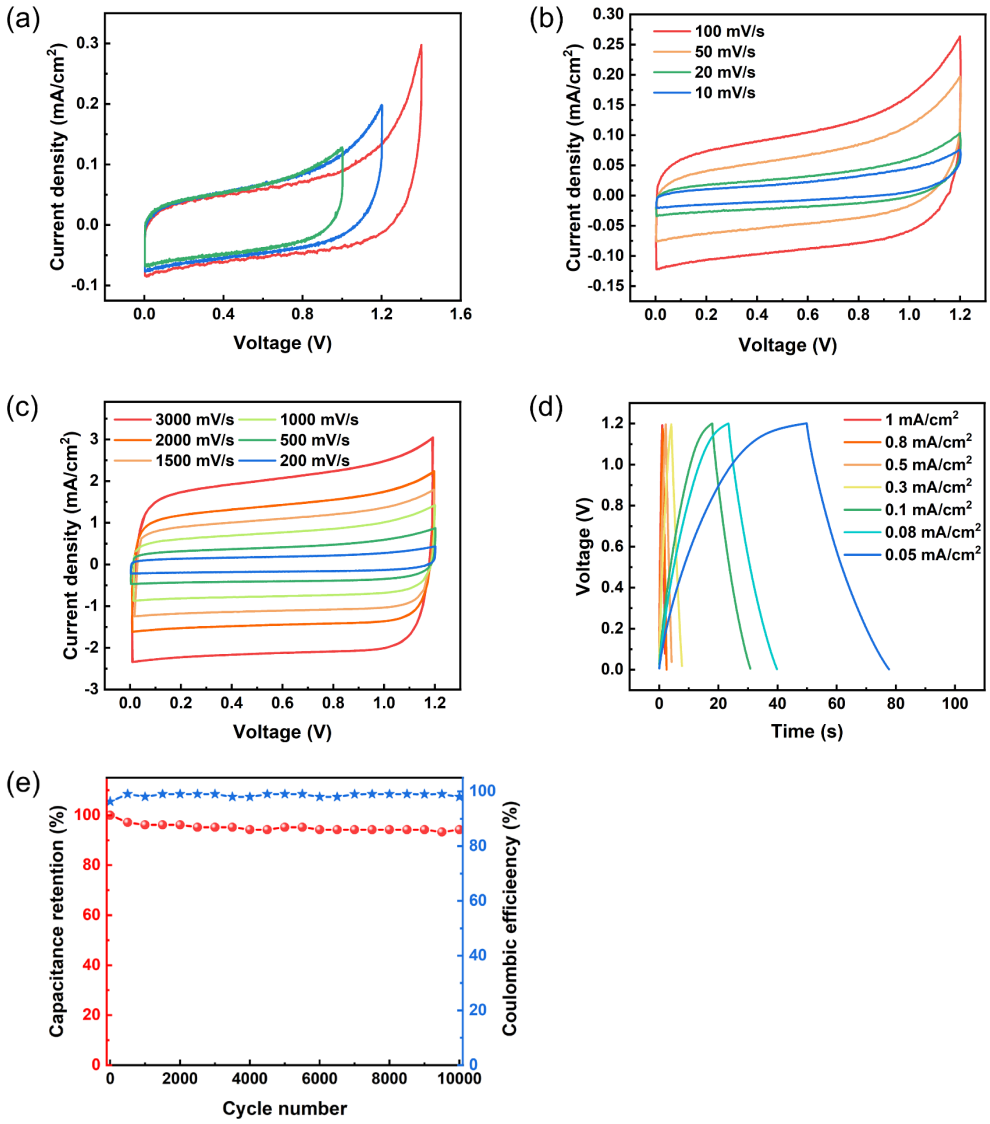


Figure 3.11. *Electrochemical performance of symmetric EDLC using DC electrodes in a two-electrode system in 1.0 M Na_2SO_4 solution: CVs of a symmetric EDLC (a) with different scanning voltage ranges at a scan rate of 50 mV s^{-1}, and (b) within a voltage range of 1.2 V at different scan rates, (c) at high scan rates; (d) GCD curves of a symmetric EDLC at different current densities; (e) Capacitance retention and coulombic efficiency during 10,000 charging-discharging cycles.*

The two-electrode symmetric EDLC was initially fabricated and evaluated in a 1.0 M Na_2SO_4 aqueous solution. The CV profiles of the EDLC exhibit a quasi-rectangular shape within the working voltage extending up to 1.2 V (**Figure 3.11a)**, indicating ideal double-

layer behavior and good electrochemical stability at relatively high cell voltage. CVs recorded at scan rates ranging from 10 to 100 mV s^{-1} under a cell voltage of 1.2 V are presented in **Figure 3.11b**. At lower scan rates, the CVs retain a nearly ideal rectangular shape, characteristic of efficient electric double-layer charge storage and minimal resistive distortion. The calculated specific capacitances of each DC electrode are 0.76, 0.63, 0.57, and 0.49 mF cm^{-2} at the scan rates of 10, 20, 50 and 100 mV s^{-1}, respectively. The tendency of these values is consistent with those obtained from the three-electrode system, suggesting reproducible performance across different configurations. Remarkably, the symmetric EDLC exhibits exceptional rate capability, as shown in **Figure 3.11c**. Even at ultra-high scan rates of up to 3000 mV s^{-1}, the CVs maintain a symmetric, rectangular shape, further confirming the excellent double-layer capacitive behavior, fast ion transport, and minimal diffusion resistance. The GCD curves of this symmetric EDLC recorded at various current densities are presented in **Figure 3.11d**. The GCD profiles are nearly linear and symmetric, again suggesting excellent capacitive behavior with minimal resistance-induced distortion. The curves retain their symmetric nature throughout all current densities, demonstrating high coulombic efficiencies and stable charging-discharging characteristics. Notably, the negligible voltage drop at the beginning of the discharging phase implies low internal resistance and efficient charge transfer processes within the electrode. The specific capacitances of each DC electrode were calculated. They are 0.86, 0.70, 0.68, 0.51, 0.46, 0.44, and 0.42 mF cm^{-2} at the current densities of 0.05, 0.08, 0.1, 0.3, 0.5, 0.8, and 1 mA cm^{-2}, respectively. The long-term electrochemical durability of the EDLC was further evaluated *via* continuous charging–discharging cycling over 10,000 cycles at a constant current density. As illustrated in **Figure 3.11e**, the symmetric EDLC retains a capacitance retention of 94 % after 10,000 charging-discharging cycles, demonstrating excellent cycling stability. Furthermore, the coulombic efficiency remains consistently above 98 %, indicating minimal internal energy losses and highly reversible charging-discharging processes throughout the operation.

The electrochemical behavior of the symmetric PC assembled using DC electrodes was

further evaluated in a two-electrode configuration. The device was investigated in 1.0 M Na_2SO_4 aqueous solution containing 0.05 M $Fe(CN)_6^{3-/4}$. The voltage ranged from -0.8 V to 0.8 V. As shown in **Figure 3.12a**, the CVs recorded at scan rates from 10 to 100 mV s^{-1} exhibit a pair of symmetric redox peaks across all scan rates, confirming that the dominant charge storage mechanism arises from fast and reversible redox reactions of the $Fe(CN)_6^{3-/4-}$ couple undergoing on the electrode surface. The oxidation and reduction peaks exhibit nearly equal current magnitudes, indicating excellent electrochemical reversibility and high redox efficiency. The calculated specific capacitances of this PC are 81.94, 69.46, 55.57, and 46.82 mF cm^{-2} at the scan rates of 10, 20, 50 and 100 mV s^{-1}, respectively. GCD measurements were performed at various current densities ranging from 5 to 80 mA cm^{-2} (**Figure 3.12b**). The curves exhibit symmetrical charging-discharging profiles, indicating high coulombic efficiency, excellent charge transfer reversibility, and low internal resistance. The estimated specific capacitances are 64.63, 52.44, 46.79, 38.31, 32.84, and 24.81 mF cm^{-2} at the current densities of of 5, 10, 15, 30, 50 and 80 mA cm^{-2}, respectively. The gradual decline in capacitance with increasing current density is attributed to kinetic limitations in ion diffusion at high rates. Similar to the capacitances calculated in a three-electrode system, the capacitances of a symmetrical PC are much higher than those of a symmetrical EDLC. This enhancement arises from the synergistic contribution of two mechanisms: (i) electric double-layer capacitance, due to electrostatic charge/ion accumulation at electrode-electrolyte interface, and (ii) pseudocapacitance, originating from fast surface redox reactions of the $Fe(CN)_6^{3-/4-}$ redox pair. The long-term cycling stability of the symmetric PC was also evaluated over 10,000 continuous charging-discharging cycles. As shown in **Figure 3.12c**, the capacitance retention of this symmetrical PC remains 100 % after 10 000 charging-discharging cycles, demonstrating exceptional electrochemical durability. Meanwhile, the coulombic efficiency remains consistently close to 100 % throughout cycling, further confirming the high reversibility and low energy loss of the system. In summary, both symmetrical EDLC and PC constructed with DC material as electrodes exhibit extremely high cycling stability, which is one of the most significant features of SCs.

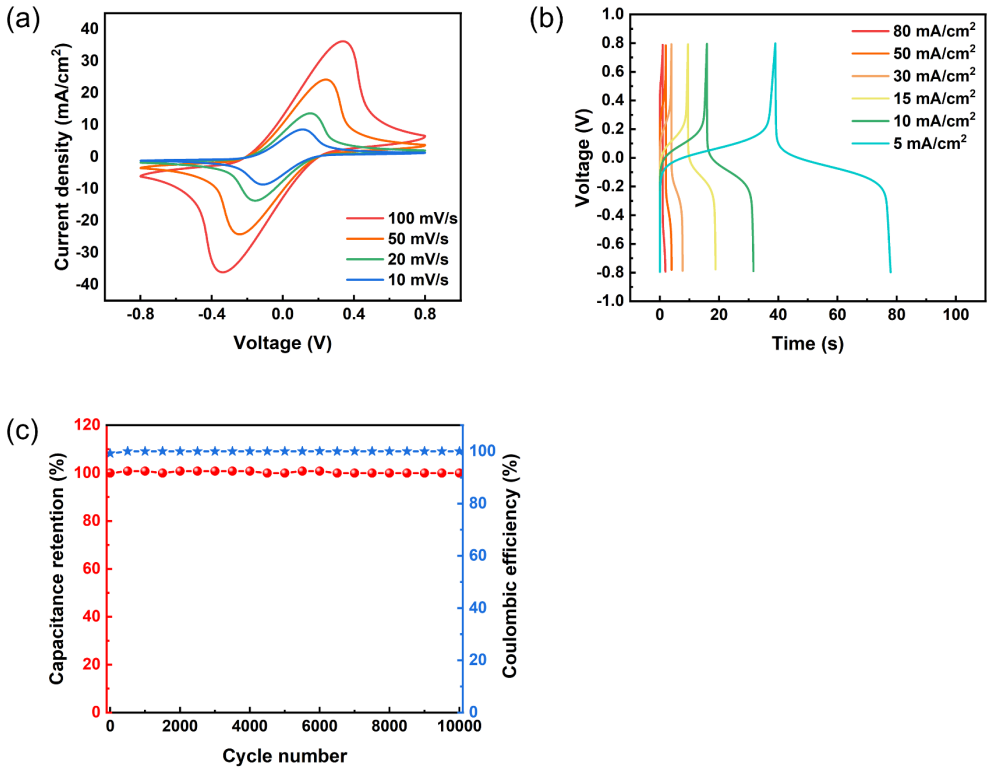


***Figure 3.12**. Electrochemical performance of symmetric PC using DC electrodes in a two-electrode system in 1.0 M Na_2SO_4 solution containing 0.05 M $Fe(CN)_6^{3-/4-}$: (a) CVs of a symmetric PC at different scan rates; (b) GCD curves of a symmetric PC at different current densities; (c) Capacitance retention and coulombic efficiency during 10,000 charging-discharging cycles.*

3.3.3 Energy and power density

The energy density and power density are two critical parameters for evaluating the overall performance of SC devices. In this section, the area-specific energy and power densities of the symmetric SCs were calculated from GCD curves obtained at various current densities. The area-normalized values were used to avoid ambiguity often encountered in gravimetric comparisons due to differences in electrode mass loading.[61] These values are summarized and benchmarked against other diamond-based and carbon-related SC devices in **Figure 3.13**.

The energy and power densities of the symmetric EDLC were shown in the Ragone plots in **Figure 3.13a**. It can be easily found that it exhibits superior performance compared to EDLCs based on other related electrode materials.[136–139] For instance, the DC-based EDLC exhibits a maximum of energy density of 0.18 μWh cm^{-2} at a power density of 23.29 μW cm^{-2}. Even at a high power density of 351.85 μW cm^{-2}, the energy density still remains 0.09 μWh cm^{-2}. However, in terms of the absolute values of energy densities and power densities, the symmetric EDLC based on DC electrodes delivers relatively modest performance, as is typical of EDLCs due to the purely electrostatic charge storage mechanism. This result is consistent with previously reported EDLCs using diamond-based materials and reflects the intrinsic limitations of double-layer capacitance in storing energy. In contrast, the symmetric PC based on the same DC electrodes but operating in a redox-active electrolyte demonstrates significantly enhanced performance. It achieves a maximum energy density of 45.96 μWh cm^{-2} at a power density of 4.25 mW cm^{-2}. Even at a power density of 67.93 mW cm^{-2}, it still delivers an energy density of 17.64 μWh cm^{-2}. This performance highlights the contribution of the redox-active electrolyte to the energy density of the symmetric SC, while maintaining its power delivery capabilities. Comparative analysis with previously reported PCs based on carbon-based materials further underscores the competitive advantage of the DC-based symmetric PC. As illustrated in **Figure 3.13b**, its energy and power densities are not only comparable to but in many cases exceed those of the previously reported carbon-based flexible SC systems.[57,73,140–144] For example, our symmetrical PCs exhibits even slightly better electrochemical performance in terms of the maximal energy density and power density when compared with the symmetrical PCs using 3D diamond/graphite composite film covered CC as electrodes (43.08 μWh cm^{-2} and 7.00 mW cm^{-2}).[57] Furthermore, its energy densities and power densities are superior to those of the others. For instance, the best-performing fCC-PANI array-rGO-based flexible EDLC merely demonstrates a maximum energy density of 17.51 μWh cm^{-2} and a maximum power density of 20.00 mW cm^{-2}.[140] The symmetrical PC assembled with vertically aligned carbon nanofiber/diamond delivers an energy density 18.17 μWh cm^{-2} and a power density of 10.00 mW cm^{-2}.[73]

In summary, while the energy density of the DC-based EDLC is limited by its electrostatic adsorption/desorption mechanism, the DC-based PC exhibits exceptional energy and power densities, demonstrating superior pseudocapacitive behavior, high-rate capability, and outstanding electrochemical efficiency. In combination with the acquired high capacitances and excellent cycling stability, DC-based PC holds immense potential in the practical application of energy storage.

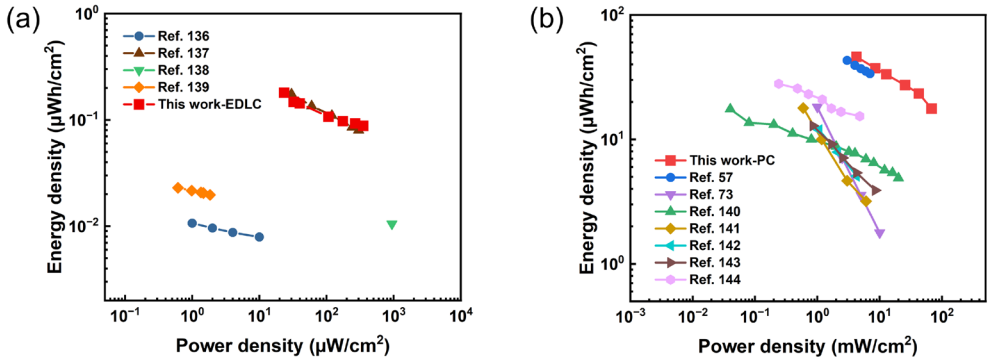


***Figure 3.13**. Ragone plots of (a) the symmetric EDLC and (b) the symmetric PC using DC electrodes in comparison to other diamond and carbon related SCs.*

3.3.4 Mechanical flexibility and stability

To evaluate the potential of our DC electrodes for wearable and portable electronic devices, the mechanical flexibility under deformation was further investigated. For this purpose, a flexible symmetric EDLC was assembled using a gel electrolyte containing 0.5 M Na_2SO_4, as illustrated in **Figure 2.5**. The electrochemical performance was tested under various mechanical bending conditions, from the flat state to bending angles of 60 °, 90 °, and 180 °, as shown in **Figure 3.14a**. The CVs were recorded at a scan rate of 50 mV s^{-1} under these bending states. Compared with CVs obtained in aqueous electrolyte, the voltammograms in gel electrolyte show slight differences, which are due to reduced ionic conductivity and mobility in the gel medium. The CVs recorded at various bending angles exhibit a minor deviation compared to the curve recorded in the flat state. However, the overlapping nature of the CVs under flat and bent conditions indicates that the device

maintains a relatively consistent performance, demonstrating superior mechanical flexibility of the DC EDLC device. To further assess the durability under repeated mechanical deformation, a bending fatigue test was performed by subjecting the device to 500 cycles of flat-to-180° back-and-forth bending. The capacitance retention was monitored *via* the GCD measurements at each interval (**Figure 3.14b**). While small fluctuations in capacitance are observed throughout the test, the lowest retention remains as high as 97 % of the initial value. This is indicative of excellent properties such as high mechanical flexibility and excellent durability of DC electrodes under dynamic deformation. This high retention ratio underscores the structural integrity and intimate contact between the BDD film and the CF scaffold, even under severe mechanical stress. In summary, the DC electrode exhibits superior mechanical flexibility, structural integrity, and stable electrochemical performance under bending deformation, confirming its promising potential for wearable and portable energy storage applications.

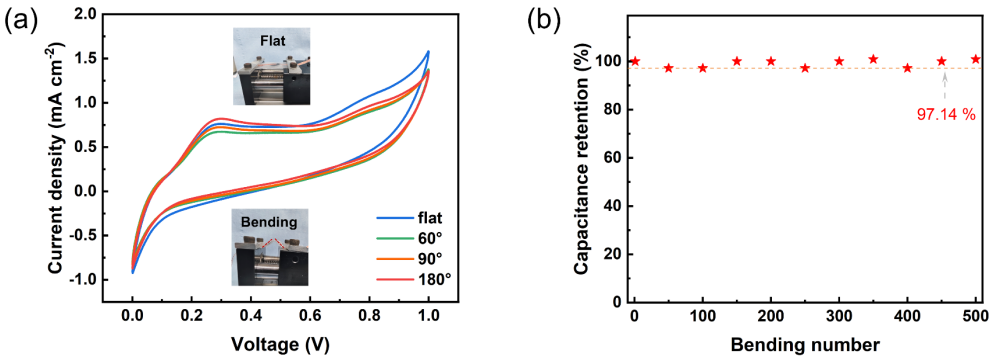


***Figure 3.14**. Bending test: (a) CVs of the symmetric EDLC at different bending angles at a scan rate of 50 mV s^{-1}. (b) the cycling stability of the EDLC for 500 bending times. The insets in (a) are the photographs of the EDLC at flat and bending states.*

3.4 Conclusions

Flexible DC material has been successfully synthesized by overgrowing BDD thin films over the commercially available CC substrate using a MWCVD technique. To protect the CC substrate from plasma etching and improve the adhesion between BDD

film and the substrate, a 20-30 nm Ti thin film has been sputtered onto the CC substrate prior to BDD deposition, serving as both a protective and adhesion-promoting interlayer. The electrochemical performance of the synthesized DC electrodes has been comprehensively evaluated using both three-electrode and two-electrode configurations. Across all testing conditions, the DC electrodes demonstrate remarkable electrochemical performance, including high specific capacitance, low charge transfer resistance, exceptional coulombic efficiency, excellent cycling stability, and impressive energy densities and power densities. It is particularly emphasized that the DC maintain nearly 100 % coulombic efficiency throughout prolonged testing, and there is only slight degradation in capacitance retention over 10,000 charging-discharging cycles, underscoring its long-term reliability. In particular, the symmetric PC assembled with DC electrodes exhibits significant attributes such as high capacitances, enduring stability, remarkable power densities, and elevated energy densities. The performance is superior to the other carbon-based flexible SCs. In addition to superior electrochemical performance, the DC electrodes also demonstrate excellent mechanical flexibility and robustness, as confirmed by bending tests under various angles and repeated deformation. The nearly unchanged electrochemical behavior under mechanical stress indicates that the DC electrode maintains its integrity and conductivity during operation. Therefore, the combination of high electrochemical performance and excellent mechanical flexibility establishes the diamond cloth as a highly promising electrode material of energy storage units for wearable and portable electronics.

4 $NiMnO_x$-Coated Carbon Cloth

To improve the specific capacitance and energy density of SCs, incorporation of pseudocapacitive materials that store charge through fast and reversible Faradaic reactions has emerged as an effective strategy.[76] Among various pseudocapacitive candidates, manganese oxides (MnO_x) stand out due to their high theoretical capacitance, environmental compatibility, natural abundance, and cost-effectiveness.[85] However, MnO_x is often limited by its poor electrical conductivity and insufficient structural stability during long-term cycling. A promising approach to mitigate these issues is the incorporation of to form Ni–Mn-based composite materials (i.e., $NiMnO_x$), which is expected to enhance electrical conductivity, improve electrochemical activity, and stabilize the microstructure.[90,91]

This chapter details the exploration of NiMnOx deposited directly onto the CC substrate. Two synthesizing approaches (i.e., hydrothermal synthesis and electrodeposition method) have been applied to deposit metal oxide films onto the CC substrate. The resulting electrodes are comprehensively characterized and compared in terms of morphology, structure, and electrochemical properties. In addition, the critical role of nickel incorporation has been investigated. Finally, a comprehensive evaluation of the structural, morphological, and electrochemical performance of the resulting $NiMnO_x$@CC electrode has been conducted.

4.1 Comparison of hydrothermal synthesis and electrodeposition

Two preparation routes for the synthesis of manganese oxides film were investigated and compared: hydrothermal synthesis and cathodic electrodeposition. The experimental parameters for each method are summarized in **Table 2.3**. Hydrothermal synthesis was performed under different precursor concentrations and reaction durations (i.e., samples from SH-1 to SH-5), whereas electrodeposition was conducted under a constant potential in a $MnSO_4$ electrolyte (i.e., sample SE-Mn). The morphology and electrochemical features of the fabricated samples are herein compared and discussed.

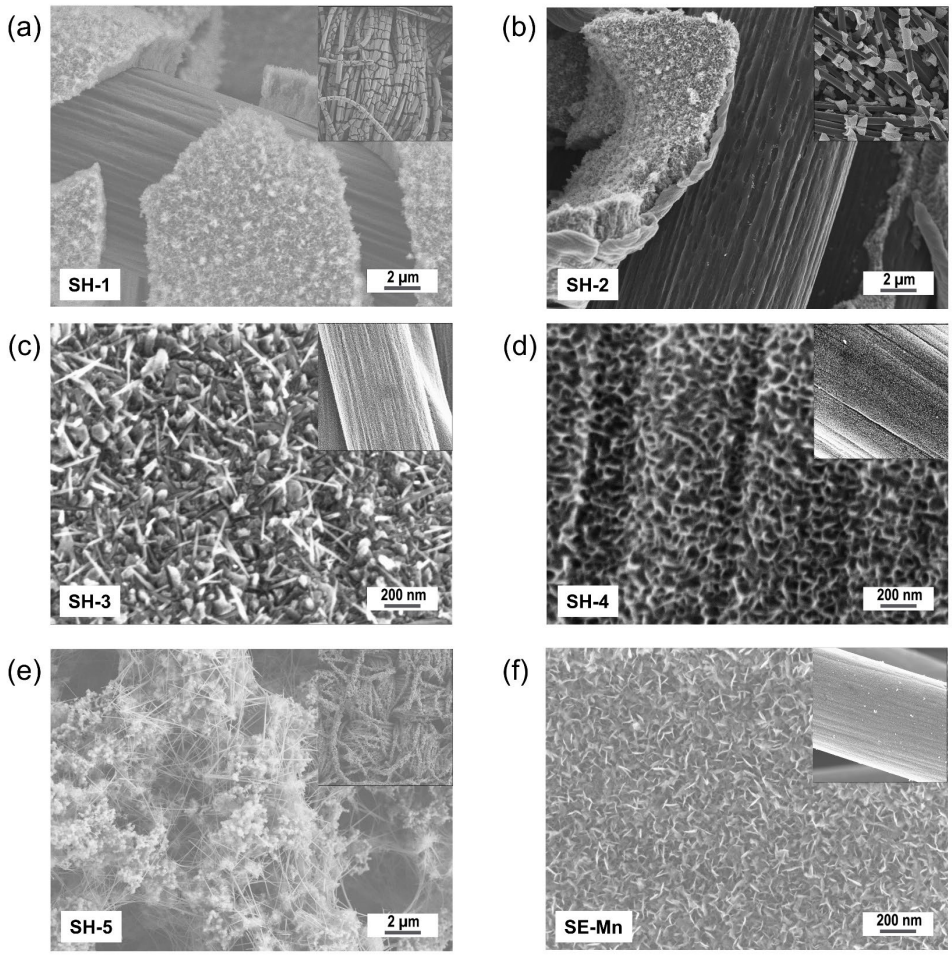


***Figure 4.1**. FESEM images of (a)-(e) SH samples prepared through hydrothermal synthesis, and (f) SE-Mn sample prepared through electrodeposition. The insets are the corresponding low-magnification images.*

The FESEM images of five hydrothermal samples and one electrodeposited sample are shown in **Figure 4.1**. In case of sample SH-1 (**Figure 4.1a**), a substantial amount of manganese oxides is visible, synthesized under a higher $KMnO_4$ concentration (20 mM), a higher reaction temperature (150 °C), and long operation time (5 h). However, the resulting film is discontinuous with poor surface coverage. Despite the application of the precursor with reduced concentration (10 mM), the sample (SH-2, **Figure 4.1b**) does not show any notable improvement in its morphology. The coverage becomes even worse. In these synthesis processes, the permanganate ions are supposed to be reduced by carbon to form Mn ions in lower oxidation states, leading to a pronounced etching of CFs as

illustrated in **Figure 4.1b**. Such etching is expected to negatively affect the long-term stability of these samples when they are used as capacitor electrodes. To mitigate the severe etching and enhance the poor coverage observed in SH-1 and SH-2, more mild synthesis parameters were then implemented, including a lower $KMnO_4$ concentration (5 mM), a reduced temperature (80 °C), and a shorter reaction time (1—2 h). As expected, these milder conditions effectively suppress excessive CFs degradation and facilitate more uniform deposition of manganese oxides, as shown by SH-3 (**Figure 4.1c**) and SH-4 (**Figure 4.1d**). In comparison between SH-3 and SH-4, an extended reaction time significantly changes the morphology of MnO_x, transforming from granular and needle-like to flake-like network. For SH-5 (**Figure 4.1e**), $MnSO_4$ was introduced to replace carbon as reductant. In this case, the reduction of MnO_4^+ is expected to proceed predominantly in the solution phase rather than at the carbon surface. Consequently, a large amount of MnO_x is precipitated and deposited onto the CC, yielding a thick but highly non-uniform film. The related FESEM image shows a web-like network of ultrathin nanowires/whiskers spanning across the fiber scaffold, interspersed with micron-scale, flower-like aggregates. This irregular and loose agglomerated film probably leads to uneven current distribution, increased contact resistance, and weakened the mechanical robustness in electrochemical applications. In contrast, the electrodeposited MnO_x film, as shown for SE-Mn in **Figure 4.1f**, consists of a dense and compact nanosheets structure, which uniformly covers the entire CFs with a homogeneous thickness. Compared with hydrothermal synthesis, electrodeposition method seems to offer several decisive advantages, including good controllability of conformality and thickness, effective substrate protection, high reproducibility, and strong adhesion between film and substrate.

The CVs of MnO_x@CC electrodes obtained by the two routes was investigated in 1.0 M Na_2SO_4 aqueous solution at a scan rate of 50 mV s^{-1} (**Figure 4.2**). Samples SH-1 and SH-2 were excluded for these measurements. It is due to the presence of evidently etched substrates and poorly developed morphologies, which compromise the reliability of their electrochemical performance. All hydrothermal samples deliver low current responses

and narrow available potential ranges, indicating limited electrochemical activity. In sharp contrast, the SE-Mn sample exhibits the highest current response, a larger specific capacitance (25.51 mF cm^{-2}), a wider potential window (-0.1—1.4 V), and distinct redox peaks, suggesting superior electrochemical performance. The better behavior of SE-Mn can be ascribed to its microstructure and strong adhesion between the electrodeposited film and the substrate. Again, these comparisons demonstrate the advantages of electrodeposition synthesis in the synthesis of manganese oxide films on CC.

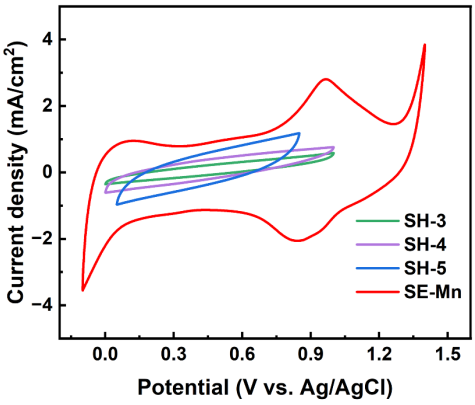


***Figure 4.2**. Comparison of CVs of hydrothermmal sample SH-3, SH-4 and SH-5 with electrodeposited sample SE-Mn at the scan rate of 50 mV s^{-1} in 1.0 M Na_2SO_4 solution.*

4.2 Incorporation of nickel

A trace amount of nickel was co-electrodeposited with MnO_x to yield a mixed Ni–Mn oxides ($NiMnO_x$). **Figure 4.3** compares the i-t curves recorded for electrodeposition using three different electrolytes: (1) 50 mM $MnSO_4$ (for SE-Mn), (2) 3 mM $Ni(CH_3COO)_2$ (for SE-Ni), and (3) 50 mM $MnSO_4$ + 3 mM $Ni(CH_3COO)_2$ (for SE-NiMn). All curves exhibit a high initial current value, followed by a rapid decay to a quasi-steady state, which indicates a double-layer formation and a fast charge transfer process at the initial stage, subsequently constrained by ion diffusion limitations. The steady current values for fabrication of SE-Ni, SE-Mn, and SE-NiMn are approximately 0.005 mA, 0.1 mA, and

0.3 mA, respectively. The current observed for SE-NiMn is three-times higher than that of SE-Mn, which can be attributed to the addition of a trace amount of $Ni(CH_3COO)_2$. Over 1500 s, the theoretical corresponding charges are approximately 7.5 mC, 150 mC, and 450 mC, respectively. This enhancement demonstrates the synergistic effect of the mixed electrolyte in promoting both nucleation density and the growth rate during electrodeposition.

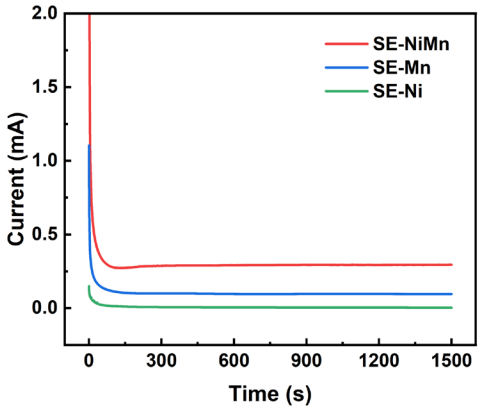


***Figure 4.3**. I-t curves of the electrodeposition of three samples at a constant potential of 0.9 V (vs. Ag/AgCl) for 1500 s.*

The differences in the electrodeposition process induced by electrolyte composition lead to morphological changes of these samples (**Figure 4.4**). In comparison to SE-Mn (**Figure 4.4a**), the SE-NiMn (**Figure 4.4b**) exhibits a denser, thicker, and relatively rougher deposited film, which is an expected consequence of the increased nucleation density and the accelerated deposition rate. For both samples (**Figure 4.4c and 4.4d**), the interconnected nanosheets are uniformly grown on the surface of CFs. Nevertheless, slight morphological differences can be observed between them. The nanosheets tend to coalesce laterally to form continuous bridges, improving film continuity. The surface morphology of interconnected nanosheets facilitates electrolyte penetration and thereby enhances the effective contact between the electrolyte and the electrode.

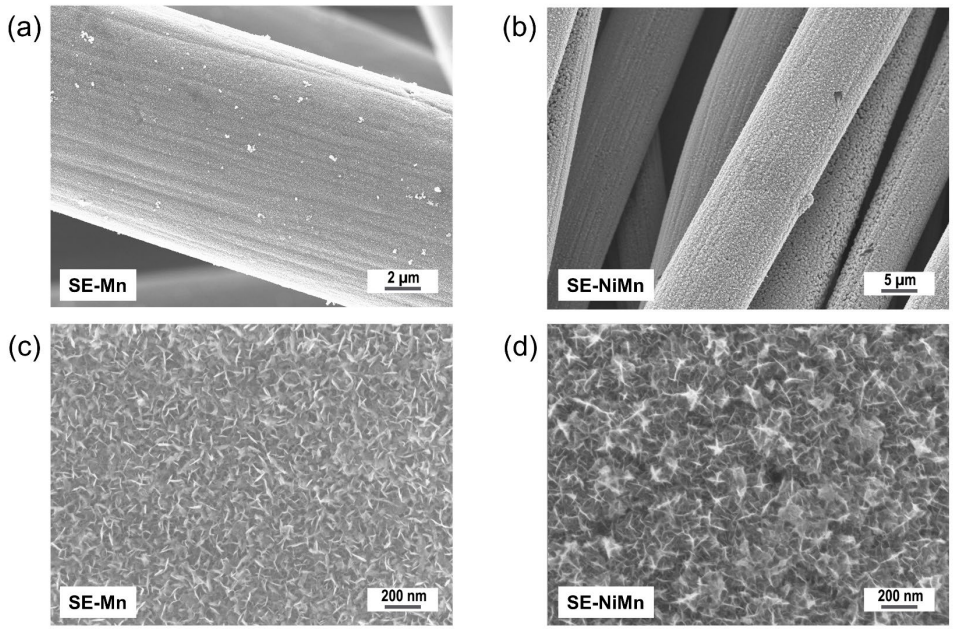


***Figure 4.4**. FESEM images of (a) SE-Mn and (b) SE-NiMn with a low-magnification, and (c), (d) with a high-magnification.*

The electrochemical performance of three samples as working electrodes was investigated in 1.0 M Na_2SO_4 aqueous solution using a three-electrode configuration. The comparison is demonstrated in **Figure 4.5**. A potential window ranging from -0.1 V to 1.4 V is accessible for all three electrodes. It can be attributed to the high oxygen evolution overpotential of the conductive CC substrate.[145] **Figure 4.5a** presents the CVs of the electrodes recorded at a scan rate of 50 mV s^{-1}. Among them, the SE-Ni exhibits the smallest current response, probably due to a low loading amount of capacitive materials. Both SE-Mn and SE-NiMn demonstrate pronounced redox features, stemming from the characteristic of surface Mn-based pseudocapacitance. In comparison, the CV of SE-NiMn exhibits much bigger redox peak currents, indicating better redox activity and faster interfacial kinetics. The peak positions of SE-NiMn are influenced by the nickel component in the film, positioning between those of SE-Ni and SE-Mn. Specifically, the cathodic potentials of SE-Mn, SE-NiMn, and SE-Ni are 0.97 V, 1.02 V, and 1.03 V, respectively. Their related anodic potentials are 0.84 V, 0.79 V, and 0.76 V, respectively. In addition, SE-NiMn exhibits a delayed increase in current response near the potential

limits, suggesting a lower tendency toward water splitting (i.e., oxygen evolution reaction and hydrogen evolution reaction) and, consequently, a wider effective potential window.

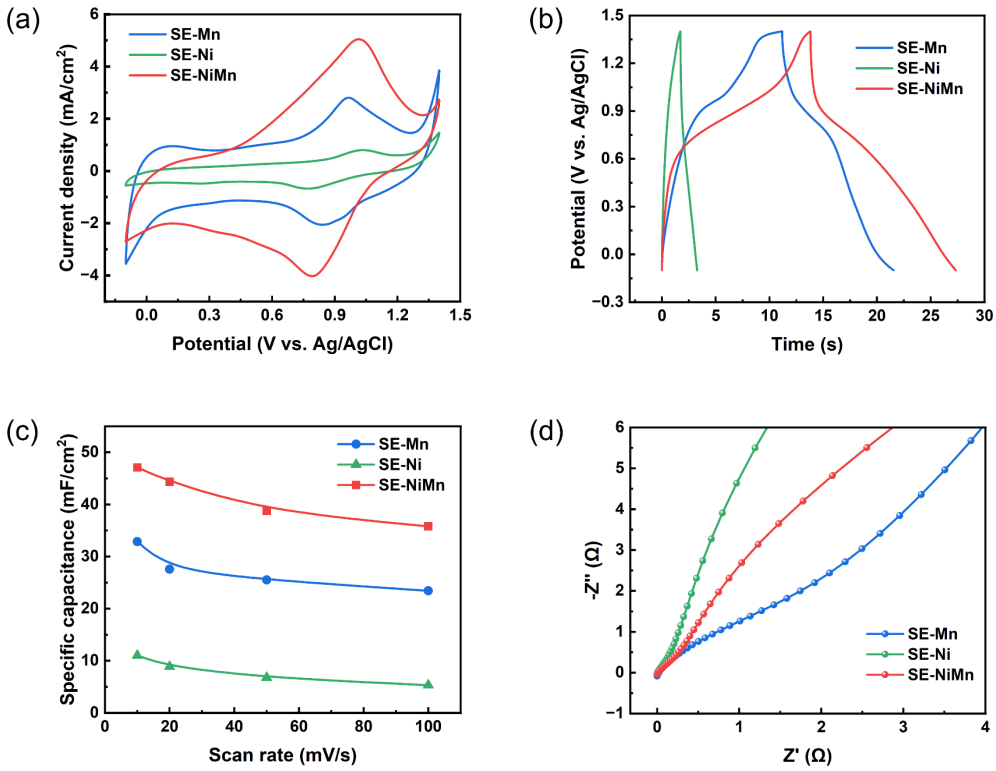


***Figure 4.5**. Comparison of electrochemical performance of SE-Mn, SE-Ni, and SE-NiMn in 1.0 M Na_2SO_4 aqueous solution: (a) CVs recorded in -0.1—1.4 V at a scan rate of 50 mV s^{-1}, (b) GCD curves measured at a current density of 3 mA cm^{-2}, (c) The variation of specific capacitances with scan rates, and (d) Nyquist plots.*

As shown in **Figure 4.5b**, the GCD curves measured at the current density of 3 mA cm^{-2} show that SE-NiMn has the longest charging-discharging time, indicating the highest specific capacitance. The specific capacitances of three electrodes calculated through CVs at different scan rates (e.g., from 10 mV s^{-1} to 100 mV s^{-1}) are presented in **Figure 4.5c**. SE-NiMn maintains the highest specific capacitance across all shown scan rates, demonstrating the superior charge transfer efficiency. The Nyquist plots (**Figure 4.5d**) show that the SE-Ni sample has the smallest semicircle in high-frequency region (i.e., the lowest R_{ct}). This response is expected for an ultrathin Ni oxide layer, which is supported

quantitatively by the deposition charge obtained from the *i-t* curves (**Figure 4.3**). Consequently, the EIS response of SE-Ni approaches that of bare CC substrate. Moreover, co-deposition of nickel with MnO_x (e.g., SE-NiMn) reduces the semicircle relative to SE-Mn in high-frequency region, indicating a lower R_{ct}. This is consistent with nickel incorporation enhancing the electronic conductivity of the mixed oxide and facilitating interfacial redox kinetics. In the low-frequency region, the Nyquist plots of SE-NiMn and SE-Mn show similar slopes, implying comparable Warburg-type diffusion impedance (i.e., similar ion transport limitations).

In summary, incorporating a nickel component during electrodeposition increases nucleation density and promotes the formation of a mixed $NiMnO_x$ film. The incorporation of Ni is providing mixed-valence redox couples (Ni^{3+}/Ni^{2+}) that enhance electronic conductivity and facilitate charge transport. Meanwhile, the synergistic mixed oxide framework helps stabilize the structure by mitigating Mn^{3+}-induced Jahn-Teller distortion and related degradation mechanisms, thereby improving cycling stability.[91] Along with improvement in Na^+ storage,[90] the $NiMnO_x$-coated CC (i.e., $NiMnO_x$@CC, SE-NiMn) exhibits a higher capacitance, a lower resistance, better rate capability, and enhanced pseudocapacitive behavior in comparison to MnO_x-coated CC (i.e., MnO_x@CC SE-Mn).

4.3 Characterization of $NiMnO_x$-coated carbon cloth

In addition to morphological characterization, EDX elemental mapping of $NiMnO_x$ films was carried out. As shown in **Figure 4.6**, there is the signal of O, Mn, and Ni elements. Homogeneous distribution of O, Mn, and Ni is also noticed. The O and Mn elemental maps exhibit nearly identical distributions. Their uniformly dispersed signals over the observed surface confirm the formation of a continuous and interconnected MnO_x structure. The Ni signal is weaker yet evenly distributed, consistent with an intentional low-level incorporation of Ni during deposition. There are no Ni-rich agglomerates or phase-segregated domains observed, indicating that Ni is well integrated

within the MnO_x matrix rather than forming separate particles. The elemental mapping confirms the formation of a homogeneous $NiMnO_x$ film, which aligns with the enhanced electrochemical performance observed in SE-NiMn.

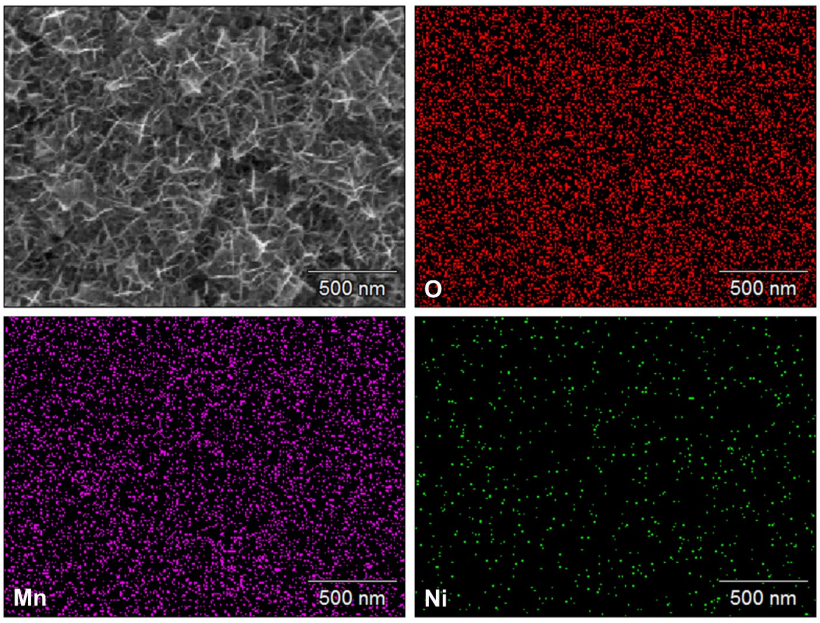


***Figure 4.6**. FESEM image (upper left) and corresponding EDX elemental mapping of oxygen (red), manganese (fuchsia), and nickel (green).*

The structural fingerprints of the $NiMnO_x$@CC electrode material were further characterized by means of Raman spectroscopy in the region of 150—1900 cm^{-1} (**Figure 4.7a**). The Raman spectrum of $NiMnO_x$@CC exhibits three strong peaks at 651 cm^{-1}, 1358 cm^{-1}, and 1582 cm^{-1}, along with a weak and broad band in the range of 280—400 cm^{-1}. The strong band centered at 651 cm^{-1} is assigned to the ν_2(Mn–O) symmetric stretching vibrations (A_{1g} mode) of MnO_6 octahedra, which is characteristic of birnessite-type MnO_x. Whereas the two weaker bands at 302 cm^{-1} and 356 cm^{-1}, as well as those appeared within the 280—400 cm^{-1} range, are associated with Mn–O bending vibrations.[146,147] The D band at 1358 cm^{-1} and the G band at 1582 cm^{-1} originate from the CC substrate, reflecting disordered carbon and ordered graphitic sp^2 carbon, respectively.

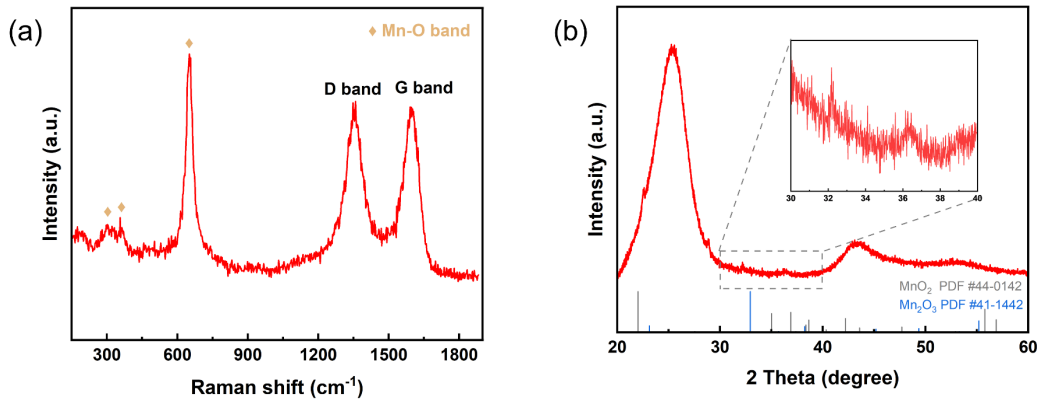


***Figure 4.7**. (a) Raman spectrum and (b) XRD patterns with an enlarged view of the NiMnO$_x$@CC.*

XRD was employed to investigate the crystalline structure of the NiMnO$_x$ film. The diffraction patterns (**Figure 4.7b**) are dominated by the CC substrate, showing the broad (002) reflection of graphitic carbon at 25.7 ° and a weak feature at 42.1 ° assignable to (100) plane. In addition to these substrate peaks, the NiMnO$_x$ film exhibits no sharp Bragg reflections. Only very low-intensity and broadened features are discernible at 22.5 ° and 36.7 °. These results indicate that the deposited NiMnO$_x$ film has poor crystallinity and a thin thickness. Such diffuse scattering is typical for electrodeposited Mn oxide films, where small coherent domain sizes, structural disorder, and lattice defects suppress long-range order.[148,149] Note that amorphous transition metal hydroxides are expected to possess better electrochemical performance because of more grain boundaries and ion diffusion channels.[92,150] The absence of clear Ni oxide diffraction features further indicates the presence of only trace amounts of Ni, likely existing as a solid solution within MnO$_x$. It also suggests a low degree of crystallinity, in agreement with the results from the EDX mapping (**Figure 4.6**) and the corresponding Raman spectrum (**Figure 4.7a**).

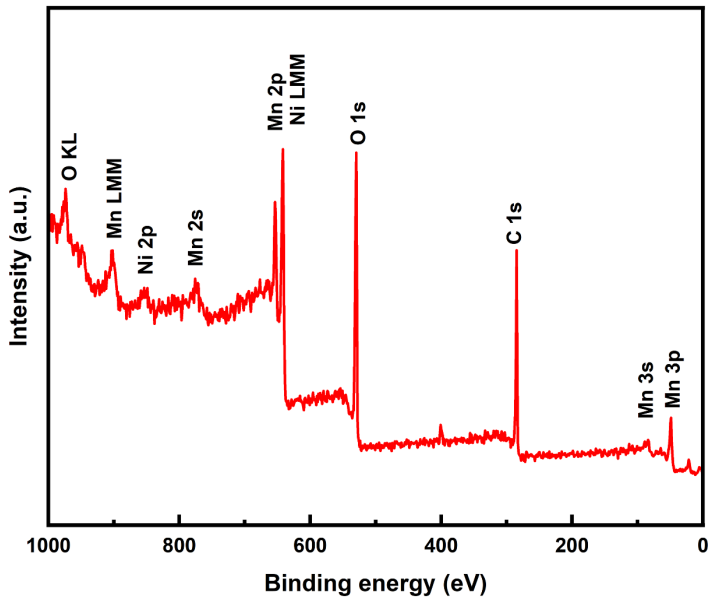


Figure 4.8. *XPS survey spectrum of the NiMnO$_x$@CC film.*

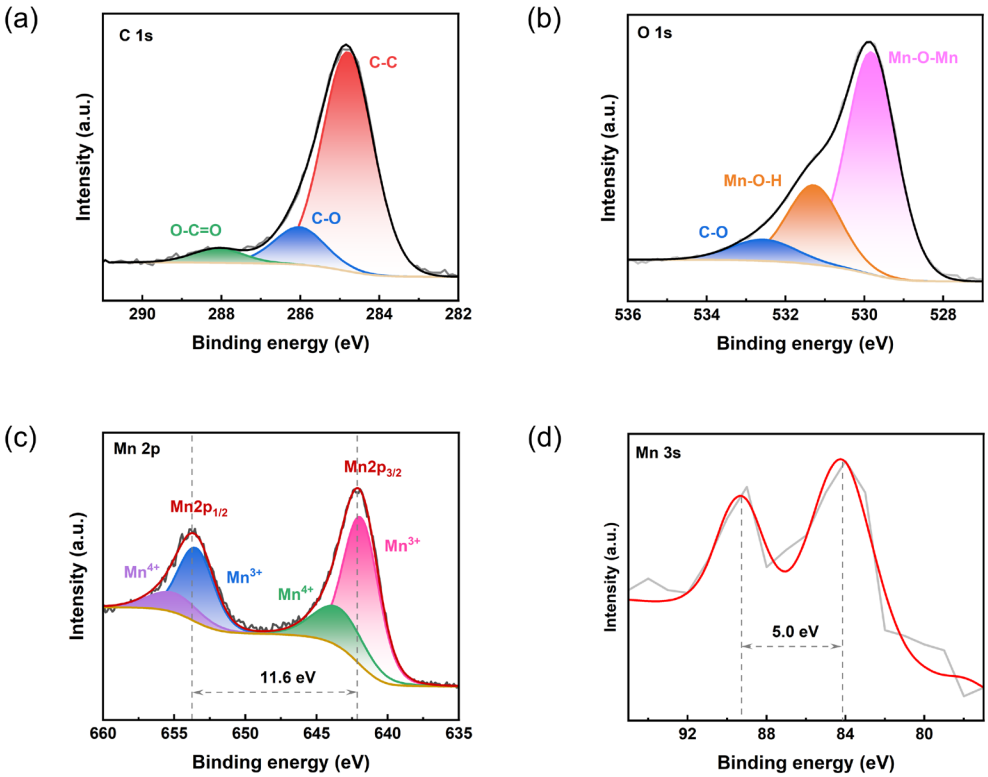


Figure 4.9. *High-resolution XPS spectra of (a) C 1s, (b) O 1s, (c) Mn 2p, and (d) Mn 3s of the NiMnO$_x$@CC electrode material.*

XPS measurements were conducted to further investigate the composition and the chemical bonding states of the synthesized $NiMnO_x$@CC film. The XPS survey spectrum (**Figure 4.8**) is dominated by Mn 2p (642.6/653.8 eV doublet), O 1s (539.8 eV), and C 1s (284.8 eV) signals, confirming a MnO_x film on the CC substrate. The strong C 1s peak (52.7 atom-%) is assigned to CC substrate. Additional Mn peaks (Mn LMN, Mn 2s, Mn 3s, and Mn 3p) are presented, further corroborating the manganese oxides. A weak Ni 2p hump is also discernible, consistent with the low-level incorporation of Ni and in agreement with the homogeneous, low-abundance Ni distribution seen in EDX mapping (**Figure 4.6**)

Figure 4.9 presents the high-resolution XPS spectra obtained for the investigation of the elemental bonding states of C, O, and Mn. Due to the low content of Ni, its high-resolution XPS fine scan spectra could not be recorded. The obtained C 1s spectrum (**Figure 4.9a**) has been fitted up into a dominant C–C component at 284.8 eV, together with C–O (~ 286.0 eV) and O–C=O (~ 288.1 eV) contributions that arise from mild electrochemical oxidation of the CC surface. From the fitted O 1s spectrum (**Figure 4.9b**) three chemically distinct oxygen species are identified: lattice oxygen Mn–O–Mn centered at 529.8 eV (dominant), Mn–OH bonding at 531.3 eV, and a high-BE shoulder at 532.6 eV that is attributed to C–O bonds. All these peaks are characteristic of Mn oxides film and further suggest a predominantly oxide phase.[78,151] The fitted Mn 2p spectrum (**Figure 4.9c**) displays a well-defined spin–orbit doublet at Mn $2p_{3/2}$ at 653.8 eV and Mn $2p_{1/2}$ at 642.2 eV with a peak separation of 11.6 eV, in good agreement with the reported values for Mn oxide phases.[152–155] It should be noticed that no satellite feature is observed at approximately 647 eV, which is typically associated with MnO films but absent in both Mn_2O_3 and MnO_2.[156] The Mn $2p_{3/2}$ peak has been fitted into two peaks at 641.9 eV and 643.4 eV, while the Mn $2p_{1/2}$ peak is deconvoluted into two peaks at 653.5 eV and 655.0 eV. They correspond to Mn^{3+} and Mn^{4+} oxidation states, respectively.[157] This deconvolution confirms that as-synthesized Mn oxide film exhibit a mixed-valence state, which is advantageous for enhancing electrochemical activity.[78,158] The Mn 3s spectrum (**Figure 4.9d**) shows two multiplet split components with a peak separation of

5.0 eV. It is possible to distinguish Mn oxidation states using Mn 3s peak as well. The average Mn oxidation state can be calculated by the equation:

$$Average\ valance\ state = 8.95 - 1.13 \times \Delta E \quad (4.1)$$

where ΔE refers to peak separation.[159] Therefore, the average oxidation valence state of Mn element in the $NiMnO_x$ film is 3.3+, consistent with the Mn^{4+}/Mn^{3+} ratio inferred from the Mn 2p spectrum fitting.

4.4 Performance of $NiMnO_x$-coated carbon cloth electrode

The electrochemical performance was thoroughly investigated in 1.0 M Na_2SO_4 aqueous solution using a three-electrode system. The potential range of -0.1—1.4 V (*vs.* Ag/AgCl) was applied to perform these measurements. **Figure 4.10** presents a summary of such performance using CV and GCD techniques.

The CVs (**Figure 4.10a**) exhibit rectangular-like profile with broad redox peaks, which is a characteristic feature of surface-controlled redox pseudocapacitive behavior for Mn-based oxides. The peak pair centered near 0.9—1.2 V is attributed to the reversible Mn^{4+}/Mn^{3+} (and, to a lesser extent, Ni^{3+}/Ni^{2+}) redox reaction, accompanied by charge-compensating Na^+ ion intercalation/deintercalation in the hydrated oxide lattice.[36,77,78,85,89,160,161] The specific reactions can be described as follows. (I) During charging process, some Mn^{3+} ions undergo oxidation and transform into Mn^{4+} ions, while Na^+ ions are simultaneously extracted from the Mn oxide lattice and the resulting vacant sites are occupied by H^+ ions (mediated by water molecules), leading to an ion exchange process.[162] (II) The discharging process reverses these steps. As the scan rate increases from 10 mV s^{-1} to 100 mV s^{-1}, the current response rises proportionally, and the CVs maintain their general shape, indicating fast charge transfer rate and the modest diffusion limitations in 1.0 M Na_2SO_4 aqueous electrolyte.

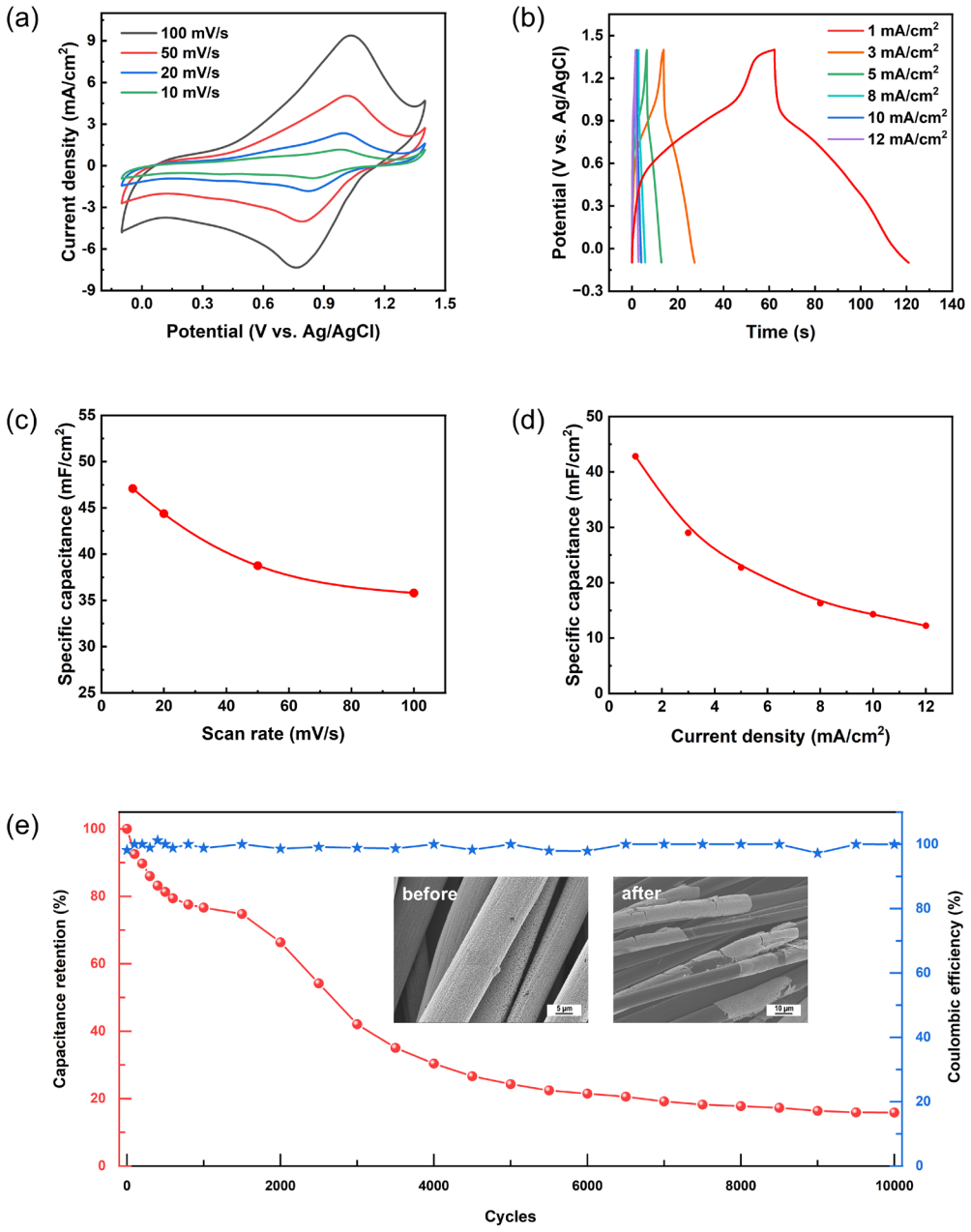


Figure 4.10. *Electrochemical performance of the NiMnO$_x$@CC electrode in 1.0 M Na$_2$SO$_4$ aqueous solution: (a) cyclic voltammograms at scan rates of 10, 20, 50, and 100 mV s^{-1}; (b) GCD curves at current densities of 1, 3, 5, 8, 10, and 12 mA cm^{-2}; (c) specific capacitances in relation to scan rates, and (d) specific capacitances in relation to current densities; (e) capacitance retention and coulombic efficiency during long time cycling at a current density of 12 mA cm^{-2}, the insets are the FESEM images of electrode before and after long-term cycling.*

Figure 4.10b shows the GCD curves of the $NiMnO_x$@CC electrode at different current densities ranging (e.g., from 1 mA cm^{-2} to 12 mA cm^{-2}). Non-linear GCD profiles with discernible plateaus further confirm a pseudocapacitive charge storage mechanism. The charging duration is almost equivalent to the discharging time, demonstrating the excellent reversibility of such a pseudocapacitive process.

The specific capacitances were calculated from both CVs and GCD curves. They are presented in **Figure 4.10c** and **Figure 4.10d**, respectively. Specifically, the specific capacitances calculated from the CVs are 47.1, 44.4, 38.8, and 35.8 mF cm^{-2} at the scan rates of 10, 20, 50, and 100 mV s^{-1}, respectively. The results indicate a good rate capability with 76 % retention when the scan rate increases ten-fold. Based on the GCD curves, the calculated specific capacitances are 42.8, 29.0, 22.7, 16.3, 14.3, and 12.2 mF cm^{-2} at the current densities of 1, 3, 5, 8, 10, and 12 mA cm^{-2}, respectively, reflecting the expected decline at higher current densities caused by shortened ion diffusion lengths and increased ohmic losses.

The long-term cycling stability of the $NiMnO_x$@CC electrode was evaluated by GCD technique at a high current density of 12 mA cm^{-2}. Both capacitance retention and coulombic efficiency were calculated, which are demonstrated in **Figure 4.10e**. The $NiMnO_x$@CC electrode maintains a consistently high coulombic efficiency (> 98.5 %) over 10,000 cycles, confirming the effective charge transfer processes and highly reversible redox reactions. In contrast, the capacitance undergoes a two-stage degradation behavior: it first drops rapidly to approximately 80 % within the initial hundreds of cycles, followed by a short quasi-steady plateau; thereafter, the second dramatic decrease begins at around 1,500 cycles, which transitions into a more gradual, near-linear decline to below 20 % retention after 10,000 cycles. It has to point out that the rapid initial capacitance fading is commonly observed in manganese oxide-based electrodes.[85,163,164] It has been attributed to (i) structural instability under applied potential, leading to removal of loosely bound surface materials, (ii) partial disproportionation of Mn^{3+} to soluble Mn^{2+} in neutral electrolyte (again leading to gradual mass loss), and (iii) a high mechanical stress caused by ion intercalation/deintercalation processes, reducing the structural stability of $NiMnO_x$

film. After approximately 1,500 cycles, the capacitance undergoes a second abrupt degradation. This result is probably associated with the electrochemical oxidation of the surface sp^2 carbon on CFs, which damages the original surface structure and significantly increases the surface roughness.[165] As a consequence, the oxide film loses interfacial adhesion to the CC substrate surface. Such an assumption is further supported by the FESEM images in **Figure 4.10e**, where the $NiMnO_x$ film fragments and is detached from the CC substrate after a number of charging-discharging cycles.

4.5 Conclusions

Two synthesis approaches, hydrothermal synthesis and cathodic electrodeposition, have been explored to grow pseudocapacitive materials of manganese oxides on the CC substrate to prepare high-performance electrodes. In comparison to hydrothermal synthesis, electrodeposition method offers several decisive advantages, including good controllability of conformality and thickness, effective substrate protection, high reproducibility, and strong adhesion between film and substrate. In addition, the synthesized sample through electrodeposition exhibits better electrochemical performance with higher current response, a larger specific capacitance (25.51 mF cm^{-2} at 50 mV s^{-1}), a wider available potential range (-0.1—1.4 V), and better defined redox peaks characteristic of fast surface redox reactions.

Incorporating a trace amount of nickel component during electrodeposition can facilitate the formation of a $NiMnO_x$ film, thereby enhancing both reaction kinetics and charge storage capacity. The optimized $NiMnO_x$@CC electrode exhibits high specific capacitances, good rate capability, and excellent coulombic efficiency. For example, high specific capacitances of 47.1 mF cm^{-2} at the scan rate of 10 mV s^{-1} and 42.8 mF cm^{-2} at the current density of 1 mA cm^{-2} have been obtained. During long-term cycling, the electrode keeps a high coulombic efficiency over 98.5 % over 10,000 cycles at the current density of 12 mA cm^{-2}. These results are consistent with the role of Ni in promoting electronic conductivity and providing additional, complementary redox couples that

contribute to an enhanced pseudocapacitive performance.

Despite these advantages, long-term cycling stability remains a critical challenge. Only less than 20 % of its initial capacitance is preserved after 10,000 charging-discharging cycles. The corresponding FESEM images reveal the loss of interfacial adhesion between the oxide films and CF surface. From the perspective of electrode design, it is theoretically feasible to enhance durability by replacing the sp^2 carbon substrate with a sp^3 carbon substrate, which could maintain stronger interfacial adhesion between the $NiMnO_x$ film and the substrate.

5 $NiMnO_x$-Coated Diamond Cloth

The development of flexible supercapacitors requires electrode materials capable of simultaneously delivering high energy density, long-term cycling stability, and mechanical robustness. In the previous chapters, two electrode systems based on CC substrates have been discussed. Both electrodes demonstrate enhanced electrochemical performance but still possess their own distinct limitations. While the DC (i.e., boron-doped diamond coated CC) electrode discussed in Chapter 3 demonstrates exceptional mechanical flexibility and outstanding cycling stability, its capacitance is inherently limited by the purely electrostatic electric double-layer mechanism. In contrast, $NiMnO_x$@CC detailed in Chapter 4 exhibits significantly higher capacitance through fast, reversible Faradaic reactions, yet it frequently suffers from structural degradation, interfacial delamination, and capacitance fading during prolonged cycling.

To reconcile these complementary limitations, this chapter introduces an integrated materials design that combines the strengths of both systems. The strategy involves the conformal electrodeposition of a $NiMnO_x$ film onto the robust DC substrate, creating a composite $NiMnO_x$@DC electrode. In this architecture, the DC substrate serves as an electrochemically inert and mechanically stable electrode platform, engineered to withstand electrochemical oxidation and mechanical stress associated with pseudocapacitive cycling. Concurrently, the adhered $NiMnO_x$ film provides a high capacitance *via* fast and reversible Faradaic reactions.

This chapter systematically investigates the fabrication, optimization, characterization, and electrochemical performance of the $NiMnO_x$@DC electrode material. It begins by directly comparing the electrochemical performance of $NiMnO_x$@DC with that of $NiMnO_x$@CC to isolate and elucidate the critical role of the DC substrate. A key electrodeposition parameter (e.g., the deposition potential) is optimized to achieve a uniform and adherent $NiMnO_x$ film. Electrochemical evaluations are carried out in both three-electrode and two-electrode configurations, quantifying capacitance, rate capability, cycling stability, energy density, and power density. Finally, the mechanical flexibility of

the $NiMnO_x$@DC electrode is examined under different bending conditions to validate the practical suitability for flexible SC applications.

5.1 Substrate-dependent performance of $NiMnO_x$

To investigate the influence of substrate materials on electrochemical performance of $NiMnO_x$ capacitive films, they were fabricated on both CC substrate and DC substrate under identical electrodeposition conditions. The $NiMnO_x$ films were electrochemically deposited at a constant potential of 0.9 V (*vs.* Ag/AgCl) in an aqueous solution containing 50 mM $MnSO_4$ and 3 mM $Ni(CH_3COO)_2$. The fabricated electrodes are denoted $NiMnO_x$@CC and $NiMnO_x$@DC-0.9, respectively.

Figure 5.1 compares electrochemical behaviors of $NiMnO_x$@CC and $NiMnO_x$@DC-0.9 electrodes in 1.0 M Na_2SO_4 aqueous solution. The CVs recorded at a scan rate of 50 mV s^{-1} (**Figure 5.1a**) reveal distinct differences in electrochemical activity between the two electrodes. The $NiMnO_x$@DC-0.9 electrode exhibits a higher response current, more pronounced redox peaks, and a larger enclosed area compared to $NiMnO_x$@CC, indicating enhanced pseudocapacitive performance. The GCD curves obtained at the current density of 3 mA cm^{-2} (**Figure 5.1b**) further demonstrate the effect of a substrate on electrochemical performance of the two electrodes. The $NiMnO_x$@DC-0.9 electrode shows significantly longer charging and discharging times and more symmetric charging-discharging curves compared to $NiMnO_x$@CC, indicating its superior charge storage capacity and better reversibility. The potential plateau observed in both electrodes verifies that their energy storage mechanism is predominantly pseudocapacitive in nature. The specific capacitances of the $NiMnO_x$@DC-0.9 electrode, calculated from both the CVs and GCD curves, are approximately twice those of $NiMnO_x$@CC. Furthermore, their EIS analysis (**Figure 5.1c**) provides insights into the charge transfer kinetics and ion diffusion processes. The Nyquist plots show that both electrodes exhibit relatively small semicircles in the high-frequency region, indicating fast interfacial charge transfer rates. However, the $NiMnO_x$@DC-0.9 electrode exhibits a smaller slope in the low-frequency

region, suggesting the formation of a denser oxide film and consequently increased ion diffusion impedance. This behavior is consistent with the larger specific capacitance derived from CV and GCD measurements. The enhanced electrochemical performance can be primarily attributed to improved interfacial electrical contact and more efficient utilization of the active material.

The enhanced performance of NiMnO$_x$@DC-0.9 can be attributed to improved adhesion between the active material and BDD surface, facilitating more efficient electron transfer, and optimized pore structure that promotes electrolyte penetration and ion transport. The superior performance preliminarily demonstrates that DC can serve as a more effective electrode support for pseudocapacitive NiMnO$_x$ films.

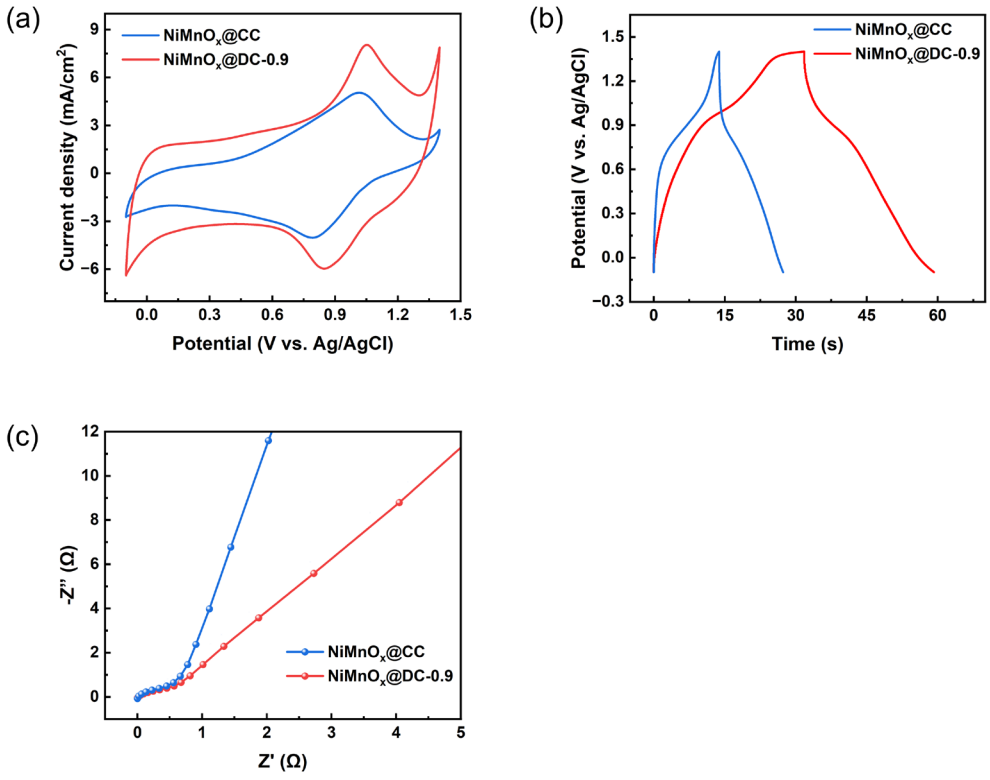


Figure 5.1. *Electrochemical performance of NiMnO$_x$@CC electrode and NiMnO$_x$@DC-0.9 electrode in 1.0 M Na_2SO_4 electrolyte: (a) CVs recorded at the scan rate of 50 mV s^{-1}, (b) GCD curves measured at the current density of 3 mA cm^{-2}, and (c) Nyquist plots.*

5.2 Influence of deposition potential

The $NiMnO_x$ films were electrochemically deposited on DC in a mixed $MnSO_4$ and $Ni(CH_3COO)_2$ electrolyte at three different constant electrodeposition potentials: 0.9, 1.0, and 1.1 V (*vs.* Ag/AgCl). The fabricated electrode materials are denoted $NiMnO_x$@DC-0.9, $NiMnO_x$@DC-1.0, and $NiMnO_x$@DC-1.1, respectively. **Figure 5.2** presents the *i-t* curves for a deposition time of 1500 s. All curves exhibit a very high current in the first few seconds (that is due to double-layer formation and nucleation), followed by a quasi-steady-state (that is limited by mass transport). After approximately 200 s, the steady-state current increases with applied potential, measuring 0.22 mA at 0.9 V, 0.66 mA at 1.0 V, and 1.49 mA at 1.1 V. A high potential provides a greater thermodynamic driving force for the electrochemical oxidation reaction. The potential directly affects the nucleation and growth rates of $NiMnO_x$, thereby influencing the final film microstructure and thickness.[166]

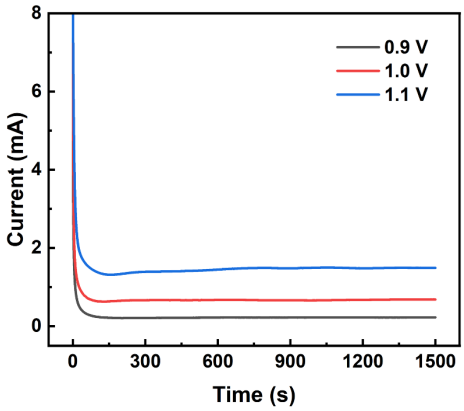


***Figure 5.2**. I-t curves of electrodeposition for $NiMnO_x$ films under three constant potentials of 0.9, 1.0, and 1.1 V (vs. Ag/AgCl) for 1500 s.*

The FESEM images of these films were recorded (**Figure 5.3**). They reveal distinct morphological differences among the electrode materials electrodeposited at three different potentials. They are further compared after their 10,000 charging-discharging cycles in 1.0 M Na_2SO_4 aqueous electrolyte. In this way, crucial insights into the

relationship between deposition conditions and film structure can be provided. For $NiMnO_x$@DC-0.9 (**Figure 5.3a**), DC fibers are fully coated with a relatively smooth and uniform $NiMnO_x$ film, exhibiting a good conformal coverage. This is because a low potential or a slow deposition rate can result in more controlled nucleation and growth, leading to the formation of smaller particles and a more compact film structure. As-synthesized $NiMnO_x$@DC-1.0 (**Figure 5.3c**) exhibits a highly porous, flower-like morphology with interconnected nanostructures. The porous architecture provides abundant active sites and facilitates efficient electrolyte penetration. At the deposition potential of 1.1 V, DC is coated with a coarser, and more aggregated film structure (**Figure 5.3e**). It is assumed that a higher potential, namely a fast deposition rate, leads to rapid and less controlled film formation, resulting in non-uniform coverage. In addition, a high current density at the deposition potential of 1.1 V may induce side reactions (e.g., oxygen evolution reaction), which can further improve the film porosity and weaken interfacial adhesion. This explanation is supported by the FESEM images obtained after long-term cycling (**Figure 5.3f**). $NiMnO_x$@DC-1.1 exhibits more pronounced changes in its morphology after a prolonged operation. Discernible cracking and potential flake detachment are observed, consistent with stress accumulation during the charging-discharging cycles and weak interfacial adhesion. In the case of $NiMnO_x$@DC-0.9, the $NiMnO_x$ film is largely absent and the underlying BDD film is almost exposed after such a cycling test (**Figure 5.3b**). These facets remain sharp and the granular texture of the BDD film is essentially unchanged. This suggests that the oxide film deposited at 0.9 V was relatively thin, consistent with the low steady-state current recorded by *i-t* curve. The DC substrate demonstrates high electrochemical stability. Small residual patches of oxide that cling to the BDD surface indicate the good interfacial adhesion between $NiMnO_x$ and BDD film. Furthermore, this phenomenon suggests that the oxide film undergoes progressive and uniform recession on the DC substrate during prolonged cycling, in contrast to fragmentary detachment observed on the CC substrate. The contrast underscores the chemical inertness, a wide potential window, and corrosion resistance of the sp^3 carbon electrode support compared to the sp^2 carbon electrode support, which is more susceptible to electrochemical oxidation.[165,167] After 10,000 cycles, $NiMnO_x$@DC-

1.0 retains much of its original nanosheet network structure (**Figure 5.3d**). The open and mesh-like architecture remains continuous across the surface of DC fibers in the inset, with no discernible cracking, flaking, or exposure of bare substrate. This morphological analysis strongly supports that a potential of 1.0 V presents the optimal electrodeposition potential, which offers a balance between reasonable deposition rate, more controlled film formation, and reduced side reactions.

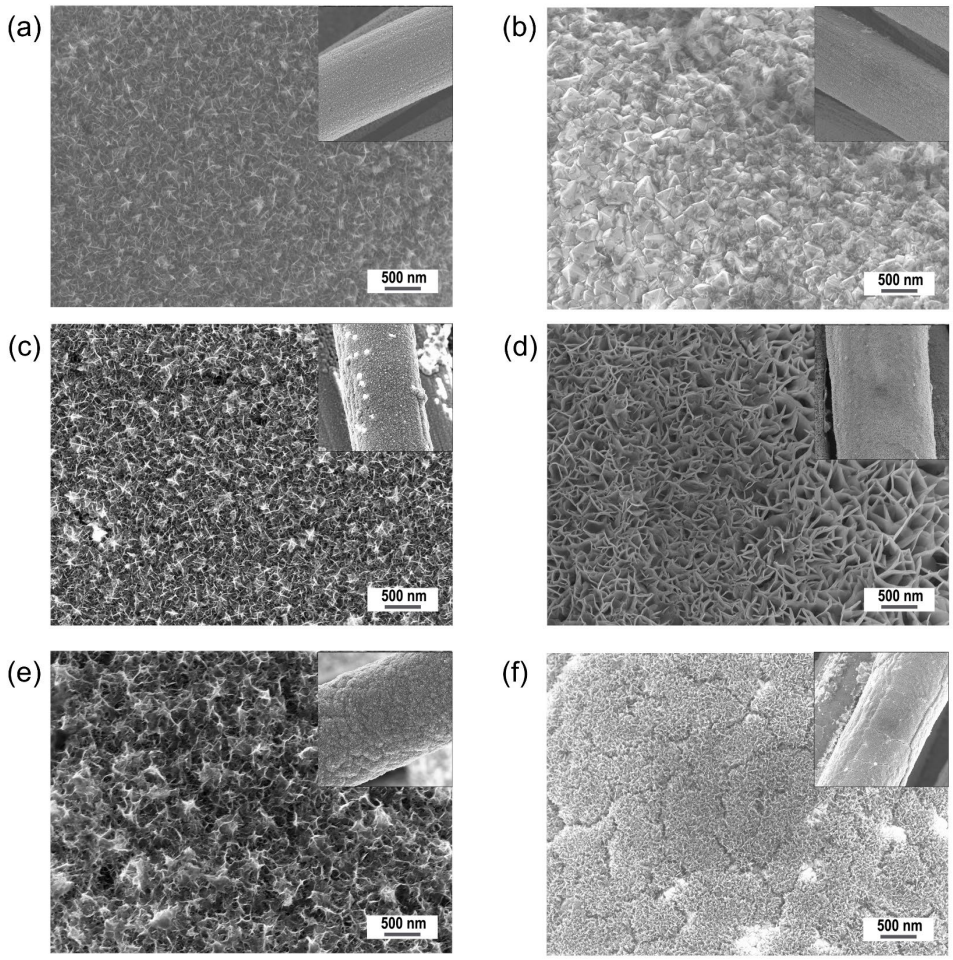


***Figure 5.3**. FESEM images of (a), (b) $NiMnO_x$@DC-0.9, (c), (d) $NiMnO_x$@DC-1.0, and (e), (f) $NiMnO_x$@DC-1.1. Images (a), (c), and (e) show the as-deposited material, while images (b), (d), and (f) show the materials after 10,000 charging-discharging cycles. The insets are the low-magnification FESEM images.*

Furthermore, Raman spectroscopy, XRD, and XPS analyses were carried out to clarify

the influence of deposition potential on the structural and chemical compositions of the as-prepared NiMnO$_x$@DC materials. **Figure 5.4** presents the Raman spectra and XRD patterns of NiMnO$_x$@DC electrodes prepared at different deposition potentials. The NiMnO$_x$ film deposited on DC demonstrates structural similarities to that formed on CC. The Raman spectra reveal distinct vibrational modes characteristic of manganese oxide phases (**Figure 5.4a**). All three electrode materials exhibit a prominent band centered near 650 cm^{-1}, which is assigned to the symmetric stretching vibrations of v_2(Mn–O) within the MnO_6 octahedra. The peak is characteristic of birnessite-type Mn oxide structure. Broad, low-intensity features observed in the range of 280—400 cm^{-1} can be attributed to the Mn–O bending vibrations. All these broad features indicate the as-prepared oxide film is generally amorphous and has a poor crystalline structure. This is actually a common outcome of the materials synthesized by means of electrodeposition. Notably, distinct Ni–O signatures are not observed, which is consistent with the low Ni content and suggests either intimate mixing or solid solution formation. By comparison, the dominant peak becomes slightly sharper for the NiMnO$_x$@DC-1.0 and NiMnO$_x$@DC-1.1, suggesting a modest improvement in short-range ordering of the MnO_6 network relative to the thin film grown at 0.9 V.

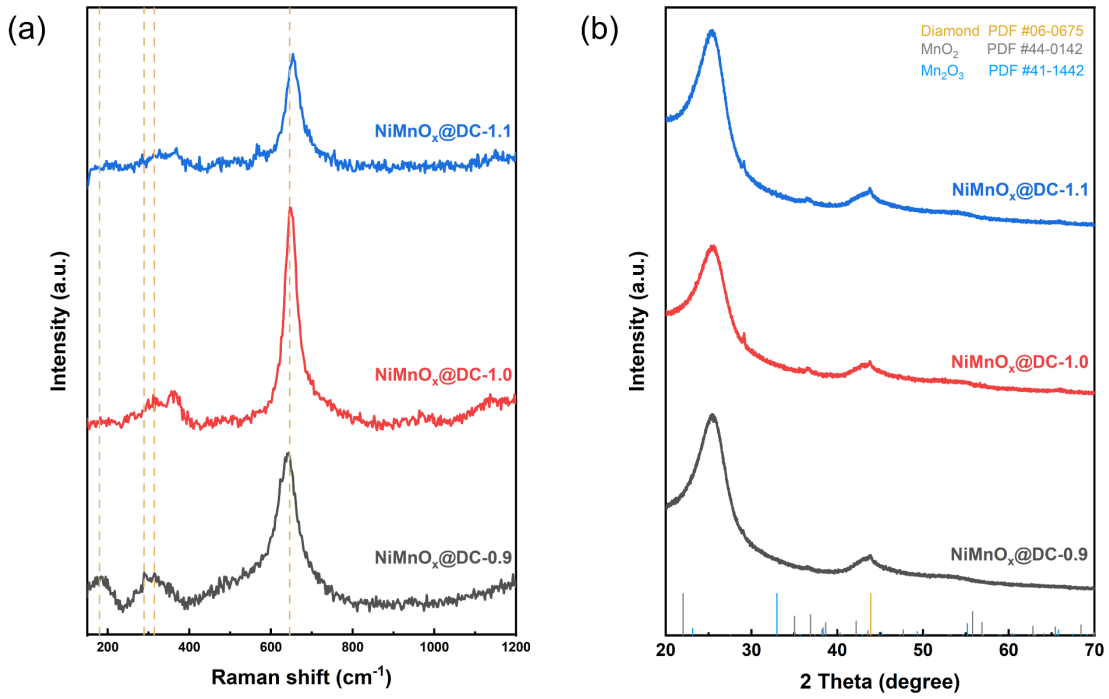


***Figure 5.4**. (a) Raman spectra and (b) XRD patterns of $NiMnO_x$@DC electrode materials.*

XRD patterns (**Figure 5.4b**) further confirm the largely amorphous or poorly crystalline nature of these oxide films. All patterns are dominated by broad, low-intensity humps without resolvable Bragg reflections from well crystalline Mn oxides. The discernible weak peak at approximately 36 ° and the small shoulder at around 55 ° become slightly more pronounced as applied deposition potential increases from 0.9 V to 1.0 V and 1.1V. They suggest the formation of slightly larger crystallite domains. The distinct diffraction peak corresponding to the (111) plane of the BDD film (as shown in **Figure 3.7a**) at 43.9 ° becomes significantly weaker. It is due to the attenuation caused by the conformal oxide film deposition, as expected. Overall, the Raman spectra and XRD patterns of three $NiMnO_x$@DC materials deliver highly similar conclusions to each other, demonstrating that the variation in electrodeposition potentials has a relatively minor effect on the phase composition and crystal structure of as-prepared $NiMnO_x$ film.

The XPS survey spectra of three $NiMnO_x$@DC electrode materials deposited at different potentials (i.e., 0.9, 1.0, and 1.1 V (*vs.* Ag/AgCl)) are presented in **Figure 5.5**. They provide a comprehensive overview of the elemental composition and chemical states present in the electrodeposited films. All three electrode materials exhibit clear identification of Mn, Ni, O, and C elemental peaks. Distinct Mn features are observed at Mn 2p (642/654 eV doublet), Mn 2s (771 eV), Mn 3s (86 eV) and Mn 3p (49 eV); while a strong O 1s peak is located at about 530 eV. These observations clearly confirm the formation of Mn oxides. In addition, a weak Ni 2p envelope centered at approximately 855 eV is discernible, indicating successful incorporation of Ni into the mixed oxides. The XPS survey also provides an analysis of semi-quantification. The atomic percentages of Mn in $NiMnO_x$@DC-0.9, $NiMnO_x$@DC-1.0, and $NiMnO_x$@DC-1.1 are approximately 7.8 %, 12.5 %, and 10.0 %, respectively. The oxygen contents in the corresponding samples are 33.6 %, 51.61 %, and 42.32 %, respectively. For $NiMnO_x$@DC-1.0, the highest content of Mn and O (in atomic percentage), along with the strongest attenuation of the substrate C 1s peak, indicate that the deposition potential

of 1.0 V achieves the optimal balance between electrochemical driving force and current efficiency. These results also confirm that a higher potential of 1.1 V promotes side reactions, which reduces the current efficiency for Mn oxide deposition and leads to the formation of more porous structures.[168]

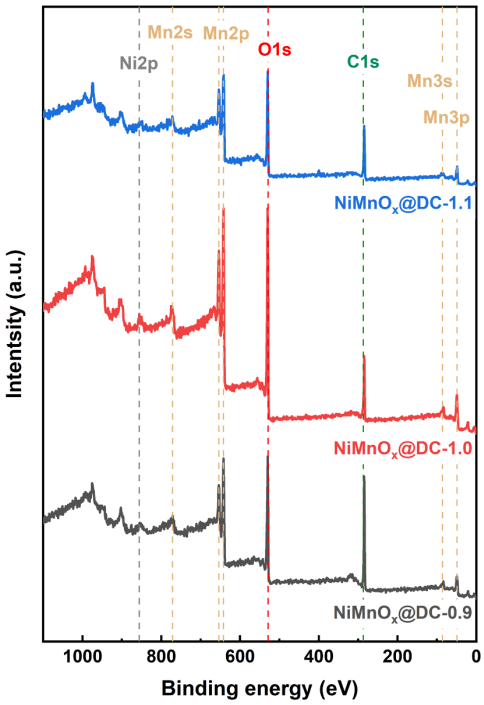


***Figure 5.5**. XPS survey spectra for NiMnO$_x$@DC electrode materials deposited at three different potentials.*

Furthermore, high-resolution XPS spectra of the Mn 2s and Mn 2P peaks were analyzed to elucidate the influence of deposition potential on chemical states and oxidation environments of Mn of NiMnO$_x$@DC electrodes (**Figure 5.6**). All electrodes display the characteristic two multiplet split components of Mn 3s with a peak separation of 4.8—5.0 eV (**Figure 5.6a**). This is diagnostic of mixed Mn^{4+}/Mn^{3+} oxidation states, typical of birnessite-type MnO_x structures. The peak separation increases as the deposition potential rises from 0.9 to 1.1 V, indicating an decrease in the average oxidation state of the Mn element.[159] The high-resolution Mn 2p spectra (**Figure 5.6b**) provide complementary information through detailed peak fitting analysis that deconvolutes the contributions

from different manganese oxidation states. The Mn 2p spectra exhibit the expected spin-orbit doublet ($2p_{3/2}$ and $2p_{1/2}$) with a separation of 11.6 eV. Across all three deposition potentials, peak fitting analysis reveals that Mn^{3+} constitutes the major component, with Mn^{4+} making a secondary contribution. This mixed valence nature is particularly advantageous for aqueous SC applications, where the reversible redox transitions between Mn^{4+} and Mn^{3+} states can provide high specific capacitance while maintaining structural stability. According to estimation from the fitting results, the Mn^{4+}/Mn^{3+} ratio of the NiMnO$_x$@DC-1.0 electrode is comparable to that of the NiMnO$_x$@DC-1.1 electrode, but higher than that of NiMnO$_x$@DC-0.9. This ratio is expected to correlate with electrochemical performance.[157,169]

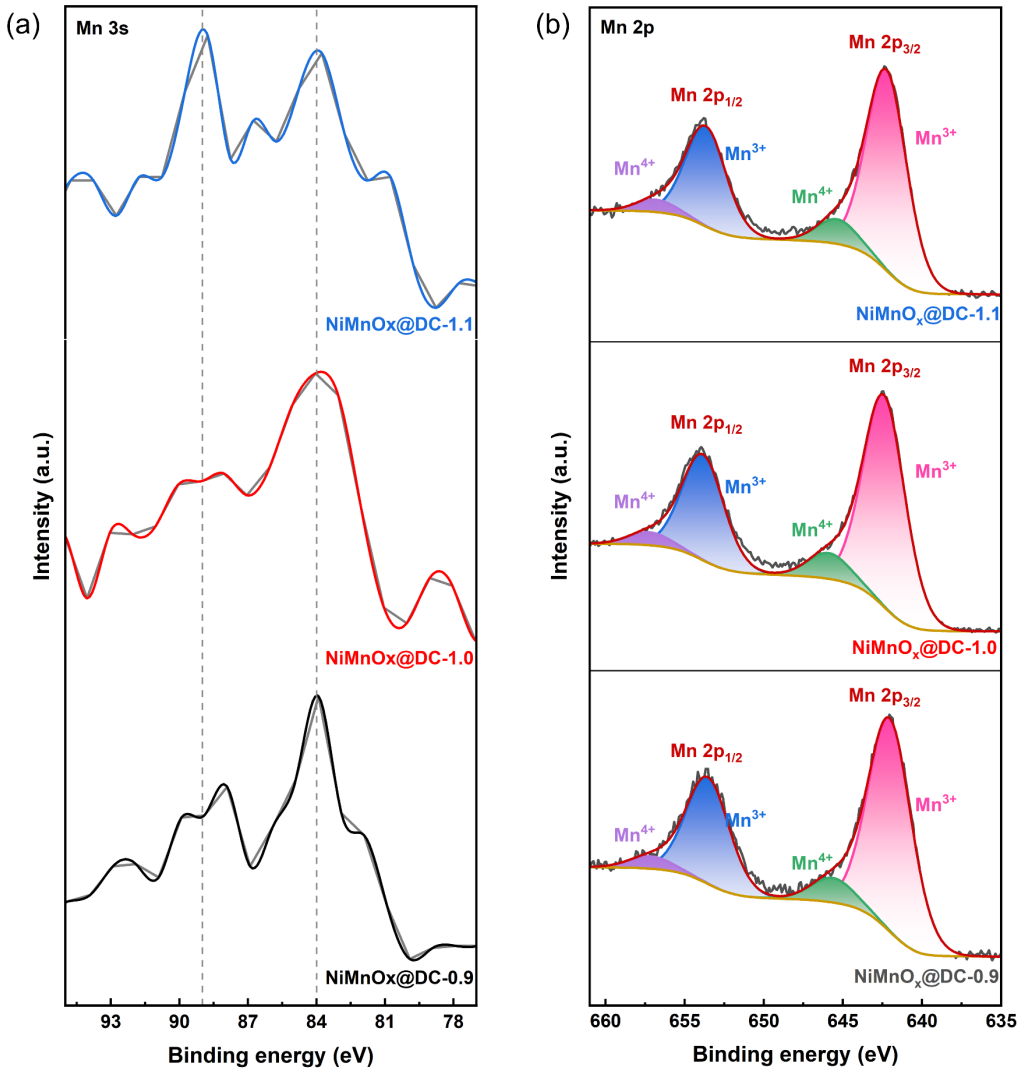


***Figure5.6**. High-resolution XPS spectra of (a) the Mn 3s orbital and (b) the Mn 2p orbital*

with fine fittings for the NiMnO$_x$@DC electrode materials.

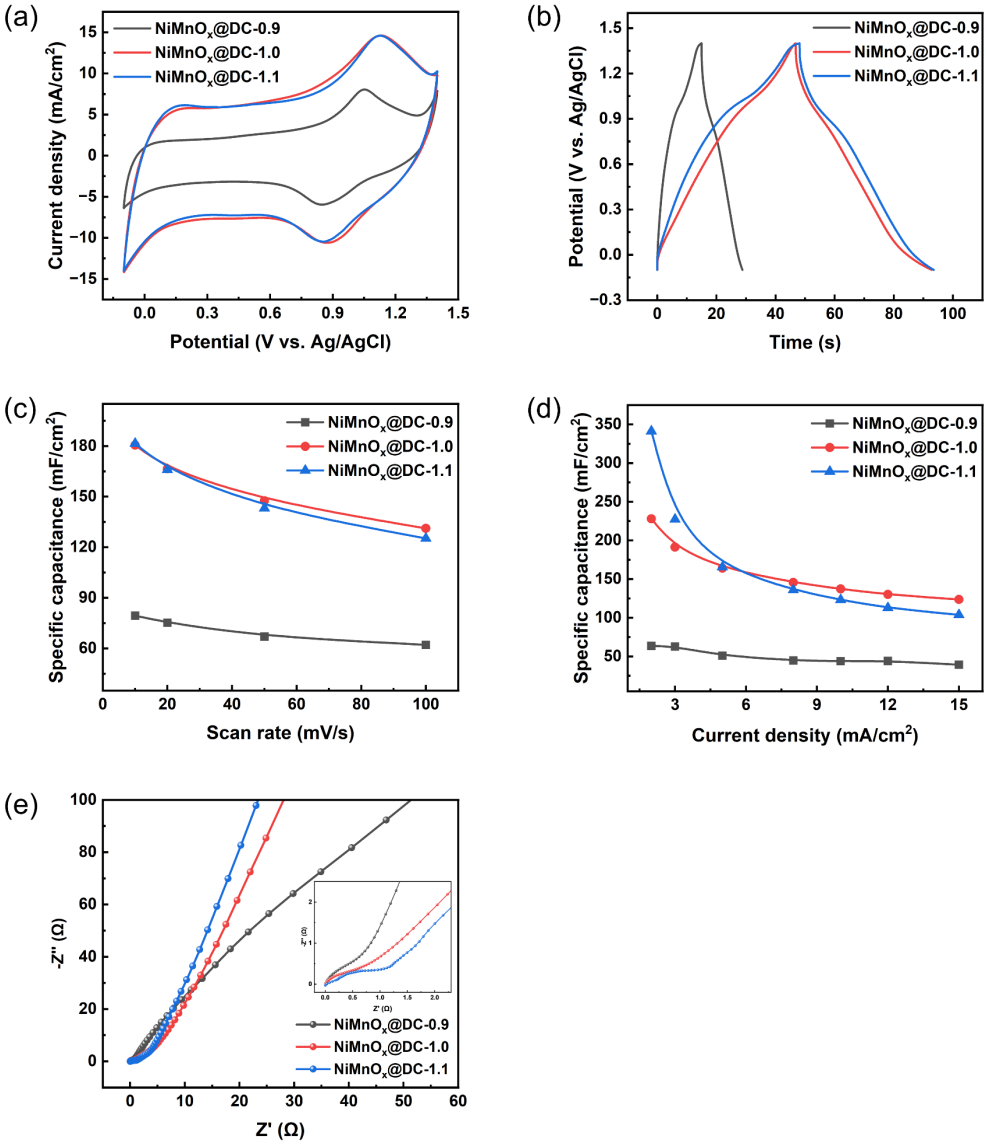


Figure 5.7*. Comparison of the electrochemical performance of NiMnO$_x$@DC electrodes measured in 1.0 M Na$_2$SO$_4$ aqueous electrolyte: (a) CVs measured at a scan rate of 50 mV s^{-1}, (b) GCD curves recorded at a current density of 5 mA cm^{-2}, the specific capacitances as a function of (c) scan rate and (d) current density, and (e) Nyquist plots with a magnified view inset.*

A comprehensive electrochemical characterization of three NiMnO$_x$@DC electrodes

was investigated in 1.0 M Na_2SO_4 aqueous solution using a three-electrode configuration. The comparison of the performance is presented in **Figure 5.7**. All three electrodes exhibit similar potential windows (-0.1—1.4 V *vs.* Ag/AgCl) and display a couple of well-defined redox current peaks, suggesting similar energy storage mechanism through fast surface Faradaic reactions (**Figure 5.7a**). The $NiMnO_x$@DC-1.0 and $NiMnO_x$@DC-1.1 electrodes show comparable enclosed areas, which are significantly larger than that of $NiMnO_x$@DC-0.9, demonstrating a higher capacitance. As shown in **Figure 5.7b**, all GCD curves measured at a current density of 5 mA cm^{-2} display quasi-triangular profiles with mild potential plateaus, confirming pseudocapacitive contributions. The discharging time again follows the order of 1.1 V ≈ 1.0 V > 0.9 V. The $NiMnO_x$@DC-0.9 electrode shows an evidently shortened discharging rate/time, consistent with its features of a thinner film and limited active mass. Regarding rate performance, the specific capacitance decreases with increasing scan rate for all electrodes (as shown in **Figure 5.7c**), which is typical behavior arising from ion diffusion limitations. All three electrodes demonstrate commendable rate capability. As an example, the $NiMnO_x$@DC-1.0 electrode maintains a high specific capacitance of 131.2 mF cm^{-2} at 100 mV s^{-1}, which corresponds to 73 % of the specific capacitance (180.5 mF cm^{-2}) measured at a low scan rate of 10 mV s^{-1}. Similar trends are observed with current density variation (**Figure 5.7d**). Again, the $NiMnO_x$@DC-1.0 electrode delivers high specific capacitances across various current densities while simultaneously exhibiting good rate capability. The Nyquist plots of three electrodes (**Figure 5.7e**) were further recorded in a frequency ranging from 0.01 to 10 kHz. The EIS curves exhibit a quasi-semicircle shape within the high-frequency range, indicating that the electrode reaction kinetics are primarily governed by the charge transfer process. In comparison, the $NiMnO_x$@DC-1.0 electrode has a smaller semicircle, evidencing the lower charge transfer resistance.[170,171] In the linear regions at low frequencies, the Nyquist plots of the $NiMnO_x$@DC-1.0 and the $NiMnO_x$@DC-1.1 electrodes exhibit nearly parallel straight lines that are steeper than that of the $NiMnO_x$@DC-0.9 electrode, indicating an improved ion diffusion process.

In combination with the characterization results from SEM, Raman, XRD, XPS, and

electrochemical measurements, the deposition potential of 1.0 V is optimal for the formation of a uniform and well-adherent $NiMnO_x$ film that is conformal to DC. The fabricated $NiMnO_x$@DC-1.0 electrode contributes to superior overall electrochemical performance, including a high areal capacitance, good rate performance, and a low charge transfer resistance. In the following sections, $NiMnO_x$@DC specifically refers to the electrode material prepared by electrodeposition at a potential of 1.0 V. It was taken as the optimized electrode material for detailed electrochemical measurements.

5.3 Pseudocapacitive performance of $NiMnO_x$-coated diamond cloth

In this section, the comprehensive electrochemical performance of $NiMnO_x$@DC was systematically investigated. The pseudocapacitive performance was evaluated in both a three-electrode system and in a two-electrode system. Subsequently, the energy density and power density of assembled devices were calculated and assessed. This progression establishes a direct connection between materials design and device-level performance, elucidating how the DC electrode support and $NiMnO_x$ pseudocapacitive material jointly contribute to the realization of stable and high-performance SCs.

5.3.1 Pseudocapacitive performance using a three-electrode system

The electrochemical performance of the $NiMnO_x$@DC electrode as a working electrode was initially evaluated using a three-electrode configuration in 1.0 M Na_2SO_4 aqueous electrolyte. The measurement results are detailed in **Figure 5.8**.

Figure 5.8a shows the CVs of $NiMnO_x$@DC at different scan rates (10, 20, 50, and 100 mV s^{-1}) within a wide potential window of -0.1—1.4 V (*vs.* Ag/AgCl). All curves exhibit nearly rectangular shapes with distinct redox peaks, indicating the coexistence of electric double-layer capacitance and Faradaic pseudocapacitance contributions. The latter originates from the reversible redox reactions of Ni^{3+}/Ni^{2+} and Mn^{4+}/Mn^{3+} couples.[77,85,125,172] As the scan rate increases, the curves retain their overall shape, with the current density scaling up proportionally. These results indicate fast electron transfer

kinetics and effective electrolyte access to the active sites. Good rate capability and a low internal resistance of the oxide/BDD interface is then expected. The calculated specific capacitances of this electrode are 180.5, 166.5, 147.6, and 131.2 mF cm^{-2} at the scan rates of 10, 20, 50, and 100 mV s^{-1}, respectively.

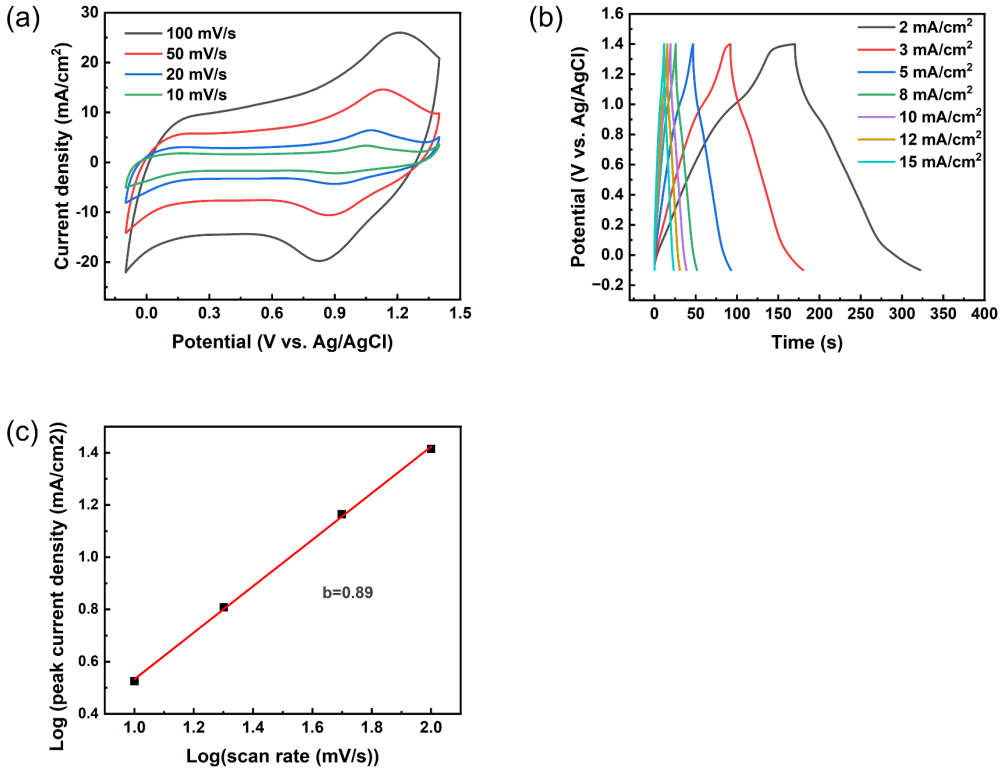


***Figure 5.8**. Electrochemical performance of NiMnO$_x$@DC electrode in 1.0 M Na$_2$SO$_4$ aqueous solution: (a) CVs at the scan rates of 10, 20, 50, and 100 mV s^{-1}, (b) GCD curves at the current densities ranging from 2 to15 mA cm^{-2}, and (c) relationship between logarithm peak current densities and logarithm scan rates.*

The GCD curves of this capacitor electrode are presented in **Figure 5.8b**. The curves were recorded at various current densities (e.g., ranging from 2 to 15 mA cm^{-2}). The GCD profiles exhibit characteristic features of pseudocapacitive behavior, with distinct potential plateaus corresponding to the redox reactions observed in the CVs. In addition, the nearly symmetrical charging and discharging times indicate a high degree of reversibility in the redox reactions. The estimated specific capacitances from the GCD

curves are 228.1, 191.3, 164.2, 145.8, 137.2, 130.1, and 123.7 mF cm^{-2} at the current densities of 2, 3, 5, 8, 10, 12, and 15 mA cm^{-2}, respectively.

The porous interconnected nanostructures of a $NiMnO_x$ film provide abundant active sites, which contribute to a significant enhancement in its capacitance. Both CV and GDC curves confirm a high pseudocapacitance of the $NiMnO_x$@DC electrode, arising from fast Faradaic reactions. Moreover, the specific capacitance decreases moderately without a significant drop with increasing charging-discharging rate, indicating excellent rate performance.

To explore the capacitance contributions of the $NiMnO_x$@DC electrode, the CV data were further analyzed. It is known that the pseudocapacitive contributions can be characterized by the dependence of the measured peak current (i) on the scan rate (v), which exhibits characteristics of a power law relationship:

$$i = av^b, \tag{5.1}$$

where both a and b are constant.[173–176] **Figure 5.8c** shows a linear relationship between the logarithm peak current density and the logarithm scan rate. The calculated b value of 0.89 suggests that the charge storage behavior of $NiMnO_x$@DC is dominated by surface-controlled redox pseudocapacitive processes, while diffusion-controlled processes (e.g., Na^+ ion intercalation) also make a secondary contribution. Both fast surface redox reactions and ion diffusion participate synergistically in the energy storage processes.

Figure 5.9 presents the cycling stability and morphological evolution of the $NiMnO_x$@DC electrode over 10,000 cycles in 1.0 M Na_2SO_4 electrolyte, together with a comparison to the $NiMnO_x$@CC electrode. As shown in **Figure 5.9a**, the $NiMnO_x$@DC electrode exhibits excellent long-term stability, maintaining approximately 84 % of its initial capacitance after the first 500 cycles and over 73 % after 10,000 cycles. In stark contrast, although the capacitance retention is very similar to that of $NiMnO_x$@DC in the first stage, the $NiMnO_x$@CC electrode shows dramatic degradation after 1500 cycles, retaining only approximately 16 % of its initial capacity after the same cycling period. The significant difference highlights the crucial role of DC support in improving cycling

stability. The capacitance retention profiles reveal distinct degradation process for each electrode. The NiMnO$_x$@DC electrode shows an initial rapid decrease in the first 500 cycles, followed by a more gradual decline, suggesting an initial stabilization process followed by steady-state operation. As previously mentioned in Section 4.4, the NiMnO$_x$@CC electrode undergoes a two-stage degradation process. Both electrodes maintain excellent coulombic efficiency (approaching 100 %) throughout the cycling process, indicating high reversibility of the redox reactions during prolonged operation and suggesting that the capacitance loss is primarily attributed to active material degradation rather than irreversible side reactions.

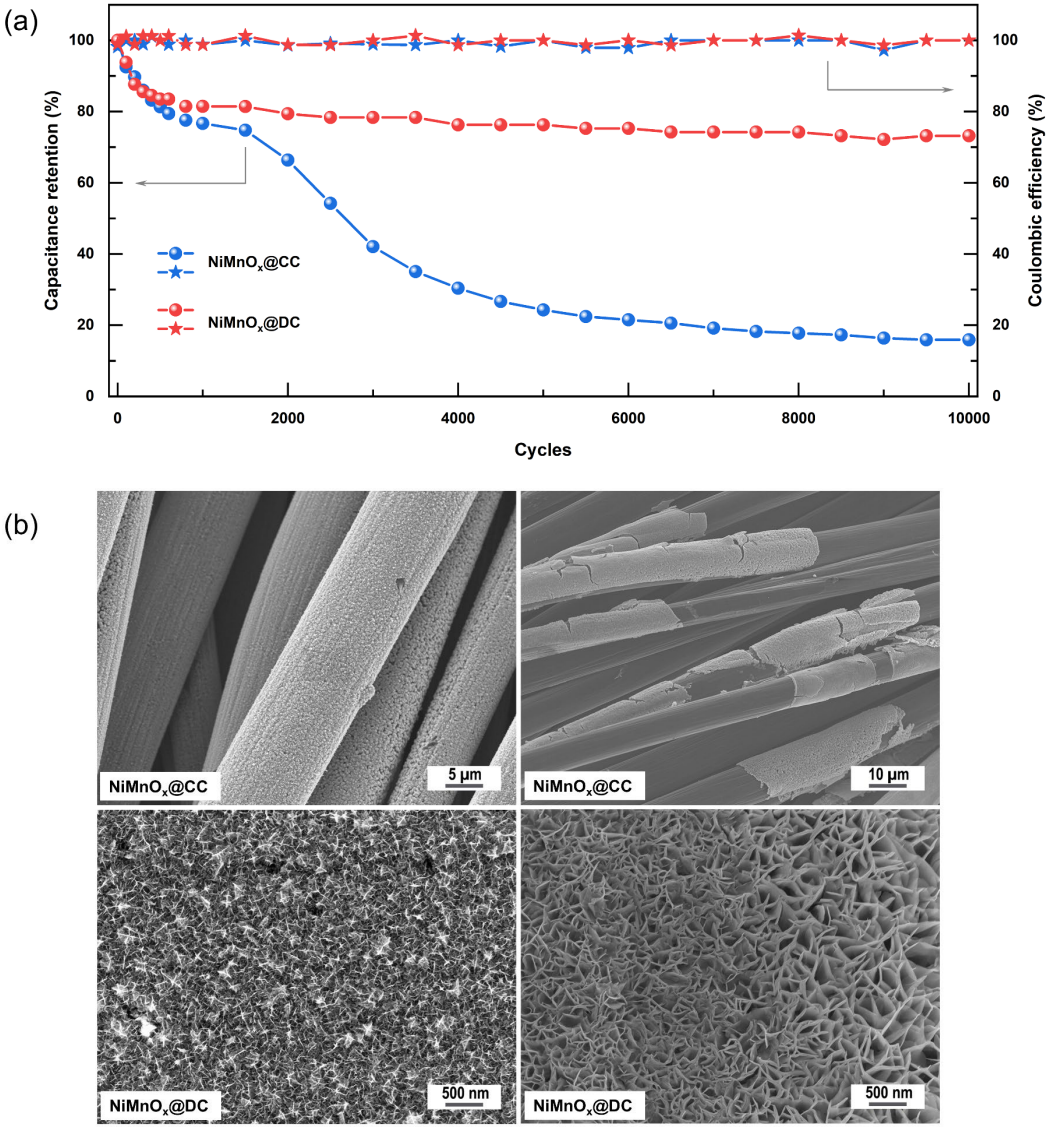


***Figure 5.9**. (a) Capacitance retention and coulombic efficiency of the NiMnO$_x$@DC*

electrode compared with $NiMnO_x$@CC. (b) FESEM images showing the morphologies of $NiMnO_x$@DC and $NiMnO_x$@CC before (left) and after (right) 10,000 charging-discharging cycles.

The FESEM images of these electrodes after such cycling tests were recorded (**Figure 5.9b**), which are expected to provide important insights into the structural evolution occurring during long-term cycling. It is evident that prior to cycling, both electrodes exhibit uniform films coating on the fibers. After 10,000 cycles, significant morphological differences become apparent. The $NiMnO_x$@CC electrode shows severe structural degradation with detachment in fragments of oxide material from the CFs, consistent with poor adhesion as mentioned previously. In contrast, the $NiMnO_x$@DC electrode maintains its structural integrity remarkably well after prolonged cycling. While some morphological changes are observed, the active material remains well-adhered to the DC substrate, changing into a stable, interconnected network. The superior performance of $NiMnO_x$@DC can be rationalized as follows: (i) the DC substrate provides better mechanical support and enhanced adhesion with the active material, suppressing film cracking or detachment caused by redox-induced mechanical strain during repeated charging-discharging cycles; (ii) the exceptional electrochemical inertness and wide potential window of BDD prevent substrate electrochemical oxidation and surface functionalization, thereby maintaining a stable $NiMnO_x$/DC interface during long-term cycling; (iii) the DC substrate maintains better electrical contact with active material throughout cycling, ensuring low interfacial resistance and efficient electron transfer even after morphological changes.

5.3.2 Electrochemical performance using a two-electrode system

To evaluate the practical applicability of the $NiMnO_x$@DC electrode for PC applications, a symmetric two-electrode configuration was constructed and measured in 1.0 M Na_2SO_4 aqueous electrolyte. **Figure 5.10** presents the electrochemical characterization of the symmetric PC.

The CVs recorded at various scan rates (e.g., 10, 20, 50, and 100 mV s^{-1}) are shown in

Figure 5.10a over a wide voltage window of 0—2.6 V. The CVs exhibit characteristic pseudocapacitive behavior with broad redox humps that persist from 10 to 100 mV s^{-1}, evidencing surface-controlled Faradaic reactions. The overall curve shape is well preserved as the scan rate increases, and the current scales nearly linearly with scan rate. All these indicate low charge transfer resistances and excellent rate capability. The estimated specific capacitances from CVs are 54.9, 52.1, 49.2, and 46.4 mF cm^{-2} at the scan rates of 10, 20, 50, and 100 mV s^{-1}, respectively.

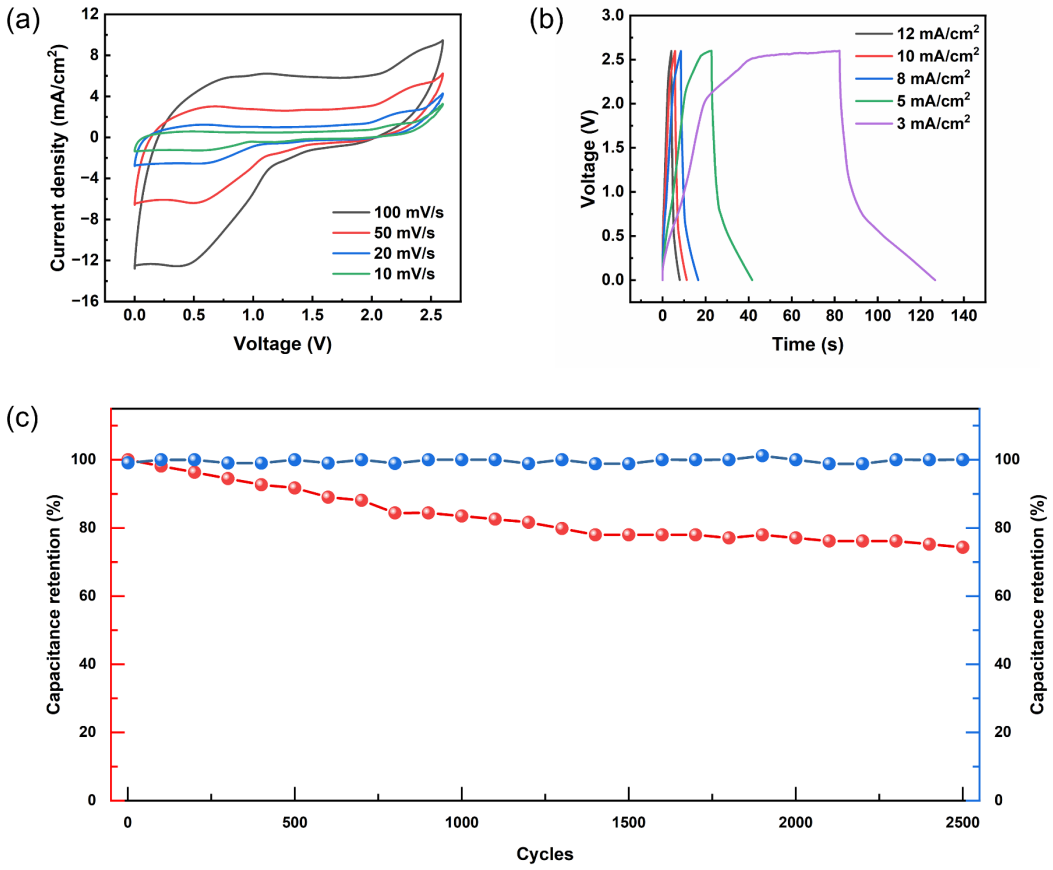


***Figure 5.10**. Electrochemical performance of the NiMnO$_x$@DC electrode using a two-electrode system for PC in 1.0 M Na_2SO_4 solution: (a) CVs at scan rates of 10, 20, 50, and 100 mV s^{-1}, (b) GVD curves at current densities ranging from 3 to 12 mA cm^{-2}, and (C) cycling stability including capacitance retention and coulombic efficiency over 2,500 cycles.*

Figure 5.10b presents the GCD curves of the symmetric NiMnO$_x$@DC PC at the

current densities of 3, 5, 8, 10, and 12 mA cm^{-2}. At high current densities (8—12 mA cm^{-2}), the GCD curves are close to triangular with very small IR drops and exhibit high symmetry, again demonstrating highly reversible surface redox reactions. By contrast, at a low current density (e.g., 3 mA cm^{-2}), the GCD profile shows a long quasi-plateau as the voltage approaches 2.6 V. This hysteresis behavior is consistent with the CVs observed at low scan rates. Side reactions related to water splitting become more pronounced at low charging rates, with a portion of the applied current being diverted to oxygen evolution reactions.[177,178] At higher currents, the device reaches the upper cutoff voltage more rapidly and spends significantly less time in the vicinity of the oxygen evolution reaction regime, resulting in more triangular-shaped curves and reduced parasitic losses. The calculated specific capacitances are 38.8, 21.2, 13.5, 11.5, and 9.8 mF cm^{-2} at the current densities of 3, 5, 8, 10, and 12 mA cm^{-2}, respectively.

The long-term cycling stability of the symmetric $NiMnO_x$@DC PC was evaluated over 2500 charging-discharging cycles. The results are presented in **Figure 5.10c**. The symmetric PC demonstrates remarkable electrochemical stability, retaining approximately 75 % of its initial capacitance after 2,500 cycles. The capacity retention profile also exhibits a characteristic two-stage degradation behavior: an initial rapid decline during the first 800 cycles (from 100 % to 85 %), followed by a more gradual and steady decrease for the subsequent cycles. This initial capacitance loss is commonly attributed to the electrochemical stabilization process of these metal oxide films, where unstable surface species are removed. The subsequent stable average degradation rate of approximately 0.006 % per cycle indicates excellent structural integrity and demonstrates the robust nature of the $NiMnO_x$@DC electrode material in the symmetric configuration in neutral aqueous electrolyte. Moreover, the symmetric PC exhibit ideal coulombic efficiency (99—101 %) throughout 2,500 cycles, confirming the high reversibility of the redox processes and minimal occurrence of parasitic side reactions (e.g., oxygen evolution reaction and hydrogen evolution reaction). This excellent cycling performance validates the practical viability of the symmetric $NiMnO_x$@DC PC for long-term energy storage applications, positioning it as a promising candidate for next-generation aqueous

energy storage devices that require both high performance and prolonged operational lifetime.

5.3.3 Energy density and power density

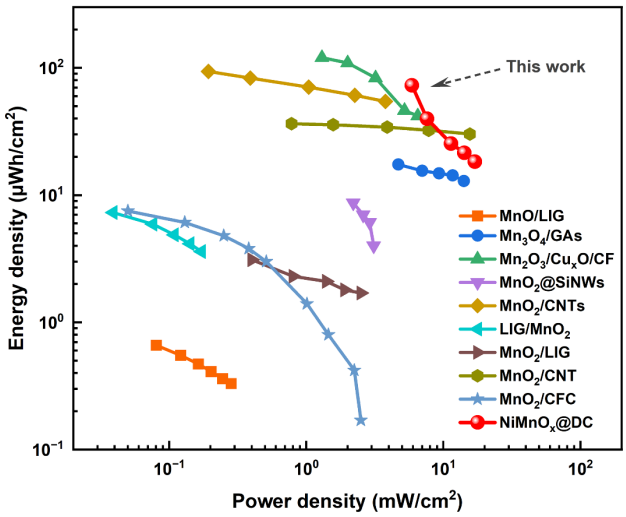


***Figure 5.11**. Ragone plot of the NiMnO$_x$@DC electrode in comparison with other MnO$_x$-based capacitor electrodes.*

The energy density and power density of the NiMnO$_x$@DC PC were calculated based on the GCD curves measured in the two-electrode system. As presented in the Ragone plots (**Figure 5.11**) and summarized in detail **in Table 5.1**, the energy storage performance of the NiMnO$_x$@DC electrode is benchmarked against other manganese oxides-based capacitor electrodes reported in the literature.[179–187] The NiMnO$_x$@DC PC is located in the upper-right region of the Ragone plots, highlighting its exceptional balance between power density and energy density compared to the other systems. Quantitatively, the symmetric PC delivers a maximum areal energy density of 72.8 μWh cm^{-2} at a power density of 5.90 mW cm^{-2} and still sustains 18.3 μWh cm^{-2} even when the areal power density is pushed to 17.0 mW cm^{-2} in 1.0 M Na_2SO_4 aqueous electrolyte. The advantage stems from the integrated architecture: (i) a wide device voltage window enabled by the chemically inert DC electrode support; (ii) the pseudocapacitive Ni–Mn oxide film that

contributes a high areal capacitance; and (iii) low interfacial resistance and strong film-substrate adhesion, which preserve power delivery at high current. The well-balanced performance renders the $NiMnO_x$@DC PC particularly suitable for energy storage applications requiring both high energy density and rapid power delivery. The comparative analysis of $NiMnO_x$@DC with $NiMnO_x$@CC and other MnO_x-based capacitor electrodes confirms that the strategic integration of nickel-manganese oxide chemistry with the DC substrate architecture successfully achieves the design objectives of high performance, stability, and practical applicability in PC systems.

***Table 5.1**. Performance comparison of $NiMnO_x$@DC devices with other MnO_x-based SCs.*

Electrode	**Electrolyte**	**Max. energy density [μWh cm^{-2}]**	**Max. power density [mW cm^{-2}]**	**Reference**
$NiMnO_x$@DC	1.0 M Na_2SO_4	72.8	17.0	This work
MnO/LIG	1.0 M Na_2SO_4	0.66	0.28	[179]
Mn_3O_4/GAs	1.0 M NaOH/PVA	17.4	14.1	[180]
Mn_2O_3/Cu_xO/CF	0.1 g/mL KOH/PVA	120.2	6.5	[181]
MnO_2@SiNWs	0.01 M $LiClO_4$-PMPyrrBTA IL	9.1	0.39	[182]
MnO_2/CNTs	0.2 g/mL LiCl/PVA	93.8	3.78	[183]
LIG/MnO_2	5.0 mM LiCl/PVA	7.3	0.17	[184]
MnO_2/LIG	1.0 M H_2SO_4/PVA	3.1	2.5	[185]
MnO_2/CNT	0.1 g/mL Na_2SO_4/CMC	36.4	15.6	[186]
MnO_2/CFC	LiCl/PVA	7.5	2.5	[187]

5.4 Flexible supercapacitors from $NiMnO_x$-coated diamond cloth

Mechanical flexibility is an important parameter for the $NiMnO_x$@DC electrode. To demonstrate the practical applicability of $NiMnO_x$@DC electrodes in flexible energy storage systems, a symmetric PC was assembled with a quasi-solid Na_2SO_4 gel electrolyte. Mechanical flexibility was assessed under different bending states and during repeated bending cycles (**Figure 5.12**).

Figure 5.12a shows the CVs of the flexible symmetric $NiMnO_x$@DC PC measured at a scan rate of 50 mV s^{-1} under various bending conditions. The device maintains remarkable electrochemical stability across different mechanical states, including flat, 60 °, 90 °, and 180 ° bending angles (as shown in **Figure 5.12b**). The CV profiles show minimal deviation from the original flat-state performance, with well-preserved redox peaks and similar enclosed areas, indicating that the pseudocapacitive behavior remains intact under mechanical stress. The consistency of CVs across different bending angles demonstrates that bending has a limited effect on ion transport and interfacial kinetics.

The mechanical durability of the flexible device was evaluated through repeated cycles of flat-to-180° back-and-forth bending. The results are shown in **Figure 5.12c**. A three-stage evolution during mechanical bending tests is observed. During the first tens of bending cycles, the capacitance increases slightly (up to ~ 120 %) due to enhanced electrolyte penetration and improved interfacial contact under mild mechanical stress. The subsequent gradual decline (to ~ 90 % by 100 bending cycles) is attributed to (i) loss of adhesion between the active material and the substrate, and (ii) modest increases in charge transfer resistance due to accumulation of microcracks within the electrode structure under dynamic deformation. The subsequent stable performance indicates that the device reaches a mechanically equilibrated state, where the electrode structure adapts to the cyclic stress without further significant degradation. After 500 bending cycles, the device retains 79.5 % of its initial capacitance, demonstrating excellent mechanical robustness of the $NiMnO_x$@DC electrode. **Figure 5.12d** presents the GCD curves measured at a bending angle of 180 ° under a current density of 2 mA cm^{-2} during different

stages of the bending test. The curves remain quasi-triangular with a gradual decrease in discharging time, consistent with the moderate capacitance fading. This stability indicates that the electronic and ionic transport pathways remain largely intact despite repeated mechanical deformation.

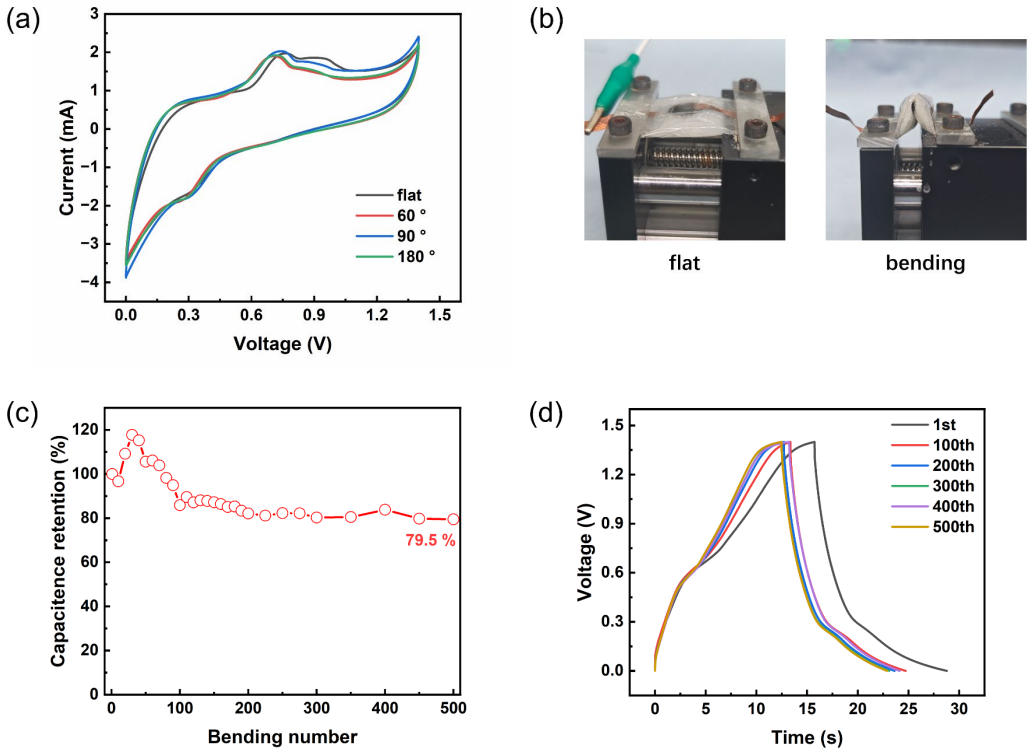


***Figure 5.12**. Mechanical flexibility of the symmetric NiMnO$_x$@DC PC using a gel electrolyte, evaluated through bending tests: (a) CVs measured at a scan rate of 50 mV s^{-1} under different bending conditions; (b) Photographs of the device in flat and bent states; (c) mechanical stability of this PC during repeated bending cycles; and (d) GCD curves recorded at a current density of 2 mA cm^{-2} during the bending tests.*

This mechanical robustness is attributed to the inherent flexibility of the DC substrate and the strong interfacial adhesion between the substrate and the NiMnO$_x$ active material. The above results demonstrate that the integration of pseudocapacitive NiMnO$_x$ with a DC substrate allows the construction of a flexible SC capable of enduring mechanical deformation and repeated bending while maintaining stable electrochemical performance.

5.5 Conclusions

The $NiMnO_x$@DC electrode has been electrochemically synthesized through conformal deposition of a highly pseudocapacitive $NiMnO_x$ film onto the electrochemically inert and mechanically flexible DC substrate. A systematic investigation of the role of the substrate, the influence of deposition potential, structure, composition, and electrochemical performance has been conducted.

In combination with the characterization results from FESEM, Raman, XRD, XPS, and electrochemical measurements, the deposition potential of 1.0 V is identified to be optimal for the formation of a uniform and well-adherent $NiMnO_x$ film that is conformal to DC electrode support. The DC substrate provides a stronger interfacial adhesion to $NiMnO_x$ film compared with the CC substrate, which is more susceptible to electrochemical oxidation. Therefore, the $NiMnO_x$@DC electrode exhibits overall enhanced electrochemical performance compared with the $NiMnO_x$@CC electrode, including a higher capacitance, comparable rate capability, and significantly improved cycling stability.

The optimized $NiMnO_x$@DC electrode exhibits pronounced redox features and high areal capacitances of 180.5 mF cm^{-2} at a scan rate of 10 mV s^{-1} and 228.1 mF cm^{-2} at a current density of 2 mA cm^{-2} with exceptional coulombic efficiency approaching 100 % over 10,000 charging-discharging cycles. In terms of capacitance retention, $NiMnO_x$@DC retains 73 % of its initial capacitance after 10,000 cycles, significantly outperforming the 16 % retention observed for $NiMnO_x$@CC under the identical cycling conditions. These results underscore the electrochemical inertness and adhesion advantages of sp^3 carbon (BDD) over sp^2 carbon for Faradaic reactions. The symmetric $NiMnO_x$@DC PC maintains excellent electrochemical performance including a wide voltage window, high capacitance, and long-term cycling stability. This PC delivers a maximum energy density of 72.8 µWh cm^{-2} at the power density of 5.90 mW cm^{-2} and retains 18.3 µWh cm^{-2} at the power density of 17.0 mW cm^{-2} in 1.0 M Na_2SO_4 aqueous electrolyte, demonstrating a superior balance between energy density and high power

output. The quasi-solid-state flexible $NiMnO_x$@DC PC exhibits excellent mechanical flexibility during the bending tests. The electrochemical performance of the device is well preserved under mechanical stress and dynamic deformation.

In summary, the $NiMnO_x$@DC electrode material exhibits high specific capacitances, excellent rate capability, exceptional coulombic efficiency, long-term cycling stability, and excellent mechanical flexibility. Owing to its excellent electrochemical performance, $NiMnO_x$@DC is expected to emerge as a strong candidate for high-performance flexible SCs, particularly suitable for wearable and portable electronic devices.

6 Summary and Perspectives

This thesis presents a rational materials engineering strategy for the development of electrode materials in flexible SC through systematic electrode integration. Three electrode systems are progressively constructed, namely the flexible diamond cloth (DC), $NiMnO_x$-coated carbon cloth ($NiMnO_x$@CC), and $NiMnO_x$-coated diamond cloth ($NiMnO_x$@DC). The progressive design strategy offers valuable insights into the interplay among substrate chemistry, interfacial stability, and electrochemical performance. The overarching goal was to simultaneously achieve mechanical flexibility, high energy density, and high power density, thereby meeting the critical requirements of electrode materials for flexible SCs.

The comparative analysis across the three electrode systems reveals critical insights into the role of substrate properties in determining the overall performance of SCs, particularly their cycling stability. The DC electrode combines the inherent advantages of CC substrate and BDD film, namely showcasing a wide potential window, exceptionally long cycling life, and excellent mechanical flexibility. However, its capacitance and energy density are intrinsically limited by electric double-layer mechanism. The $NiMnO_x$@CC electrode provides high specific pseudocapacitance (e.g., 47.1 mF cm^{-2} at the scan rate of 10 mV s^{-1}) but undergoes interfacial degradation and film delamination during long-term cycling, resulting in severe capacity fading (e.g., 16 % capacitance retention after 10,000 cycles). The failure mechanism analysis reveals that sp^2 carbon substrates create an inherent limitation: their susceptibility to electrochemical oxidation under pseudocapacitive operating conditions leads to interfacial degradation regardless of active material quality. By replacing the CC substrate with DC, $NiMnO_x$@DC successfully integrates the high pseudocapacitance of the $NiMnO_x$ film with the exceptional stability of the DC substrate. The $NiMnO_x$@DC electrode not only delivers a higher capacitance (228.1 mF cm^{-2}) but also a significantly improved cycling stability (e.g., 73 % capacitance retention after 10,000 cycles). Generally, the enhanced stability of this electrode is attributed to two key factors: (i) The BDD surface of DC provides a

more robust and electrochemically stable anchor for the $NiMnO_x$ film; (ii) the wide electrochemical window and corrosion resistance of BDD prevent the substrate oxidation of surface carbon. In addition, this electrode also exhibits excellent mechanical flexibility. With a maximum energy density of 72.8 μWh cm^{-2} and a maximum power density of 17.0 mW cm^{-2}, this electrode ranks among the competitive candidates for high-performance flexible SC applications. Therefore, it is suggested that using an electrochemically inert platform represents an effective strategy for fully exploiting pseudocapacitive materials, as it minimizes the degradation during long-time cycling that limits sp^2 carbon supports.

In summary, this thesis establishes a rational electrode design paradigm that can be generalized to other pseudocapacitive systems for the development of high-performance flexible SCs. By employing a mechanically robust, electrochemically inert flexible substrate as a structural foundation and integrating it with a conformal and redox-active pseudocapacitive films, the resulting electrode architecture is expected to exhibit superior cycling stability, high energy and power density, and excellent mechanical flexibility, paving the way for broader applications in wearable and portable electronic devices.

While the $NiMnO_x$@DC electrode already exhibits excellent electrochemical activity and mechanical robustness, several avenues merit deeper investigation for further research, spinning from fundamental material synthesis and mechanistic studies to practical device integration and application.

A more in-depth characterization of the microstructure is essential for optimizing its composition and enhancing long-term stability. For example, HRTEM coupled with FFT patterns should be carried out to provide detailed insights into the microstructure of the synthesized $NiMnO_x$ thin films, enabling the assessment of their crystalline degree and the distinction between amorphous domains and nanocrystalline regions. On the compositional side, the average Mn valence should be fine-tuned to maximize capacitive redox while minimizing dissolution. Precise control of the Ni/Mn ratio can be meaningful and critical: Ni can improve electronic transport and introduce additional redox centers, but excessive Ni may dilute Mn-centered charge storage and destabilize the oxide. To suppress Mn dissolution and thereby improve capacitance retention during extended

cycling, suitable electrolyte additives can be introduced to reduce parasitic reactions.[163,188,189]

Transitioning to mass production requires addressing synthesis scalability. For DC, alternative approaches such as hot filament CVD or roll-to-roll compatible processes could improve throughput while maintaining quality. The electrochemical $NiMnO_x$ deposition offers inherent scaling advantages but requires optimization for continuous processing and consideration of alternative methods like atomic layer deposition for large-scale manufacturing.[190,191]

Advanced in situ techniques including XPS, X-ray absorption spectroscopy (XAS), TEM, and Raman spectroscopy can provide real-time information about valence changes and structural evolution during operation. Theoretical approaches including density functional theory (DFT) calculations and molecular dynamics simulations could elucidate interfacial interactions and ion transport mechanisms, while machine learning approaches could correlate structural parameters with performance.

The ultimate validation of flexible supercapacitor technology lies in its successful integration into practical wearable and portable electronic systems. A prototype flexible SC needs to be fabricated and integrated to power a real-world wearable device, such as a smartwatch. The performance of this integrated demonstrator will be evaluated under realistic mechanical deformations and environmental conditions.

Moreover, based on the $NiMnO_x$@DC electrode as the positive electrode, developing asymmetric flexible SCs using appropriate negative electrodes (e.g., carbon-based materials, diamond-derived electrodes, or other stable EDLC materials) will be promising to extend the cell voltage and boost energy density. The optimization of asymmetric configurations requires careful balancing of charge capacities and cell voltage to maximize energy density while maintaining cycling stability.

In conclusion, by advancing these optimization strategies and research directions, the promising $NiMnO_x$@DC material can be further refined and effectively propelled

towards the development of high-performance flexible SCs, ultimately contributing to the realization of next-generation wearable and portable electronic devices.

7 References

(1) Zhou, G.; Xu, L.; Hu, G.; Mai, L.; Cui, Y. Nanowires for Electrochemical Energy Storage. *Chem. Rev.* **2019**, *119* (20), 11042–11109. https://doi.org/10.1021/acs.chemrev.9b00326.

(2) Simon, P.; Gogotsi, Y. Perspectives for Electrochemical Capacitors and Related Devices. *Nat. Mater.* **2020**, *19* (11), 1151–1163. https://doi.org/10.1038/s41563-020-0747-z.

(3) Lu, X.; Wang, Y.; Xu, X.; Yan, B.; Wu, T.; Lu, L. Polymer-Based Solid-State Electrolytes for High-Energy-Density Lithium-Ion Batteries – Review. *Advanced Energy Materials* **2023**, *13* (38), 2301746. https://doi.org/10.1002/aenm.202301746.

(4) Fan, E.; Li, L.; Wang, Z.; Lin, J.; Huang, Y.; Yao, Y.; Chen, R.; Wu, F. Sustainable Recycling Technology for Li-Ion Batteries and Beyond: Challenges and Future Prospects. *Chem. Rev.* **2020**, *120* (14), 7020–7063. https://doi.org/10.1021/acs.chemrev.9b00535.

(5) Zhu, Q.; Zhao, D.; Cheng, M.; Zhou, J.; Owusu, K. A.; Mai, L.; Yu, Y. A New View of Supercapacitors: Integrated Supercapacitors. *Advanced Energy Materials* **2019**, *9* (36), 1901081. https://doi.org/10.1002/aenm.201901081.

(6) Wang, Y.; Xia, Y. Recent Progress in Supercapacitors: From Materials Design to System Construction. *Advanced Materials* **2013**, *25* (37), 5336–5342. https://doi.org/10.1002/adma.201301932.

(7) Simon, P.; Gogotsi, Y. Materials for Electrochemical Capacitors. *Nature Mater* **2008**, *7* (11), 845–854. https://doi.org/10.1038/nmat2297.

(8) Wang, Y.; Song, Y.; Xia, Y. Electrochemical Capacitors: Mechanism, Materials, Systems, Characterization and Applications. *Chem. Soc. Rev.* **2016**, *45* (21), 5925–5950. https://doi.org/10.1039/C5CS00580A.

(9) Becker, H. I.; Ferry, V. Low Voltage Electrolytic Capacitor. *United States Patent Office* **1957**, *2,800,616*.

(10) Béguin, F.; Presser, V.; Balducci, A.; Frackowiak, E. Carbons and Electrolytes for Advanced Supercapacitors. *Advanced Materials* **2014**, *26* (14), 2219–2251.

https://doi.org/10.1002/adma.201304137.

(11) Yu, S.; Yang, N.; Liu, S.; Jiang, X. Diamond Supercapacitors: Progress and Perspectives. *Curr. Opin. Solid State Mater. Sci.* **2021**, *25* (3), 100922. https://doi.org/10.1016/j.cossms.2021.100922.

(12) Qin, K.; Baucom, J.; Diao, L.; Lu, Y.; Zhao, N. Compacted N-Doped 3D Bicontinuous Nanoporous Graphene/Carbon nanotubes@Ni-Doped MnO_2 Electrode for Ultrahigh Volumetric Performance All-Solid-State Supercapacitors at Wide Temperature Range. *Small* **2022**, *18* (33), 2203166. https://doi.org/10.1002/smll.202203166.

(13) Wang, J.-G.; Kang, F.; Wei, B. Engineering of MnO_2-Based Nanocomposites for High-Performance Supercapacitors. *Progress in Materials Science* **2015**, *74*, 51–124. https://doi.org/10.1016/j.pmatsci.2015.04.003.

(14) Liu, X.; Liu, C.-F.; Xu, S.; Cheng, T.; Wang, S.; Lai, W.-Y.; Huang, W. Porous Organic Polymers for High-Performance Supercapacitors. *Chemical Society Reviews* **2022**, *51* (8), 3181–3225. https://doi.org/10.1039/D2CS00065B.

(15) Zhong, M.; Zhang, M.; Li, X. Carbon Nanomaterials and Their Composites for Supercapacitors. *Carbon Energy* **2022**, *4* (5), 950–985. https://doi.org/10.1002/cey2.219.

(16) Kumar, S.; Saeed, G.; Zhu, L.; Hui, K. N.; Kim, N. H.; Lee, J. H. 0D to 3D Carbon-Based Networks Combined with Pseudocapacitive Electrode Material for High Energy Density Supercapacitor: A Review. *Chemical Engineering Journal* **2021**, *403*, 126352. https://doi.org/10.1016/j.cej.2020.126352.

(17) Xie, P.; Yuan, W.; Liu, X.; Peng, Y.; Yin, Y.; Li, Y.; Wu, Z. Advanced Carbon Nanomaterials for State-of-the-Art Flexible Supercapacitors. *Energy Storage Materials* **2021**, *36*, 56–76. https://doi.org/10.1016/j.ensm.2020.12.011.

(18) Zhang, Y.; Mei, H.; Cao, Y.; Yan, X.; Yan, J.; Gao, H.; Luo, H.; Wang, S.; Jia, X.; Kachalova, L.; Yang, J.; Xue, S.; Zhou, C.; Wang, L.; Gui, Y. Recent Advances and Challenges of Electrode Materials for Flexible Supercapacitors. *Coordination Chemistry Reviews* **2021**, *438*, 213910. https://doi.org/10.1016/j.ccr.2021.213910.

(19) Benzigar, M. R.; Dasireddy, V. D. B. C.; Guan, X.; Wu, T.; Liu, G. Advances on

Emerging Materials for Flexible Supercapacitors: Current Trends and Beyond. *Advanced Functional Materials* **2020**, *30* (40), 2002993. https://doi.org/10.1002/adfm.202002993.

(20) Lu, X.; Yu, M.; Wang, G.; Tong, Y.; Li, Y. Flexible Solid-State Supercapacitors: Design, Fabrication and Applications. *Energy Environ. Sci.* **2014**, *7* (7), 2160–2181. https://doi.org/10.1039/C4EE00960F.

(21) Mao, L.; Meng, Q.; Ahmad, A.; Wei, Z. Mechanical Analyses and Structural Design Requirements for Flexible Energy Storage Devices. *Advanced Energy Materials* **2017**, *7* (23), 1700535. https://doi.org/10.1002/aenm.201700535.

(22) Liu, W.; Song, M.-S.; Kong, B.; Cui, Y. Flexible and Stretchable Energy Storage: Recent Advances and Future Perspectives. *Advanced Materials* **2017**, *29* (1), 1603436. https://doi.org/10.1002/adma.201603436.

(23) G. Mackanic, D.; Chang, T.-H.; Huang, Z.; Cui, Y.; Bao, Z. Stretchable Electrochemical Energy Storage Devices. *Chemical Society Reviews* **2020**, *49* (13), 4466–4495. https://doi.org/10.1039/D0CS00035C.

(24) Wang, G.; Zhang, L.; Zhang, J. A Review of Electrode Materials for Electrochemical Supercapacitors. *Chemical Society Reviews* **2012**, *41* (2), 797–828. https://doi.org/10.1039/C1CS15060J.

(25) Shao, Y.; El-Kady, M. F.; Sun, J.; Li, Y.; Zhang, Q.; Zhu, M.; Wang, H.; Dunn, B.; Kaner, R. B. Design and Mechanisms of Asymmetric Supercapacitors. *Chem. Rev.* **2018**, *118* (18), 9233–9280. https://doi.org/10.1021/acs.chemrev.8b00252.

(26) Helmholtz, H. Ueber Einige Gesetze Der Vertheilung Elektrischer Ströme in Körperlichen Leitern, Mit Anwendung Auf Die Thierisch-Elektrischen Versuche (Schluss.). *Annalen der Physik* **1853**, *165* (7), 353–377. https://doi.org/10.1002/andp.18531650702.

(27) Gouy, M. Sur la constitution de la charge électrique à la surface d'un électrolyte. *J. Phys. Theor. Appl.* **1910**, *9* (1), 457–468. https://doi.org/10.1051/jphystap:019100090045700.

(28) Chapman, D. L. A Contribution to the Theory of Electrocapillarity. *The London, Edinburgh, and Dublin Philosophical Magazine and Journal of Science* **1913**, *25*

(148), 475–481. https://doi.org/10.1080/14786440408634187.

(29) Stern, O. Zur Theorie Der Elektrolytischen Doppelschicht. *Zeitschrift für Elektrochemie und angewandte physikalische Chemie* **1924**, *30* (21–22), 508–516. https://doi.org/10.1002/bbpc.192400182.

(30) Grahame, D. C. The Electrical Double Layer and the Theory of Electrocapillarity. *Chem. Rev.* **1947**, *41* (3), 441–501. https://doi.org/10.1021/cr60130a002.

(31) Fang, B.; Binder, L. A Novel Carbon Electrode Material for Highly Improved EDLC Performance. *J. Phys. Chem. B* **2006**, *110* (15), 7877–7882. https://doi.org/10.1021/jp060110d.

(32) Chmiola, J.; Yushin, G.; Gogotsi, Y.; Portet, C.; Simon, P.; Taberna, P. L. Anomalous Increase in Carbon Capacitance at Pore Sizes Less Than 1 Nanometer. *Science* **2006**, *313* (5794), 1760–1763. https://doi.org/10.1126/science.1132195.

(33) Conway, B. E. Capacitance Behavior of Films of Conducting, Electrochemically Reactive Polymers. In *Electrochemical Supercapacitors: Scientific Fundamentals and Technological Applications*; Conway, B. E., Ed.; Springer US: Boston, MA, 1999; pp 299–334. https://doi.org/10.1007/978-1-4757-3058-6_12.

(34) Jiang, Y.; Liu, J. Definitions of Pseudocapacitive Materials: A Brief Review. *ENERGY & ENVIRONMENTAL MATERIALS* **2019**, *2* (1), 30–37. https://doi.org/10.1002/eem2.12028.

(35) Zhang, L.; Zhao, S. X. Carbon-Based Materials as Supercapacitor Electrodes. *Chemical Society Reviews* **2009**, *38* (9), 2520–2531. https://doi.org/10.1039/B813846J.

(36) Augustyn, V.; Simon, P.; Dunn, B. Pseudocapacitive Oxide Materials for High-Rate Electrochemical Energy Storage. *Energy Environ. Sci.* **2014**, *7* (5), 1597–1614. https://doi.org/10.1039/C3EE44164D.

(37) Schmidt, U.; Vinzelberg, S.; Staikov, G. Pb UPD on Ag(100) and Au(100) — 2D Phase Formation Studied by in Situ STM. *Surface Science* **1996**, *348* (3), 261–279. https://doi.org/10.1016/0039-6028(95)01000-9.

(38) Herrero, E.; Buller, L. J.; Abruña, H. D. Underpotential Deposition at Single Crystal Surfaces of Au, Pt, Ag and Other Materials. *Chem. Rev.* **2001**, *101* (7), 1897–1930.

https://doi.org/10.1021/cr9600363.

(39) Srividhya, G.; Ponpandian, N. Pseudocapacitance: Mechanism and Characteristics. In *Pseudocapacitors: Fundamentals to High Performance Energy Storage Devices*; Gupta, R. K., Ed.; Springer Nature Switzerland: Cham, 2024; pp 39–56. https://doi.org/10.1007/978-3-031-45430-1_3.

(40) Augustyn, V.; Come, J.; Lowe, M. A.; Kim, J. W.; Taberna, P.-L.; Tolbert, S. H.; Abruña, H. D.; Simon, P.; Dunn, B. High-Rate Electrochemical Energy Storage through Li^+ Intercalation Pseudocapacitance. *Nature Mater* **2013**, *12* (6), 518–522. https://doi.org/10.1038/nmat3601.

(41) Simon, P.; Gogotsi, Y.; Dunn, B. Where Do Batteries End and Supercapacitors Begin? *Science* **2014**, *343* (6176), 1210–1211. https://doi.org/10.1126/science.1249625.

(42) Tang, P.; Tan, W.; Deng, G.; Zhang, Y.; Xu, S.; Wang, Q.; Li, G.; Zhu, J.; Dou, Q.; Yan, X. Understanding Pseudocapacitance Mechanisms by Synchrotron X-Ray Analytical Techniques. *ENERGY & ENVIRONMENTAL MATERIALS* **2023**, *6* (4), e12619. https://doi.org/10.1002/eem2.12619.

(43) Li, S.; Qiu, J.; Lai, C.; Ling, M.; Zhao, H.; Zhang, S. Surface Capacitive Contributions: Towards High Rate Anode Materials for Sodium Ion Batteries. *Nano Energy* **2015**, *12*, 224–230. https://doi.org/10.1016/j.nanoen.2014.12.032.

(44) Lee, J.; Srimuk, P.; Fleischmann, S.; Su, X.; Hatton, T. A.; Presser, V. Redox-Electrolytes for Non-Flow Electrochemical Energy Storage: A Critical Review and Best Practice. *Progress in Materials Science* **2019**, *101*, 46–89. https://doi.org/10.1016/j.pmatsci.2018.10.005.

(45) Park, J.; Lee, J.; Kim, W. Redox-Active Water-in-Salt Electrolyte for High-Energy-Density Supercapacitors. *ACS Energy Lett.* **2022**, *7* (4), 1266–1273. https://doi.org/10.1021/acsenergylett.2c00015.

(46) Gorska, B.; Frackowiak, E.; Beguin, F. Redox Active Electrolytes in Carbon/Carbon Electrochemical Capacitors. *Current Opinion in Electrochemistry* **2018**, *9*, 95–105. https://doi.org/10.1016/j.coelec.2018.05.006.

(47) Chun, S.-E.; Evanko, B.; Wang, X.; Vonlanthen, D.; Ji, X.; Stucky, G. D.; Boettcher, S. W. Design of Aqueous Redox-Enhanced Electrochemical Capacitors with High

Specific Energies and Slow Self-Discharge. *Nat Commun* **2015**, *6* (1), 7818. https://doi.org/10.1038/ncomms8818.

(48) Yang, N.; Yu, S.; Zhang, W.; Cheng, H.; Simon, P.; Jiang, X. Electrochemical Capacitors with Confined Redox Electrolytes and Porous Electrodes. *Adv. Mater.* **2022**, 2202380. https://doi.org/10.1002/adma.202202380.

(49) Lee, J.; Choudhury, S.; Weingarth, D.; Kim, D.; Presser, V. High Performance Hybrid Energy Storage with Potassium Ferricyanide Redox Electrolyte. *ACS Appl. Mater. Interfaces* **2016**, *8* (36), 23676–23687. https://doi.org/10.1021/acsami.6b06264.

(50) Wang, G.; Liang, R.; Liu, L.; Zhong, B. Improving the Specific Capacitance of Carbon Nanotubes-Based Supercapacitors by Combining Introducing Functional Groups on Carbon Nanotubes with Using Redox-Active Electrolyte. *Electrochimica Acta* **2014**, *115*, 183–188. https://doi.org/10.1016/j.electacta.2013.10.165.

(51) Zhong, C.; Deng, Y.; Hu, W.; Qiao, J.; Zhang, L.; Zhang, J. A Review of Electrolyte Materials and Compositions for Electrochemical Supercapacitors. *Chemical Society Reviews* **2015**, *44* (21), 7484–7539. https://doi.org/10.1039/C5CS00303B.

(52) Yan, J.; Liu, T.; Liu, X.; Yan, Y.; Huang, Y. Metal-Organic Framework-Based Materials for Flexible Supercapacitor Application. *Coordination Chemistry Reviews* **2022**, *452*, 214300. https://doi.org/10.1016/j.ccr.2021.214300.

(53) Liu, X.; Xu, W.; Zheng, D.; Li, Z.; Zeng, Y.; Lu, X. Carbon Cloth as an Advanced Electrode Material for Supercapacitors: Progress and Challenges. *J. Mater. Chem. A* **2020**, *8* (35), 17938–17950. https://doi.org/10.1039/D0TA03463K.

(54) Zhang, S.; Xiao, S.; Li, D.; Liao, J.; Ji, F.; Liu, H.; Ci, L. Commercial Carbon Cloth: An Emerging Substrate for Practical Lithium Metal Batteries. *Energy Storage Materials* **2022**, *48*, 172–190. https://doi.org/10.1016/j.ensm.2022.03.014.

(55) Yu, D.; Zhai, S.; Jiang, W.; Goh, K.; Wei, L.; Chen, X.; Jiang, R.; Chen, Y. Transforming Pristine Carbon Fiber Tows into High Performance Solid-State Fiber Supercapacitors. *Advanced Materials* **2015**, *27* (33), 4895–4901. https://doi.org/10.1002/adma.201501948.

(56) Jang, J.; Shin, M.; Kwon, Y.; Jo, C. Carbon Cloth Modified by Direct Growth of Nitrogen-Doped Carbon Nanofibers and Its Utilization as Electrode for Zero Gap

Flow Batteries. *Chemical Engineering Journal* **2024**, *481*, 148644. https://doi.org/10.1016/j.cej.2024.148644.

(57) Long, J.; Guan, L.; Wang, J.; Liu, H.; Wang, B.; Xiong, Y. Battery-like Flexible Supercapacitors from Vertical 3D Diamond/Graphite Composite Films on Carbon Cloth. *Carbon* **2022**, *197*, 400–407. https://doi.org/10.1016/j.carbon.2022.06.042.

(58) Tjandra, R.; Liu, W.; Zhang, M.; Yu, A. All-Carbon Flexible Supercapacitors Based on Electrophoretic Deposition of Graphene Quantum Dots on Carbon Cloth. *Journal of Power Sources* **2019**, *438*, 227009. https://doi.org/10.1016/j.jpowsour.2019.227009.

(59) Wang, H.; Xu, C.; Chen, Y.; Wang, Y. MnO_2 Nanograsses on Porous Carbon Cloth for Flexible Solid-State Asymmetric Supercapacitors with High Energy Density. *Energy Storage Materials* **2017**, *8*, 127–133. https://doi.org/10.1016/j.ensm.2017.05.007.

(60) Yang, N.; Yu, S.; V. Macpherson, J.; Einaga, Y.; Zhao, H.; Zhao, G.; M. Swain, G.; Jiang, X. Conductive Diamond: Synthesis, Properties, and Electrochemical Applications. *Chem. Soc. Rev.* **2019**, *48* (1), 157–204. https://doi.org/10.1039/C7CS00757D.

(61) Li, C.; Jiang, X.; Yang, N. Synthesis, Surface Chemistry, and Applications of Non-Zero-Dimensional Diamond Nanostructures. *Small* **2024**, *n/a* (n/a), 2400798. https://doi.org/10.1002/smll.202400798.

(62) Hoffmann, R.; Obloh, H.; Tokuda, N.; Yang, N.; Nebel, C. E. Fractional Surface Termination of Diamond by Electrochemical Oxidation. *Langmuir* **2012**, *28* (1), 47–50. https://doi.org/10.1021/la2039366.

(63) Aradilla, D.; Gao, F.; Lewes-Malandrakis, G.; Müller-Sebert, W.; Gentile, P.; Boniface, M.; Aldakov, D.; Iliev, B.; Schubert, T. J. S.; Nebel, C. E.; Bidan, G. Designing 3D Multihierarchical Heteronanostructures for High-Performance on-Chip Hybrid Supercapacitors: Poly(3,4-(Ethylenedioxy)Thiophene)-Coated Diamond/Silicon Nanowire Electrodes in an Aprotic Ionic Liquid. *ACS Appl. Mater. Interfaces* **2016**, *8* (28), 18069–18077. https://doi.org/10.1021/acsami.6b04816.

(64) Petrák, V.; Vlčková Živcová, Z.; Krýsová, H.; Frank, O.; Zukal, A.; Klimša, L.;

Kopeček, J.; Taylor, A.; Kavan, L.; Mortet, V. Fabrication of Porous Boron-Doped Diamond on SiO_2 Fiber Templates. *Carbon* **2017**, *114*, 457–464. https://doi.org/10.1016/j.carbon.2016.12.012.

(65) Wang, J.; He, Z.; Tan, X.; Wang, T.; He, X.; Zhang, L.; Huang, J.; Chen, G.; Du, K. Hybrid Supercapacitors from Porous Boron-Doped Diamond with Water-Soluble Redox Electrolyte. *Surf. Coat. Technol.* **2020**, *398*, 126103. https://doi.org/10.1016/j.surfcoat.2020.126103.

(66) Wang, J.; He, Z.; Tan, X.; Wang, T.; Liu, L.; He, X.; Liu, X. D.; Zhang, L.; Du, K. High-Performance 2.6 V Aqueous Symmetric Supercapacitor Based on Porous Boron-Doped Diamond via Regrowth of Diamond Nanoparticles. *Carbon* **2020**, *160*, 71–79. https://doi.org/10.1016/j.carbon.2020.01.004.

(67) Zhuang, H.; Yang, N.; Fu, H.; Zhang, L.; Wang, C.; Huang, N.; Jiang, X. Diamond Network: Template-Free Fabrication and Properties. *ACS Appl. Mater. Interfaces* **2015**, *7* (9), 5384–5390. https://doi.org/10.1021/am508851r.

(68) Yoshimura, M.; Honda, K.; Uchikado, R.; Kondo, T.; Rao, T. N.; Tryk, D. A.; Fujishima, A.; Sakamoto, Y.; Yasui, K.; Masuda, H. Electrochemical Characterization of Nanoporous Honeycomb Diamond Electrodes in Non-Aqueous Electrolytes. *Diam. Relat. Mater.* **2001**, *10* (3–7), 620–626. https://doi.org/10.1016/S0925-9635(00)00381-2.

(69) Gao, F.; Wolfer, M. T.; Nebel, C. E. Highly Porous Diamond Foam as a Thin-Film Micro-Supercapacitor Material. *Carbon* **2014**, *80*, 833–840. https://doi.org/10.1016/j.carbon.2014.09.007.

(70) Gao, F.; Nebel, C. E. Diamond-Based Supercapacitors: Realization and Properties. *ACS Appl. Mater. Interfaces* **2016**, *8* (42), 28244–28254. https://doi.org/10.1021/acsami.5b07027.

(71) Yang, N.; Jiang, X. Rational Design of Diamond Electrodes. *Acc. Chem. Res.* **2022**. https://doi.org/10.1021/acs.accounts.2c00644.

(72) Hébert, C.; Mazellier, J. P.; Scorsone, E.; Mermoux, M.; Bergonzo, P. Boosting the Electrochemical Properties of Diamond Electrodes Using Carbon Nanotube Scaffolds. *Carbon* **2014**, *71*, 27–33. https://doi.org/10.1016/j.carbon.2013.12.083.

(73) Yu, S.; Yang, N.; Vogel, M.; Mandal, S.; Williams, O. A.; Jiang, S.; Schönherr, H.; Yang, B.; Jiang, X. Battery-like Supercapacitors from Vertically Aligned Carbon Nanofiber Coated Diamond: Design and Demonstrator. *Adv. Energy Mater.* **2018**, *8* (12), 1702947. https://doi.org/10.1002/aenm.201702947.

(74) Liu, T.; Li, Y. Addressing the Achilles' Heel of Pseudocapacitive Materials: Long-term Stability. *InfoMat* **2020**, *2* (5), 807–842. https://doi.org/10.1002/inf2.12105.

(75) Fleischmann, S.; Mitchell, J. B.; Wang, R.; Zhan, C.; Jiang, D.; Presser, V.; Augustyn, V. Pseudocapacitance: From Fundamental Understanding to High Power Energy Storage Materials. *Chem. Rev.* **2020**, *120* (14), 6738–6782. https://doi.org/10.1021/acs.chemrev.0c00170.

(76) Ma, Y.; Xie, X.; Yang, W.; Yu, Z.; Sun, X.; Zhang, Y.; Yang, X.; Kimura, H.; Hou, C.; Guo, Z.; Du, W. Recent Advances in Transition Metal Oxides with Different Dimensions as Electrodes for High-Performance Supercapacitors. *Adv Compos Hybrid Mater* **2021**, *4* (4), 906–924. https://doi.org/10.1007/s42114-021-00358-2.

(77) Zhang, L.; Shi, D.; Liu, T.; Jaroniec, M.; Yu, J. Nickel-Based Materials for Supercapacitors. *Materials Today* **2019**, *25*, 35–65. https://doi.org/10.1016/j.mattod.2018.11.002.

(78) Toupin, M.; Brousse, T.; Bélanger, D. Charge Storage Mechanism of MnO_2 Electrode Used in Aqueous Electrochemical Capacitor. *Chem. Mater.* **2004**, *16* (16), 3184–3190. https://doi.org/10.1021/cm049649j.

(79) Huang, Z.-H.; Song, Y.; Feng, D.-Y.; Sun, Z.; Sun, X.; Liu, X.-X. High Mass Loading MnO_2 with Hierarchical Nanostructures for Supercapacitors. *ACS Nano* **2018**, *12* (4), 3557–3567. https://doi.org/10.1021/acsnano.8b00621.

(80) Zheng, J. Y.; Zhao, W. K.; Wang, X.; Zheng, Z.; Zhang, Y.; Wang, H.; Yan, H.; Song, X.; Han, C. B. Electric-Enhanced Hydrothermal Synthesis of Manganese Dioxide for the Synergistic Catalytic of Indoor Low-Concentration Formaldehyde at Room Temperature. *Chemical Engineering Journal* **2020**, *401*, 125790. https://doi.org/10.1016/j.cej.2020.125790.

(81) Pandit, B.; Goda, E. S.; Abu Elella, M. H.; ur Rehman, A.; Eun Hong, S.; Rondiya, S. R.; Barkataki, P.; Shaikh, S. F.; Al-Enizi, A. M.; El-Bahy, S. M.; Ro Yoon, K. One-

Pot Hydrothermal Preparation of Hierarchical Manganese Oxide Nanorods for High-Performance Symmetric Supercapacitors. *Journal of Energy Chemistry* **2022**, *65*, 116–126. https://doi.org/10.1016/j.jechem.2021.05.028.

(82) Nakayama, M.; Yoshida, W. Electrodeposited Manganese Dioxides and Their Composites as Electrocatalysts for Energy Conversion Reactions. *ChemSusChem* **2025**, *18* (5), e202401907. https://doi.org/10.1002/cssc.202401907.

(83) Song, Y.; Pan, Q.; Lv, H.; Yang, D.; Qin, Z.; Zhang, M.-Y.; Sun, X.; Liu, X.-X. Ammonium-Ion Storage Using Electrodeposited Manganese Oxides. *Angewandte Chemie* **2021**, *133* (11), 5782–5786. https://doi.org/10.1002/ange.202013110.

(84) Cestaro, R.; Philippe, L.; Serrà, A.; Gómez, E.; Schmutz, P. Electrodeposited Manganese Oxides as Efficient Photocatalyst for the Degradation of Tetracycline Antibiotics Pollutant. *Chemical Engineering Journal* **2023**, *462*, 142202. https://doi.org/10.1016/j.cej.2023.142202.

(85) Wei, W.; Cui, X.; Chen, W.; Ivey, D. G. Manganese Oxide-Based Materials as Electrochemical Supercapacitor Electrodes. *Chem. Soc. Rev.* **2011**, *40* (3), 1697–1721. https://doi.org/10.1039/C0CS00127A.

(86) Yu, G.; Hu, L.; Vosgueritchian, M.; Wang, H.; Xie, X.; McDonough, J. R.; Cui, X.; Cui, Y.; Bao, Z. Solution-Processed Graphene/MnO_2 Nanostructured Textiles for High-Performance Electrochemical Capacitors. *Nano Lett.* **2011**, *11* (7), 2905–2911. https://doi.org/10.1021/nl2013828.

(87) Li, H.; Yang, H.; Sun, H.; Huang, Y.; An, P.; Yunhua, Y.; Zhao, H. A Manganese Oxide/Biomass Porous Carbon Composite for High-Performance Supercapacitor Electrodes. *Electrochimica Acta* **2024**, *473*, 143514. https://doi.org/10.1016/j.electacta.2023.143514.

(88) Dhas, S. D.; Thonge, P. N.; Mendhe, A. C.; Yun, J.; Kim, D. Nickel Manganite-Based Materials for Electrochemical Supercapacitors: An Overview. *Renewable and Sustainable Energy Reviews* **2024**, *204*, 114819. https://doi.org/10.1016/j.rser.2024.114819.

(89) Liu, X.; Wang, J.; Yang, G. Amorphous Nickel Oxide and Crystalline Manganese Oxide Nanocomposite Electrode for Transparent and Flexible Supercapacitor.

Chemical Engineering Journal **2018**, *347*, 101–110. https://doi.org/10.1016/j.cej.2018.04.070.

(90) Yao, S.; Zhao, R.; Wang, S.; Zhou, Y.; Liu, R.; Hu, L.; Zhang, A.; Yang, R.; Liu, X.; Fu, Z.; Wang, D.; Yang, Z.; Yan, Y.-M. Ni-Doping Induced Structure Distortion of MnO_2 for Highly Efficient Na+ Storage. *Chemical Engineering Journal* **2022**, *429*, 132521. https://doi.org/10.1016/j.cej.2021.132521.

(91) Tan, B.; Chen, N.; Huang, L.; Gao, X.; Tan, L.; Feng, H. Enhanced the Electrochemical Performance of Ni-Doped α-MnO_2 Prepared with One-Pot Process for Supercapacitors. *Journal of Industrial and Engineering Chemistry* **2025**, *141*, 319–327. https://doi.org/10.1016/j.jiec.2024.06.041.

(92) Chen, H. C.; Qin, Y.; Cao, H.; Song, X.; Huang, C.; Feng, H.; Zhao, X. S. Synthesis of Amorphous Nickel–Cobalt–Manganese Hydroxides for Supercapacitor-Battery Hybrid Energy Storage System. *Energy Storage Materials* **2019**, *17*, 194–203. https://doi.org/10.1016/j.ensm.2018.07.018.

(93) Chen, H.; Ai, Y.; Liu, F.; Chang, X.; Xue, Y.; Huang, Q.; Wang, C.; Lin, H.; Han, S. Carbon-Coated Hierarchical Ni–Mn Layered Double Hydroxide Nanoarrays on Ni Foam for Flexible High-Capacitance Supercapacitors. *Electrochimica Acta* **2016**, *213*, 55–65. https://doi.org/10.1016/j.electacta.2016.06.038.

(94) Sun, J.; Li, W.; Zhang, B.; Li, G.; Jiang, L.; Chen, Z.; Zou, R.; Hu, J. 3D Core/Shell Hierarchies of MnOOH Ultrathin Nanosheets Grown on NiO Nanosheet Arrays for High-Performance Supercapacitors. *Nano Energy* **2014**, *4*, 56–64. https://doi.org/10.1016/j.nanoen.2013.12.006.

(95) Girirajan, M.; Bojarajan, A. K.; Pulidindi, I. N.; Hui, K. N.; Sangaraju, S. An Insight into the Nanoarchitecture of Electrode Materials on the Performance of Supercapacitors. *Coordination Chemistry Reviews* **2024**, *518*, 216080. https://doi.org/10.1016/j.ccr.2024.216080.

(96) Bagheri, A.; Taghavi, S.; Bellani, S.; Salimi, P.; Beydaghi, H.; Panda, J.; Isabella Zappia, M.; Mastronardi, V.; Gamberini, A.; Balkrishna Thorat, S.; Abruzzese, M.; Pasquale, L.; Prato, M.; Signoretto, M.; Feng, X.; Bonaccorso, F. Venice's Macroalgae-Derived Active Material for Aqueous, Organic, and Solid-State

Supercapacitors. *Chemical Engineering Journal* **2024**, *496*, 153529. https://doi.org/10.1016/j.cej.2024.153529.

(97) Wang, D.; Xu, L.; Wang, Y.; Xu, W. Rational Synthesis of Porous Carbon Nanocages and Their Potential Application in High Rate Supercapacitors. *Journal of Electroanalytical Chemistry* **2018**, *815*, 166–174. https://doi.org/10.1016/j.jelechem.2018.03.016.

(98) Xue, K.; Zhang, X.; Sun, X.; Su, K.; Wang, Y.; Lang, J.; Zheng, Z. Di-Imidazolium Ionic Liquid Based Electrolytes for High Voltage Electrochemical Double Layer Capacitors. *Journal of Energy Storage* **2024**, *83*, 110473. https://doi.org/10.1016/j.est.2024.110473.

(99) Ye, T.; Li, L.; Zhang, Y. Recent Progress in Solid Electrolytes for Energy Storage Devices. *Advanced Functional Materials* **2020**, *30* (29), 2000077. https://doi.org/10.1002/adfm.202000077.

(100) Su, K.; Wang, C.; Pu, Y.; Wang, Y.; Ma, P.; Liu, L.; Tian, X.; Du, H.; Lang, J. Dilute Aqueous Hybrid Electrolyte Endows a High-Voltage Window for Supercapacitors. *Journal of Alloys and Compounds* **2024**, *1002*, 175354. https://doi.org/10.1016/j.jallcom.2024.175354.

(101) Guo, T.; Zhou, D.; Pang, L.; Sun, S.; Zhou, T.; Su, J. Perspectives on Working Voltage of Aqueous Supercapacitors. *Small* **2022**, *18* (16), 2106360. https://doi.org/10.1002/smll.202106360.

(102) Blomquist, N.; Wells, T.; Andres, B.; Bäckström, J.; Forsberg, S.; Olin, H. Metal-Free Supercapacitor with Aqueous Electrolyte and Low-Cost Carbon Materials. *Sci Rep* **2017**, *7* (1), 39836. https://doi.org/10.1038/srep39836.

(103) Zhao, Y.; Hu, X.; Stucky, G. D.; Boettcher, S. W. Thermodynamic, Kinetic, and Transport Contributions to Hydrogen Evolution Activity and Electrolyte-Stability Windows for Water-in-Salt Electrolytes. *J. Am. Chem. Soc.* **2024**, *146* (5), 3438–3448. https://doi.org/10.1021/jacs.3c12980.

(104) Pattan-Siddappa, G.; Elugoke, S. E.; Erkmen, C.; Kim, S.-Y.; Ebenso, E. E. Flexible Carbon Cloth Electrode: Pioneering the Future of Electrochemical Sensing Devices. *Adv Compos Hybrid Mater* **2025**, *8* (3), 263. https://doi.org/10.1007/s42114-

025-01338-6.

(105) Xiao, Q.; Yang, J.; Wang, X.; Deng, Y.; Han, P.; Yuan, N.; Zhang, L.; Feng, M.; Wang, C.; Liu, R. Carbon-Based Flexible Self-Supporting Cathode for Lithium-Sulfur Batteries: Progress and Perspective. *Carbon Energy* **2021**, *3* (2), 271–302. https://doi.org/10.1002/cey2.96.

(106) Xia, X.; Yang, J.; Liu, Y.; Zhang, J.; Shang, J.; Liu, B.; Li, S.; Li, W. Material Choice and Structure Design of Flexible Battery Electrode. *Advanced Science* **2023**, *10* (3), 2204875. https://doi.org/10.1002/advs.202204875.

(107) Sachan, R.; Bhaumik, A.; Pant, P.; Prater, J.; Narayan, J. Diamond Film Growth by HFCVD on Q-Carbon Seeded Substrate. *Carbon* **2019**, *141*, 182–189. https://doi.org/10.1016/j.carbon.2018.09.058.

(108) Lee, S.-T.; Lin, Z.; Jiang, X. CVD Diamond Films: Nucleation and Growth. *Materials Science and Engineering: R: Reports* **1999**, *25* (4), 123–154. https://doi.org/10.1016/S0927-796X(99)00003-0.

(109) Feng, S.; Xu, R. New Materials in Hydrothermal Synthesis. *Acc. Chem. Res.* **2001**, *34* (3), 239–247. https://doi.org/10.1021/ar0000105.

(110) Darr, J. A.; Zhang, J.; Makwana, N. M.; Weng, X. Continuous Hydrothermal Synthesis of Inorganic Nanoparticles: Applications and Future Directions. *Chem. Rev.* **2017**, *117* (17), 11125–11238. https://doi.org/10.1021/acs.chemrev.6b00417.

(111) Ralchenko, V.; Saveliev, A.; Voronina, S.; Dementjev, A.; Maslakov, K.; Salerno, M.; Podesta, A.; Milani, P. Nanodiamond Seeding for Nucleation and Growth of CVD Diamond Films. In *Synthesis, Properties and Applications of Ultrananocrystalline Diamond*; Gruen, D. M., Shenderova, O. A., Vul', A. Ya., Eds.; Springer Netherlands: Dordrecht, 2005; pp 109–124. https://doi.org/10.1007/1-4020-3322-2_9.

(112) Osswald, S.; Yushin, G.; Mochalin, V.; Kucheyev, S. O.; Gogotsi, Y. Control of Sp^2/Sp^3 Carbon Ratio and Surface Chemistry of Nanodiamond Powders by Selective Oxidation in Air. *J. Am. Chem. Soc.* **2006**, *128* (35), 11635–11642. https://doi.org/10.1021/ja063303n.

(113) Nicholson, R. S.; Shain, Irving. Theory of Stationary Electrode Polarography. Single Scan and Cyclic Methods Applied to Reversible, Irreversible, and Kinetic

Systems. *Anal. Chem.* **1964**, *36* (4), 706–723. https://doi.org/10.1021/ac60210a007.

(114) Cooper, S. R.; McArdle, J. V.; Raymond, K. N. Siderophore Electrochemistry: Relation to Intracellular Iron Release Mechanism. *Proceedings of the National Academy of Sciences* **1978**, *75* (8), 3551–3554. https://doi.org/10.1073/pnas.75.8.3551.

(115) Wang, S.; Zhang, J.; Gharbi, O.; Vivier, V.; Gao, M.; Orazem, M. E. Electrochemical Impedance Spectroscopy. *Nat Rev Methods Primers* **2021**, *1* (1), 41. https://doi.org/10.1038/s43586-021-00039-w.

(116) Mainka, J.; Gao, W.; He, N.; Dillet, J.; Lottin, O. A General Equivalent Electrical Circuit Model for the Characterization of MXene/Graphene Oxide Hybrid-Fiber Supercapacitors by Electrochemical Impedance Spectroscopy – Impact of Fiber Length. *Electrochimica Acta* **2022**, *404*, 139740. https://doi.org/10.1016/j.electacta.2021.139740.

(117) Magar, H. S.; Hassan, R. Y. A.; Mulchandani, A. Electrochemical Impedance Spectroscopy (EIS): Principles, Construction, and Biosensing Applications. *Sensors* **2021**, *21* (19), 6578. https://doi.org/10.3390/s21196578.

(118) Hazelgrove, B.; Matter, L.; Raos, B.; Harland, B.; Cheng, L.; Asplund, M.; Svirskis, D. Electrochemical Impedance Spectroscopy in Vivo for Neurotechnology and Bioelectronics. *Nat Rev Electr Eng* **2025**, *2* (2), 110–124. https://doi.org/10.1038/s44287-024-00126-6.

(119) Einaga, Y. Boron-Doped Diamond Electrodes: Fundamentals for Electrochemical Applications. *Acc. Chem. Res.* **2022**, *55* (24), 3605–3615. https://doi.org/10.1021/acs.accounts.2c00597.

(120) Demlow, S. N.; Rechenberg, R.; Grotjohn, T. The Effect of Substrate Temperature and Growth Rate on the Doping Efficiency of Single Crystal Boron Doped Diamond. *Diamond and Related Materials* **2014**, *49*, 19–24. https://doi.org/10.1016/j.diamond.2014.06.006.

(121) Cheng, X.-B.; Zhao, M.-Q.; Chen, C.; Pentecost, A.; Maleski, K.; Mathis, T.; Zhang, X.-Q.; Zhang, Q.; Jiang, J.; Gogotsi, Y. Nanodiamonds Suppress the Growth of Lithium Dendrites. *Nat. Commun.* **2017**, *8* (1), 336.

https://doi.org/10.1038/s41467-017-00519-2.

(122) Shang, N.; Papakonstantinou, P.; Wang, P.; Zakharov, A.; Palnitkar, U.; Lin, I.-N.; Chu, M.; Stamboulis, A. Self-Assembled Growth, Microstructure, and Field-Emission High-Performance of Ultrathin Diamond Nanorods. *ACS Nano* **2009**, *3* (4), 1032–1038. https://doi.org/10.1021/nn900167p.

(123) Xie, Z.; Deng, Y.; Yang, Y.; Su, H.; Zhou, D.; Liu, C.; Yang, W. Preparation of Nano-Sized Titanium Carbide Particles via a Vacuum Carbothermal Reduction Approach Coupled with Purification under Hydrogen/Argon Mixed Gas. *RSC Advances* **2017**, *7* (15), 9037–9044. https://doi.org/10.1039/C6RA28264D.

(124) Ahmed, S.; Shishir, Md. K. H.; Islam, Md. T.; Rahaman, Md. A.; Aman, S.; Aidid, A. R.; Sadia, S. I.; Rana, Md. M.; Alam, Md. A. Crystallinity Integration of Anatase (TiO_2) Nanocrystal by Whole Powder Pattern Fitting (WPPF) Method: A Rietveld Refinement Study. *Results in Materials* **2025**, *26*, 100673. https://doi.org/10.1016/j.rinma.2025.100673.

(125) Xu, J.; Yang, N.; Heuser, S.; Yu, S.; Schulte, A.; Schönherr, H.; Jiang, X. Achieving Ultrahigh Energy Densities of Supercapacitors with Porous Titanium Carbide/Boron-Doped Diamond Composite Electrodes. *Advanced Energy Materials* **2019**, *9* (17), 1803623. https://doi.org/10.1002/aenm.201803623.

(126) Joshi, P.; Haque, A.; Gupta, S.; Narayan, R. J.; Narayan, J. Synthesis of Multifunctional Microdiamonds on Stainless Steel Substrates by Chemical Vapor Deposition. *Carbon* **2021**, *171*, 739–749. https://doi.org/10.1016/j.carbon.2020.09.064.

(127) Li, Z.; Deng, L.; Kinloch, I. A.; Young, R. J. Raman Spectroscopy of Carbon Materials and Their Composites: Graphene, Nanotubes and Fibres. *Progress in Materials Science* **2023**, *135*, 101089. https://doi.org/10.1016/j.pmatsci.2023.101089.

(128) Knittel, P.; Stach, R.; Yoshikawa, T.; Kirste, L.; Mizaikoff, B.; Kranz, C.; E. Nebel, C. Characterisation of Thin Boron-Doped Diamond Films Using Raman Spectroscopy and Chemometrics. *Analytical Methods* **2019**, *11* (5), 582–586. https://doi.org/10.1039/C8AY02468E.

(129) Mortet, V.; Vlčková Živcová, Z.; Taylor, A.; Frank, O.; Hubík, P.; Trémouilles,

D.; Jomard, F.; Barjon, J.; Kavan, L. Insight into Boron-Doped Diamond Raman Spectra Characteristic Features. *Carbon* **2017**, *115*, 279–284. https://doi.org/10.1016/j.carbon.2017.01.022.

(130) Chen, X.; Wang, X.; Fang, D. A Review on C1s XPS-Spectra for Some Kinds of Carbon Materials. *Fuller. Nanotub. Carbon Nanostructures* **2020**, *28* (12), 1048–1058. https://doi.org/10.1080/1536383X.2020.1794851.

(131) Sadri, R.; Hosseini, M.; Kazi, S. N.; Bagheri, S.; Zubir, N.; Solangi, K. H.; Zaharinie, T.; Badarudin, A. A Bio-Based, Facile Approach for the Preparation of Covalently Functionalized Carbon Nanotubes Aqueous Suspensions and Their Potential as Heat Transfer Fluids. *Journal of Colloid and Interface Science* **2017**, *504*, 115–123. https://doi.org/10.1016/j.jcis.2017.03.051.

(132) Shan, X.-Y.; Wang, Y.; Wang, D.-W.; Li, F.; Cheng, H.-M. Armoring Graphene Cathodes for High-Rate and Long-Life Lithium Ion Supercapacitors. *Advanced Energy Materials* **2016**, *6* (6), 1502064. https://doi.org/10.1002/aenm.201502064.

(133) Hu, L.; Chen, W.; Xie, X.; Liu, N.; Yang, Y.; Wu, H.; Yao, Y.; Pasta, M.; Alshareef, H. N.; Cui, Y. Symmetrical MnO_2–Carbon Nanotube–Textile Nanostructures for Wearable Pseudocapacitors with High Mass Loading. *ACS Nano* **2011**, *5* (11), 8904–8913. https://doi.org/10.1021/nn203085j.

(134) Heuser, S.; Yang, N.; Hof, F.; Schulte, A.; Schönherr, H.; Jiang, X. 3D 3C-SiC/Graphene Hybrid Nanolaminate Films for High-Performance Supercapacitors. *Small* **2018**, *14* (45), 1801857. https://doi.org/10.1002/smll.201801857.

(135) Yu, S.; Liu, S.; Jiang, X.; Yang, N. Recent Advances on Electrochemistry of Diamond Related Materials. *Carbon* **2022**, *200*, 517–542. https://doi.org/10.1016/j.carbon.2022.09.044.

(136) Yu, S.; Sankaran, K. J.; Korneychuk, S.; Verbeeck, J.; Haenen, K.; Jiang, X.; Yang, N. High-Performance Supercabatteries Using Graphite@diamond Nano-Needle Capacitor Electrodes and Redox Electrolytes. *Nanoscale* **2019**, *11* (38), 17939–17946. https://doi.org/10.1039/C9NR07037K.

(137) Zhang, J.; Zhao, Z.; Zhang, Z.; Guo, L.; Xu, L.; Sun, P.; Wang, M.; Gao, M.; Li, Y.; Li, D.; Boukherroub, R. Construction of Flexible Fiber-Shaped Boron-Doped

Diamond Film and Its Supercapacitor Application. *Journal of Colloid and Interface Science* **2023**, *629*, 813–821. https://doi.org/10.1016/j.jcis.2022.08.143.

(138) Gao, F.; Lewes-Malandrakis, G.; Wolfer, M. T.; Müller-Sebert, W.; Gentile, P.; Aradilla, D.; Schubert, T.; Nebel, C. E. Diamond-Coated Silicon Wires for Supercapacitor Applications in Ionic Liquids. *Diamond and Related Materials* **2015**, *51*, 1–6. https://doi.org/10.1016/j.diamond.2014.10.009.

(139) Banerjee, D.; Sankaran, K. J.; Deshmukh, S.; Ficek, M.; Bhattacharya, G.; Ryl, J.; Phase, D. M.; Gupta, M.; Bogdanowicz, R.; Lin, I.-N.; Kanjilal, A.; Haenen, K.; Roy, S. S. 3D Hierarchical Boron-Doped Diamond-Multilayered Graphene Nanowalls as an Efficient Supercapacitor Electrode. *J. Phys. Chem. C* **2019**, *123* (25), 15458–15466. https://doi.org/10.1021/acs.jpcc.9b03628.

(140) Du, P.; Dong, Y.; Kang, H.; Yang, X.; Wang, Q.; Niu, J.; Wang, S.; Liu, P. Graphene-Wrapped Polyaniline Nanowire Array Modified Functionalized of Carbon Cloth for High-Performance Flexible Solid-State Supercapacitor. *ACS Sustainable Chem. Eng.* **2018**, *6* (11), 14723–14733. https://doi.org/10.1021/acssuschemeng.8b03278.

(141) Yu, S.; Yang, N.; Zhuang, H.; Mandal, S.; A. Williams, O.; Yang, B.; Huang, N.; Jiang, X. Battery-like Supercapacitors from Diamond Networks and Water-Soluble Redox Electrolytes. *J. Mater. Chem. A* **2017**, *5* (4), 1778–1785. https://doi.org/10.1039/C6TA08607A.

(142) Guo, C.; Zhang, Y.; Zeng, T.; Huang, D.; Wan, Q.; Yang, N. High-Performance Asymmetric Supercapacitors Using Holey Graphene Electrodes and Redox Electrolytes. *Carbon* **2020**, *157*, 298–307. https://doi.org/10.1016/j.carbon.2019.10.048.

(143) Liao, S.; Peng, C.; Zou, J.; Mandal, S.; Williams, O. A.; Huang, X.; Zhao, M.; Xu, J.; Yang, N.; Yu, S. Boron-Doped Diamond Decorated with Metal-Organic Framework-Derived Compounds for High-Voltage Aqueous Asymmetric Supercapacitors. *Carbon* **2024**, 119651. https://doi.org/10.1016/j.carbon.2024.119651.

(144) Yin, X.; Li, H.; Yuan, R.; Lu, J. Hierarchical Self-Supporting Sugar Gourd-Shape

MOF-Derived $NiCo_2O_4$ Hollow nanocages@SiC Nanowires for High-Performance Flexible Hybrid Supercapacitors. *Journal of Colloid and Interface Science* **2021**, *586*, 219–232. https://doi.org/10.1016/j.jcis.2020.10.086.

(145) Jia, R.; Zhu, F.; Sun, S.; Zhai, T.; Xia, H. Dual Support Ensuring High-Energy Supercapacitors via High-Performance $NiCo_2S_4$@Fe_2O_3 Anode and Working Potential Enlarged MnO_2 Cathode. *Journal of Power Sources* **2017**, *341*, 427–434. https://doi.org/10.1016/j.jpowsour.2016.12.014.

(146) Julien, C.; Massot, M.; Baddour-Hadjean, R.; Franger, S.; Bach, S.; Pereira-Ramos, J. P. Raman Spectra of Birnessite Manganese Dioxides. *Solid State Ionics* **2003**, *159* (3), 345–356. https://doi.org/10.1016/S0167-2738(03)00035-3.

(147) Bernardini, S.; Bellatreccia, F.; Casanova Municchia, A.; Della Ventura, G.; Sodo, A. Raman Spectra of Natural Manganese Oxides. *Journal of Raman Spectroscopy* **2019**, *50* (6), 873–888. https://doi.org/10.1002/jrs.5583.

(148) Zhao, H.; Han, G.; Chang, Y.; Li, M.; Li, Y. The Capacitive Properties of Amorphous Manganese Dioxide Electrodeposited on Different Thermally-Treated Carbon Papers. *Electrochimica Acta* **2013**, *91*, 50–57. https://doi.org/10.1016/j.electacta.2012.12.114.

(149) Cestaro, R.; Schweizer, P.; Philippe, L.; Maeder, X.; Serrà, A. Phase and Microstructure Control of Electrodeposited Manganese Oxide with Enhanced Optical Properties. *Applied Surface Science* **2022**, *580*, 152289. https://doi.org/10.1016/j.apsusc.2021.152289.

(150) Lytle, J. C.; Rhodes, C. P.; Long, J. W.; Pettigrew, K. A.; Stroud, R. M.; Rolison, D. R. The Importance of Combining Disorder with Order for Li-Ion Insertion into Cryogenically Prepared Nanoscopic Ruthenia. *J. Mater. Chem.* **2007**, *17* (13), 1292–1299. https://doi.org/10.1039/B614433K.

(151) Biesinger, M. C.; Payne, B. P.; Grosvenor, A. P.; Lau, L. W. M.; Gerson, A. R.; Smart, R. St. C. Resolving Surface Chemical States in XPS Analysis of First Row Transition Metals, Oxides and Hydroxides: Cr, Mn, Fe, Co and Ni. *Applied Surface Science* **2011**, *257* (7), 2717–2730. https://doi.org/10.1016/j.apsusc.2010.10.051.

(152) Yu, N.; Yin, H.; Zhang, W.; Liu, Y.; Tang, Z.; Zhu, M.-Q. High-Performance

Fiber-Shaped All-Solid-State Asymmetric Supercapacitors Based on Ultrathin MnO_2 Nanosheet/Carbon Fiber Cathodes for Wearable Electronics. *Advanced Energy Materials* **2016**, *6* (2), 1501458. https://doi.org/10.1002/aenm.201501458.

(153) Qiu, W.; Li, Y.; You, A.; Zhang, Z.; Li, G.; Lu, X.; Tong, Y. High-Performance Flexible Quasi-Solid-State Zn–MnO_2 Battery Based on MnO_2 Nanorod Arrays Coated 3D Porous Nitrogen-Doped Carbon Cloth. *Journal of Materials Chemistry A* **2017**, *5* (28), 14838–14846. https://doi.org/10.1039/C7TA03274A.

(154) Patil, B.; Ahn, S.; Yu, S.; Song, H.; Jeong, Y.; Kim, J. H.; Ahn, H. Electrochemical Performance of a Coaxial Fiber-Shaped Asymmetric Supercapacitor Based on Nanostructured MnO_2/CNT-Web Paper and Fe_2O_3/Carbon Fiber Electrodes. *Carbon* **2018**, *134*, 366–375. https://doi.org/10.1016/j.carbon.2018.03.080.

(155) Tang, P.; Han, L.; Zhang, L. Facile Synthesis of Graphite/PEDOT/MnO_2 Composites on Commercial Supercapacitor Separator Membranes as Flexible and High-Performance Supercapacitor Electrodes. *ACS Appl. Mater. Interfaces* **2014**, *6* (13), 10506–10515. https://doi.org/10.1021/am5021028.

(156) Ghods, A.; Zhou, C.; Ferguson, I. T. Structural and Optical Properties of (Zn,Mn)O Thin Films Prepared by Atomic Layer Deposition. *J. Vac. Sci. Technol. A* **2020**, *38* (4), 042408. https://doi.org/10.1116/6.0000141.

(157) Dang, S.; Wen, Y.; Qin, T.; Hao, J.; Li, H.; Huang, J.; Yan, D.; Cao, G.; Peng, S. Nanostructured Manganese Dioxide with Adjustable Mn^{3+}/Mn^{4+} Ratio for Flexible High-Energy Quasi-Solid Supercapacitors. *Chemical Engineering Journal* **2020**, *396*, 125342. https://doi.org/10.1016/j.cej.2020.125342.

(158) Devaraj, S.; Munichandraiah, N. Effect of Crystallographic Structure of MnO_2 on Its Electrochemical Capacitance Properties. *J. Phys. Chem. C* **2008**, *112* (11), 4406–4417. https://doi.org/10.1021/jp7108785.

(159) Wang, X.; Chen, S.; Li, D.; Sun, S.; Peng, Z.; Komarneni, S.; Yang, D. Direct Interfacial Growth of MnO_2 Nanostructure on Hierarchically Porous Carbon for High-Performance Asymmetric Supercapacitors. *ACS Sustainable Chem. Eng.* **2018**, *6* (1), 633–641. https://doi.org/10.1021/acssuschemeng.7b02960.

(160) Yu, S.; Yang, N.; Zhuang, H.; Meyer, J.; Mandal, S.; Williams, O. A.; Lilge, I.;

Schönherr, H.; Jiang, X. Electrochemical Supercapacitors from Diamond. *J. Phys. Chem. C* **2015**, *119* (33), 18918–18926. https://doi.org/10.1021/acs.jpcc.5b04719.

(161) Xu, J.; Yang, N.; Yu, S.; Schulte, A.; Schönherr, H.; Jiang, X. Ultra-High Energy Density Supercapacitors Using a Nickel Phosphide/Nickel/Titanium Carbide Nanocomposite Capacitor Electrode. *Nanoscale* **2020**, *12* (25), 13618–13625. https://doi.org/10.1039/D0NR01984D.

(162) Kanoh, H.; Tang, W.; Makita, Y.; Ooi, K. Electrochemical Intercalation of Alkali-Metal Ions into Birnessite-Type Manganese Oxide in Aqueous Solution. *Langmuir* **1997**, *13* (25), 6845–6849. https://doi.org/10.1021/la970767d.

(163) Ye, X.; Han, D.; Jiang, G.; Cui, C.; Guo, Y.; Wang, Y.; Zhang, Z.; Weng, Z.; Yang, Q.-H. Unraveling the Deposition/Dissolution Chemistry of MnO_2 for High-Energy Aqueous Batteries. *Energy Environ. Sci.* **2023**, *16* (3), 1016–1023. https://doi.org/10.1039/D3EE00018D.

(164) Zhang, Q.-Z.; Zhang, D.; Miao, Z.-C.; Zhang, X.-L.; Chou, S.-L. Research Progress in MnO_2–Carbon Based Supercapacitor Electrode Materials. *Small* **2018**, *14* (24), 1702883. https://doi.org/10.1002/smll.201702883.

(165) Yue, Z. R.; Jiang, W.; Wang, L.; Gardner, S. D.; Pittman, C. U. Surface Characterization of Electrochemically Oxidized Carbon Fibers. *Carbon* **1999**, *37* (11), 1785–1796. https://doi.org/10.1016/S0008-6223(99)00047-0.

(166) Li, C.; Iqbal, M.; Lin, J.; Luo, X.; Jiang, B.; Malgras, V.; Wu, K. C.-W.; Kim, J.; Yamauchi, Y. Electrochemical Deposition: An Advanced Approach for Templated Synthesis of Nanoporous Metal Architectures. *Acc. Chem. Res.* **2018**, *51* (8), 1764–1773. https://doi.org/10.1021/acs.accounts.8b00119.

(167) Tully, J. J.; Houghton, D.; Breeze, B. G.; Mollart, T. P.; Macpherson, J. V. Quantitative Measurement Technique for Anodic Corrosion of BDD Advanced Oxidation Electrodes. *ACS Meas. Sci. Au* **2024**, *4* (3), 267–276. https://doi.org/10.1021/acsmeasuresciau.3c00069.

(168) Zhang, M.; Chen, Y.; Yang, D.; Li, J. High Performance MnO_2 Supercapacitor Material Prepared by Modified Electrodeposition Method with Different Electrodeposition Voltages. *Journal of Energy Storage* **2020**, *29*, 101363.

https://doi.org/10.1016/j.est.2020.101363.

(169) Huang, Y.; Wu, J.; Xiao, X.; Deng, W.; Bai, Y.; Zou, X.; Yang, Y.; Zou, G.; Wu, T.; Hou, H.; Jing, M.; Ji, X. Multivalent Manganese-Based Composite Materials for Sodium Energy Storage in Ether Electrolyte. *Journal of Power Sources* **2023**, *588*, 233742. https://doi.org/10.1016/j.jpowsour.2023.233742.

(170) Su, X.; Sun, B.; Wang, J.; Zhang, W.; Ma, S.; He, X.; Ruan, H. Fast Capacity Estimation for Lithium-Ion Battery Based on Online Identification of Low-Frequency Electrochemical Impedance Spectroscopy and Gaussian Process Regression. *Applied Energy* **2022**, *322*, 119516. https://doi.org/10.1016/j.apenergy.2022.119516.

(171) Bredar, A. R. C.; Chown, A. L.; Burton, A. R.; Farnum, B. H. Electrochemical Impedance Spectroscopy of Metal Oxide Electrodes for Energy Applications. *ACS Appl. Energy Mater.* **2020**, *3* (1), 66–98. https://doi.org/10.1021/acsaem.9b01965.

(172) Zhang, J.; Zhu, L.; Jia, H.; Wei, K.; Wen, L. Microreactor Facilitated Preparation and Ni-Doping of MnO_2 Nanoparticles for Supercapacitors. *Journal of Alloys and Compounds* **2021**, *889*, 161772. https://doi.org/10.1016/j.jallcom.2021.161772.

(173) Wang, J.; Polleux, J.; Lim, J.; Dunn, B. Pseudocapacitive Contributions to Electrochemical Energy Storage in TiO_2 (Anatase) Nanoparticles. *J. Phys. Chem. C* **2007**, *111* (40), 14925–14931. https://doi.org/10.1021/jp074464w.

(174) Wang, X.; Fang, Y.; Shi, B.; Huang, F.; Rong, F.; Que, R. Three-Dimensional $NiCo_2O_4$@$NiCo_2O_4$ Core–Shell Nanocones Arrays for High-Performance Supercapacitors. *Chemical Engineering Journal* **2018**, *344*, 311–319. https://doi.org/10.1016/j.cej.2018.03.061.

(175) Zhang, L.; Hu, X.; Chen, C.; Guo, H.; Liu, X.; Xu, G.; Zhong, H.; Cheng, S.; Wu, P.; Meng, J.; Huang, Y.; Dou, S.; Liu, H. In Operando Mechanism Analysis on Nanocrystalline Silicon Anode Material for Reversible and Ultrafast Sodium Storage. *Advanced Materials* **2017**, *29* (5), 1604708. https://doi.org/10.1002/adma.201604708.

(176) Feng, N.; Meng, R.; Zu, L.; Feng, Y.; Peng, C.; Huang, J.; Liu, G.; Chen, B.; Yang, J. A Polymer-Direct-Intercalation Strategy for MoS_2/Carbon-Derived Heteroaerogels with Ultrahigh Pseudocapacitance. *Nat Commun* **2019**, *10* (1), 1372. https://doi.org/10.1038/s41467-019-09384-7.

(177) Nunes, W. G.; Freitas, B. G. A.; Beraldo, R. M.; Filho, R. M.; Da Silva, L. M.; Zanin, H. A Rational Experimental Approach to Identify Correctly the Working Voltage Window of Aqueous-Based Supercapacitors. *Sci Rep* **2020**, *10* (1), 19195. https://doi.org/10.1038/s41598-020-75851-7.

(178) Gou, Q.; Zhao, S.; Wang, J.; Li, M.; Xue, J. Recent Advances on Boosting the Cell Voltage of Aqueous Supercapacitors. *Nano-Micro Lett.* **2020**, *12* (1), 98. https://doi.org/10.1007/s40820-020-00430-4.

(179) Kim, Y.-R.; Nam, H. K.; Lee, Y.; Yang, D.; Le, T.-S. D.; Kim, S.-W.; Park, S.; Kim, Y.-J. Green Supercapacitor Patterned by Synthesizing MnO/Laser-Induced-Graphene Hetero-Nanostructures on Wood via Femtosecond Laser Pulses. *Biochar* **2024**, *6* (1), 36. https://doi.org/10.1007/s42773-024-00320-7.

(180) Fan, L.; Zhang, Y.; Guo, Z.; Sun, B.; Tian, D.; Feng, Y.; Zhang, N.; Sun, K. Hierarchical Mn_3O_4 Anchored on 3D Graphene Aerogels via C−O−Mn Linkage with Superior Electrochemical Performance for Flexible Asymmetric Supercapacitor. *Chemistry – A European Journal* **2020**, *26* (42), 9314–9318. https://doi.org/10.1002/chem.201903947.

(181) Li, Y.; Jiang, H.; Yan, X.; Zhang, W.; Zhang, M.; Zhu, W.; Pan, J.; Sufyan Javed, M.; Cheng, W.; Guan, Y. Rationally Designed Mn_2O_3/Cu_xO Core–Shell Heterostructure Generated on Copper Foam as Binder-Free Electrode for Flexible Asymmetric Supercapacitor. *Applied Surface Science* **2021**, *566*, 150715. https://doi.org/10.1016/j.apsusc.2021.150715.

(182) Dubal, D. P.; Aradilla, D.; Bidan, G.; Gentile, P.; Schubert, T. J. S.; Wimberg, J.; Sadki, S.; Gomez-Romero, P. 3D Hierarchical Assembly of Ultrathin MnO_2 Nanoflakes on Silicon Nanowires for High Performance Micro-Supercapacitors in Li- Doped Ionic Liquid. *Sci Rep* **2015**, *5* (1), 9771. https://doi.org/10.1038/srep09771.

(183) Jeong, J.-H.; Park, J. W.; Lee, D. W.; Baughman, R. H.; Kim, S. J. Electrodeposition of α-MnO_2/γ-MnO_2 on Carbon Nanotube for Yarn Supercapacitor. *Sci Rep* **2019**, *9* (1), 11271. https://doi.org/10.1038/s41598-019-47744-x.

(184) Klem, M. dos S.; Abreu, R.; Pinheiro, T.; Coelho, J.; Alves, N.; Martins, R. Electrochemical Deposition of Manganese Oxide on Paper-Based Laser-Induced

Graphene for the Fabrication of Sustainable High-Energy-Density Supercapacitors. *Advanced Sustainable Systems* **2024**, *8* (12), 2400254. https://doi.org/10.1002/adsu.202400254.

(185) Zhu, C.; Dong, X.; Mei, X.; Gao, M.; Wang, K.; Zhao, D. Direct Laser Writing of MnO_2 Decorated Graphene as Flexible Supercapacitor Electrodes. *J Mater Sci* **2020**, *55* (36), 17108–17119. https://doi.org/10.1007/s10853-020-05212-2.

(186) Huang, G.; Zhang, Y.; Wang, L.; Sheng, P.; Peng, H. Fiber-Based MnO_2/Carbon Nanotube/Polyimide Asymmetric Supercapacitor. *Carbon* **2017**, *125*, 595–604. https://doi.org/10.1016/j.carbon.2017.09.103.

(187) Raj, C. J.; Manikandan, R.; Cho, W.-J.; Yu, K. H.; Kim, B. C. High-Performance Flexible and Wearable Planar Supercapacitor of Manganese Dioxide Nanoflowers on Carbon Fiber Cloth. *Ceramics International* **2020**, *46* (13), 21736–21743. https://doi.org/10.1016/j.ceramint.2020.05.282.

(188) Efremova, A. O.; Volkov, A. I.; Tolstopyatova, E. G.; Kondratiev, V. V. EQCM Study of Intercalation Processes into Electrodeposited MnO_2 Electrode in Aqueous Zinc-Ion Battery Electrolyte. *Journal of Alloys and Compounds* **2022**, *892*, 162142. https://doi.org/10.1016/j.jallcom.2021.162142.

(189) Qiu, C.; Zhu, X.; Xue, L.; Ni, M.; Zhao, Y.; Liu, B.; Xia, H. The Function of Mn^{2+} Additive in Aqueous Electrolyte for Zn/δ-MnO_2 Battery. *Electrochimica Acta* **2020**, *351*, 136445. https://doi.org/10.1016/j.electacta.2020.136445.

(190) Li, J.; Chai, G.; Wang, X. Atomic Layer Deposition of Thin Films: From a Chemistry Perspective. *Int. J. Extrem. Manuf.* **2023**, *5* (3), 032003. https://doi.org/10.1088/2631-7990/acd88e.

(191) Ahmed, R.; Siddique, A.; Anderson, J.; Engdahl, C.; Holtz, M.; Piner, E. Selective Area Deposition of Hot Filament CVD Diamond on 100 Mm MOCVD Grown AlGaN/GaN Wafers. *Cryst. Growth Des.* **2019**, *19* (2), 672–677. https://doi.org/10.1021/acs.cgd.8b01260.